國 立 交 通 大 學

電子工程學系 電子研究所碩士班

碩 士 論 文

LTE 及 LTE-Advanced 上行通道估計之研究

Research in Uplink Channel Estimation for LTE and LTE-Advanced

研 究 生：李政憲

指導教授：林大衛 博士

中 華 民 國 一 ○ 二 年 三 月

LTE 及 LTE-Advanced 上行通道估計之研究

Research in Uplink Channel Estimation for LTE and LTE-Advanced

研究生：李政憲　　Student: Cheng-Hsien Lee

指導教授：林大衛 博士　　Advisor: Dr. David W. Lin

國 立 交 通 大 學

電子工程學系　　電子研究所碩士班

碩士論文

A Thesis

Submitted to Department of Electronics Engineering & Institute of Electronics

College of Electrical and Computer Engineering

National Chiao Tung University

in Partial Fulfillment of the Requirements

for the Degree of Master of Science

in

Electronics Engineering

October 2011

Hsinchu, Taiwan, Republic of China

中華民國一〇二年三月

LTE 及 LTE-Advanced 上行通道估計之研究

研究生 ： 李政憲　　指導教授 ： 林大衛　博士

國立交通大學

電子工程學系　電子研究所碩士班

摘要

無線通訊在未來通訊的發展佔了很重要的地位，其中更以 WiMAX(IEEE)跟 LTE(3GPP)這兩個分支為基礎個別發展；雖然大致上這兩個系統十分相似，但最主要的差異就在於LTE 在上傳採用的是單載波分頻多工存取(SC-FDMA)的技術。有別於 WiMAX 所使用的正交分頻多工存取(OFDMA)，其優點在於能降低峰均值比(PAPR)而使手機端(MS)的電池壽命更久、更省電，因而延長使用時間。本篇論文介紹 LTE 和 LTE-A 單載波分頻多工存取(SC-FDMA)中，多通道傳輸通道估計的問題、演算法、分析及模擬等議題，並延伸多輸入多輸出(MIMO)通道。

在通道估測中，我們分為單輸入單輸出(SISO)和多輸入多輸出的討論。首先在單輸入單輸出通道中，我們先採用最小平方差(least square)的估計器，然後再利用兩種方法在頻域去估測出載波的頻率響應並比較其效能。第一種方法是線性最小均方根誤差(LMMSE)，利用最小平方差估計器所求得的參考訊號(reference signal)上載波頻率響應，乘上線性最小均方根誤差矩陣來使參考訊號更我平滑，而線性最小均方跟誤差矩陣基於通道相關矩陣。第二種方法則是利用高斯分布當作權重來使參考訊號平滑，我們稱為高斯窗口(GWD)。接下來兩種方式皆是用線性內差的方式來得到資料載波上的頻域響應。在多輸入多輸出的系統中，我們利用參考訊號的循環位移(cyclic shift)，在頻域和時域中分開多根天線所產生的資料重疊。分開通道後，分別對各個通道做通道估計。

在模擬當中，我們先在加成性白高斯雜訊(AWGN)通道上驗證我們的模擬模型，然後在放置於多重路徑的通道上模擬，首先結果發現在低訊號雜訊比(SNR)的情況下，線性最小均方根誤差估計器的效能與高斯窗口的效能差不多，但高斯窗口的複雜度會比線性最小均方根誤差來的低。再來我們觀察到在頻域做通道分開比在時域做通道分開來的精準。

我們研究的貢獻主要是降低單輸入單輸出的通道估計的複雜度，還有增加再多輸入多輸出通道分開的準確度。

Research in Uplink Channel Estimation for LTE and LTE-Advanced

Student: Cheng-Hsien Lee Advisor: Dr. David W. Lin

Department of Electronics Engineering
& Institute of Electronics
National Chiao Tung University

Abstract

Wireless communication will play an important role in the evolution of communication in the future, especially basing on WiMAX (IEEE) and LTE (3GPP) to develop individually. Although the two systems are very similar, the biggest difference of them is that LTE using single carrier frequency division multiple access (SC-FDMA) technique in uplink transmission. The advantage of LTE is to decrease peak-to-average power ratio (PAPR) which saves more power of the batteries of user equipments (UEs) and efficiently extends the using time, rather than using OFDMA (orthogonal frequency division multiple access) which is adopted by WiMAX. This thesis will introduce the subjects of channel estimation problems, algorithms, analysis of multi-path transmission in SC-FDMA, and extend to the multi-input multi-output (MIMO) channel.

In channel estimation, we divided into the discussion of the single-input single-output (SISO) and MIMO. In single-input single-output system, first we use least square estimator, then use two different methods to estimate the channel response in frequency domain and compare the performance between them. The first method is linear minimum-mean square error (LMMSE). We use reference signal channel response which estimates by least square estimator multiplied the linear minimum-mean square error matrix to make more smooth, and the linear minimum-mean square error matrix base on the channel correlation matrix. The second method is using Gaussian distribution window (GWD) to make reference

signal more smooth. And then the two methods all use linear interpolation to get the channel response of data carriers. In multiple-input multiple-output system, we use cyclic shift of reference signal to separate channel form different transmit antenna in time domain and frequency domain. After channel separation, channel estimation for each channel.

In simulation, we test and verify the simulate model which we proposed, in additive white Gaussian noise. Then we simulate in multi-path channel. First we find that LMMSE has similar performance as Gaussian distribution window in symbol error rate and mean square error, but Gaussian distribution window has lower complexity than LMMSE. Second we observe that frequency domain channel separation is better than time domain channel separation.

Our contribution to the research is mainly to reduce the complexity of the SISO channel estimation, as well as to increase the accuracy of the MIMO channel separation.

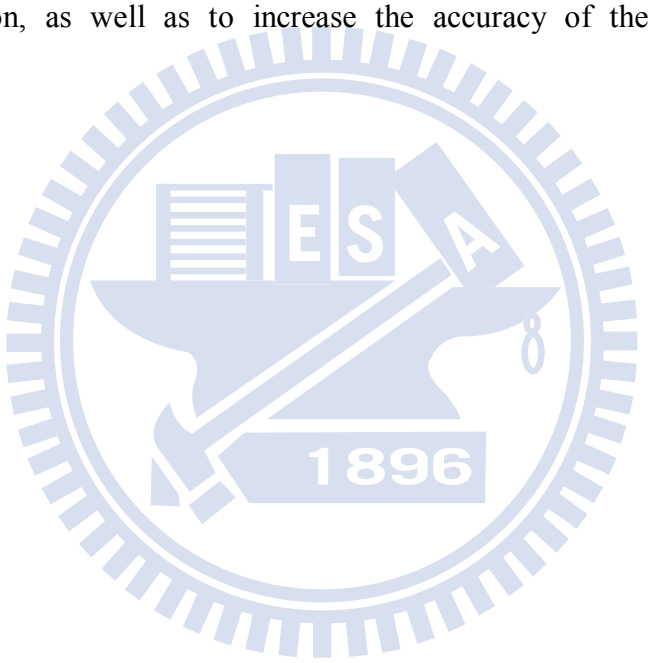

誌謝

經過不斷的討論與修改，這篇論文終於能夠順利的完成。首先當然是非常感謝我的指導教授林大衛教授耐心、細心、詳細的修改整篇論文，以及這兩年來辛苦的教導，讓我能在通訊的領域有了基本的認識，也使得這篇論文能夠完成，在一次感謝林大衛教授。

此外，在這兩年的日子當中通訊電子與訊號處理實驗室的所有成員們，包含各位師長、同學、學長姐以及學弟妹們，感謝你們讓我在這兩年的時光充滿活力以及歡笑。在這邊感謝王柏森學長、蕭世璞學長、洪朝雄學長、劉峻利學長、余卓翰學長、詹曉盈學長、柯俊言學長、陳威宇學長、張智凱學長、楊凱翔學長、楊復凱學長、羅偵源學長和翁郁婷學姐對我在學術上的不吝指導與建議，謝謝你們幫我解決了許多學業方面的疑問。感謝 99 級基峰、晉源、維哲、義文、士傑、建志、建宏、柔陵以及 100 級學弟們等實驗室成員，平日和我一起念書、討論、研究、玩樂，讓我的研究生涯擁有美好的回憶。

最後，必須感謝我的家人，我的父母親，我的朋友，包容我這幾年的任性及不成熟。有你們給予我的支持，使我在讀書時能無後顧之憂。感謝以上所有人的支持，也謝謝所有幫助過我、陪我走過這段歲月的人

李政憲

民國一百二年三月　於新竹

E S A
1896

Contents

List of Figures

List of Tables

Chapter 1

Introduction

Single-carrier frequency-division multiple access (SC-FDMA) is the chosen multiple access scheme for the uplink in the 3rd Generation Partnership Project (3GPP) Long Term Evolution (LTE) as will as LTE-Advanced (LTE-A), which are some of the major latest standards for cellular mobile communication [3, 23]. The LTE-A standard is a standard designed to increase the capacity and speed of mobile telephone networks as well as be compliant with IMT-Advanced requirements. It is backwards compatible with LTE and uses the same frequency bands, while LTE is not backwards compatible with the earlier 3G systems. The LTE is introduced in 3GPP release 8 whereas LTE-A, release 10. Much of 3GPP release 8 focuses on adopting expected 4G mobile communication technologies, including an all-IP flat networking architecture. The 3GPP is keeping working on evolving the LTE standards towards future releases.

Compared with another 4G system WiMAX (including WiMAX-2), the major difference between LTE and WiMAX in the physical layer (PHY) is the transmission scheme in the uplink. For WiMAX, both uplink and downlink use orthogonal frequency-division multiple access (OFDMA). But in LTE, only the downlink uses OFDMA. The benefit of using SC-FDMA in the uplink is that the peak-to-average power ratio (PAPR) of signals can be much lower than OFDMA. The lower PAPR, the better power efficiency of cell phones.

Our study focuses on LTE and LTE-A physical uplink shared channel (PUSCH) estimation schemes based on the 3GPP TS 36.211 release 8 [1] and release 10 [2]. First, we consider the single-input single-output (SISO) transmission structure and investigate the performance of different channel estimation techniques in the multi-path channel environment. Several channel estimation techniques have been proposed. A part of our research is based on the frequency domain channel estimation technique proposed in [10], and we propose improved techniques to lower the complexity and better the performance.

LTE (release 8) does not support uplink multiple-input-multiple-output (MIMO) transmission in the uplink, but considers only the case of one uplink transmit antenna on a user equipment (UE). In LTE-A (release 10), the allowed number of uplink transmit antennas is increased to four. So one key feature introduced in LTE-A is MIMO transmission for each UE (in addition to the multi-user MIMO, or MU MIMO, already specified in LTE). In MIMO channel estimation, a main issue is inter-antenna interference. To maximize the benefit of MIMO, a baseband receiver capable of untangling the multiple spatially multiplexed signals received simultaneously is desired. Hence, separation of different antenna channels (or antenna separation in short) is a focus of our study and with different antenna channels separated we can use SISO channel estimation methods to deal with each antenna channel in the overall MIMO channel.

For antenna separation, we consider two different methods. The first is based on the time shift of the channel impulse response (CIR) effected by the linear phase shift in the reference signal (RS) for each transmit antenna. And the second solves some linear equations in the coherence bandwidth. The second method performs better when the delay spread of the channel is smaller.

Our contribution to the research is mainly to reduce the complexity of the SISO channel estimation, as well as to increase the accuracy of the MIMO channel separation. The

following is a summary of each chapter.

- In chapter 2, we introduce some SC-FDMA basics in the LTE and LTE-A uplink standards.
- In chapter 3, we describe the uplink transmission system structure and introduce various channel estimation techniques.
- In chapter 4, we discuss the performance of difference channel estimation methods. We analyze the mean square error (MSE) and the symbol error rate (SER) performance of different methods including frequency domain (FD) linear minimum mean square error (LMMSE) and FD domain Gaussian distributed windowing (GWD) estimation in SISO system, and different methods including time domain (TD) channel separation (CS) and FD channel separation (CS) in MIMO system.
- In chapter 5, we give the conclusion and indicate some items of potential future work.

Chapter 2

Overview of LTE and LTE-A Uplink Specifications

The contents of the LTE (release 8) part of this overview are largely taken from [1]–[4] and [22].

The goal of LTE is to provide a high-data-rate, low-latency and packet-optimized radio access technology supporting flexible bandwidth deployments [1, 3]. In parallel, new network architecture is designed with the goal to support packet-switched traffic with seamless mobility, quality of service and minimal latency.

The air interface-related attributes of the LTE system are summarized in Table 2.1. The system supports flexible bandwidths thanks to OFDMA and SC-FDMA access schemes. In addition to frequency division duplexing (FDD) and time division duplexing (TDD), half-duplex FDD is allowed to support low cost user equipment (UE). Unlike FDD, in half-duplex FDD operation a UE is not required to transmit and receive at the same time. This avoids the need for a costly duplexer in the UE.

The system is primarily optimized for low speeds up to 15 km/h. However, the system specifications allow mobility support in excess of 350 km/h with some performance degradation. As mentioned in ch. 1, the uplink (UL) access is based on SC-FDMA which promises

Table 2.1: LTE System Attributes [3, Table 1.1]

Bandwidth	1.25–20 MHz	
Duplexing	FDD, TDD, half-duplex FDD	
Mobility	350km/h	
Multiple access	Downlink	OFDMA
	Uplink	SC-FDMA
MIMO	Downlink	$2 \times 2, 4 \times 2, 4 \times 4$
	Uplink	$1 \times 2, 1 \times 4$
MIMO	Downlink	173 and 326 Mb/s for 2×2 and 4×4 MIMO, respectively
	Uplink	86 Mb/s with 1×2 antenna configuration
Modulation	QPSK, 16-QAM and 64-QAM	
Channel coding	Turbo code	
Other techniques	Channel sensitive scheduling, link adaptation, power control, ICIC and hybrid ARQ	

increased UL coverage due to low PAPR relative to OFDMA.

In LTE, the downlink (DL) allows a maximum of four layers of MIMO transmission, while the UL has a maximum of one for one UE. Together with the fact that the UE has a two-branch receiver diversity, we can support 4×2 single-user (SU) MIMO in the DL and no SU MIMO from a single UE in the UL. With LTE-A, the situation is considerably different. It can support up to eight streams in the DL with eight receivers in the UE. This will give a possibility of 8×8 MIMO in the DL. And in the UL, the UE is allowed to support up to four transmitters, thereby offering a possibility of up to 4×4 transmissions.

In this chapter, we introduce SC-FDMA and the physical channel structure in LTE [1] and LTE-A specifications [2], focusing especially on the UL part.

2.1 Single-Carrier FDMA

The contents of this section are mainly taken from [3, Chapter 3].

SC-FDMA scheme provides orthogonal access to multiple users simultaneously accessing the system. In one flavor of the SC-FDMA scheme referred to as interleaved frequency division multiple access (IFDMA), the user data sequence is first repeated a predetermined number of times. Then the repeated data sequence is multiplied with a user-specific phase vector. Another way of looking at this approach is discrete Fourier transform (DFT) precoding of the data sequence and then mapping of the DFT-precoded data sequence to uniformly spaced subcarriers at the input of on IDFT. The uniform spacing is determined by a repetition factor Q. The multiplication of the repeated data sequence with a user-specific phase vector can be seen as frequency shift applied in order to map transmissions from multiple users on non-overlapping orthogonal subcarriers. As each data modulation symbol is spread out on all the subcarriers used by the UE, this can provide a frequency-diversity benefit in a frequency-selective channel. However, there may be some impact on performance due to loss of orthogonality or noise enhancement when data subcarriers experience frequency selective fading. We will refer to the IFDMA scheme as distributed FDMA (DFDMA) below.

The mapping of DFT-precoded data sequence to contiguous subcarriers results in a localized transmission in the frequency domain (FD). Similar to DFDMA, localized mapping also results in a low PAPR signal. The different ways of mapping of DFT precoded data sequence to OFDM subcarriers are sometimes collectively referred to as DFT-spread OFDM. In the case of DFDMA, the input samples to the IDFT are given as

$$\tilde{X}_l = \begin{cases} X_{l/Q}, & l = Q \cdot k,\ 0 \leqslant k \leqslant M-1, \\ 0, & \text{otherwise.} \end{cases} \tag{2.1}$$

Let $n = M \times q + m$ where $0 \leqslant q \leqslant Q-1$ and $0 \leqslant m \leqslant M-1$, The time domain (TD) samples at the output of IDFT are then given as

$$\tilde{x}_n = \frac{1}{N} \sum_{l=0}^{N-1} \tilde{X}_l e^{j2\pi \frac{n}{N} l}, \tag{2.2}$$

or,

$$\tilde{x}_n = \frac{1}{Q \cdot M} \sum_{k=0}^{M-1} X_k e^{j2\pi \frac{n}{M} k}. \tag{2.3}$$

We have

$$\tilde{x}_n = \frac{1}{Q \cdot M} \sum_{k=0}^{M-1} X_k e^{j2\pi \frac{M \times q + m}{M} k} = \frac{1}{Q} (\frac{1}{M} \sum_{k=0}^{M-1} X_k e^{j2\pi \frac{m}{M} k}) = \frac{1}{Q} x_m. \tag{2.4}$$

It can thus be seen that the TD symbols at the output of size-N IDFT are repetitions of TD symbols at the input of size-M DFT when $N = QM$.

In the case of localized FDMA (LFDMA), the input samples to the IDFT are given as

$$\tilde{X}_l = \begin{cases} X_l, & 0 \leqslant l \leqslant M-1, \\ 0, & M \leqslant l \leqslant N-1. \end{cases} \tag{2.5}$$

Let $n = Q \times m + q$, where $0 \leqslant q \leqslant Q-1$ and $0 \leqslant m \leqslant M-1$. The TD samples at the output of the IDFT are then given as

$$\tilde{X}_n = \frac{1}{N} \sum_{l=0}^{N-1} \tilde{X}_l e^{j2\pi \frac{n}{N} l}, \tag{2.6}$$

or,

$$\tilde{X}_n = \frac{1}{Q \cdot M} \sum_{l=0}^{M-1} X_l e^{j2\pi \frac{Q \times m + q}{Q \cdot M} k}. \tag{2.7}$$

For $q = 0$,

$$\tilde{x}_n = \frac{1}{Q} \cdot \frac{1}{M} \sum_{l=0}^{M-1} X_l e^{j2\pi \frac{m}{M} k} = \frac{1}{Q} x_m. \tag{2.8}$$

It can thus be seen that every Qth TD sample at the output of size N-IDFT is the same as the TD sample at the input of size M-DFT. For $q \neq 0$, the TD sample at the output of size-N IDFT is the sum of TD samples at the input of size M DFT with different complex weighting. An example of DFDMA and LFDMA mapping for $M = 4$, $N = 8$ and $Q = N/M = 2$ is given in Figure 2.1.

The transmit and receive chains for LFDMA are given in Figures 2.2 and 2.3 respectively, where it is assumed that DFTs and IDFTs are implemented using fast Fourier transforms

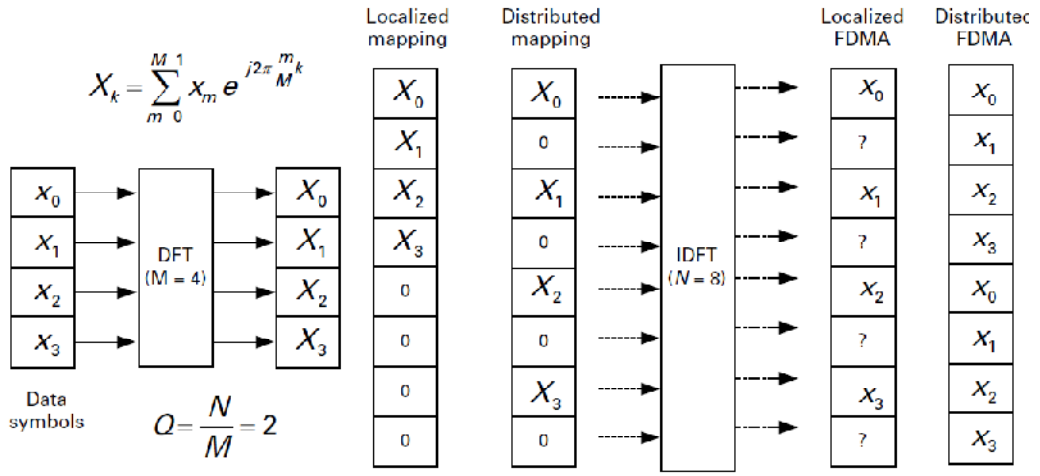

Figure 2.1: An example for subcarrier mapping of LFDMA and DFDMA [3, Fig. 4.1].

(FFTs) and inverse FFTs respectively. Moreover, it is assumed that the receiver employs frequency-domain equalization (FDE), whose operation will be touched on shortly later. All UEs use the same IDFT size of N. However, different UEs can use different DFT-precoding sizes. The size of the DFT precoder for a UE is proportional to the orthogonal subcarriers allocated to the UE for UL transmission. Except for multi-user (MU) MIMO transmission where different user signals may occupy the same subcarriers, different user signals must use distinct subcarriers.

A cyclic prefix (CP) is added after IFFT and the resulting sequence is up-converted to RF, amplified and transmitted. Each UE power amplifier sees a single FFT-precoded transmission, which leads to low signal peakiness. If we map FFT-precoded data sequences of multiple UEs to the same IFFT and transmit from a single power amplifier, it will no longer have low signal peakiness. This is one reason why SC-FDMA is not considered for DL transmission. In the DL, the base station (called Node-B in LTE and eNode-B in LTE-A) generally simultaneous transmits by signals to multiple UEs on orthogonal subcarriers using a single common power amplifier.

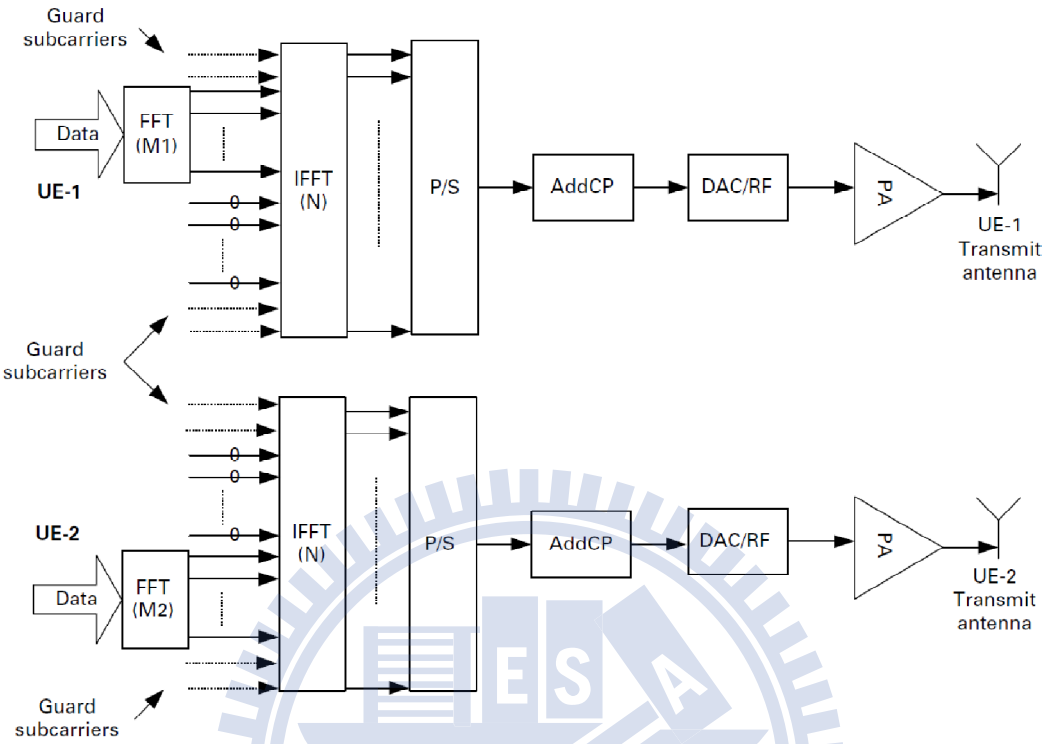

Figure 2.2: LFDMA transmitter [3, Fig. 4.2].

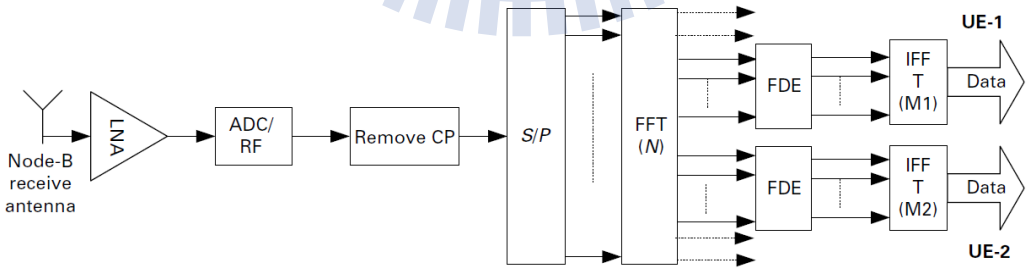

Figure 2.3: LFDMA receiver [3, Fig. 4.3].

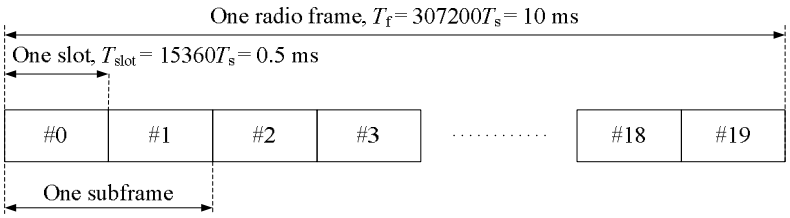

Figure 2.4: Frame structure type 1 [2, Fig. 4.1-1].

At the receiver, the received signal is filtered, amplified and down-converted from RF. The CP samples are discarded and a size-N FFT is performed on the received sample sequence. The symbols for each UE are separated by collecting data from the subcarriers allocated to a UE. An FDE operation is performed using channel estimates obtained from pilots (or reference signal, RS) received for each UE. An IFFT is then performed separately for each UE to recover the transmitted data sequence. Data demodulation in SC-FDMA is in the TD after the IDFT.

2.2 Frame Structure

The contents of this section are mainly taken from [2].

Throughout the specification of frame structure in LTE, the size of various fields in the TD is normally expressed in time units of $T_s = 1/(15000 \times 2048)$ seconds. DL and UL transmissions are organized into radio frames with frame duration $T_f = 307200 \cdot T_s = 10$ ms. Frame structure type 1 is shown in Figure 2.4. It is applicable to both full duplex and half duplex FDD. Each radio frame each consists of 20 slots of length $T_{slot} = 15360 \cdot T_s = 0.5$ ms, which are numbered from 0 to 19. A subframe consists of two consecutive slots where subframe i consists of slots $2i$ and $2i+1$. For FDD, there are 10 subframes for DL transmission and 10 subframes for UL transmissions in each 10 ms interval.

2.3 Slot Structure and Physical Resources

The contents of this section are mainly taken from [2].

The transmitted signal in each slot is described by a resource grid of $N_{RB}^{UL}N_{sc}^{RB}$ subcarriers and N_{symb}^{UL} SC-FDMA symbols as illustrated in Figure 2.5. The quantity N_{RB}^{UL} depends on the UL transmission bandwidth configured in the cell and shall fulfill

$$N_{RB}^{min,UL} \leqslant N_{RB}^{UL} \leqslant N_{RB}^{max,UL}$$

where $N_{RB}^{min,UL} = 6$ and $N_{RB}^{max,UL} = 110$ is the smallest and largest UL bandwidths, respectively, supported by release 8. The number of SC-FDMA symbols in a slot depends on the CP length configured by higher layers.

An antenna port is defined such that the channel over which a symbol on the antenna port is conveyed can be inferred from the channel over which another symbol on the same antenna port is conveyed. There is one resource grid per antenna port. The antenna ports used for transmission of a physical channel or signal depends on the number of antenna ports configured for the physical channel or signal as shown in Table 2.2.

Each element in the resource grid is called a resource element (RE) and is uniquely defined by the index pair (k, l) in a slot where $k = 0, ..., N_{RB}^{UL} \cdot N_{sc}^{RB} - 1$ and $l = 0, ..., N_{symb}^{UL} - 1$ are the indices in the FD and TD, respectively. RE (k, l) corresponds to the complex siganl value $a_{k,l}$. For an RE not used for transmission of a physical channel or a physical signal in a slot, $a_{k,l}$ shall be set to zero.

A physical resource block (RB) is defined as N_{symb}^{UL} consecutive SC-FDMA symbols in the TD and N_{sc}^{RB} consecutive subcarriers in the FD, where N_{symb}^{UL} and N_{sc}^{RB} are as given in Table 2.3. A physical RB in the UL thus consists of $N_{symb}^{UL} \times N_{sc}^{RB}$ REs, corresponding to one slot in the TD and 180 kHz in the FD. Note that the subcarrier spacing (Δf) is 15 kHz.

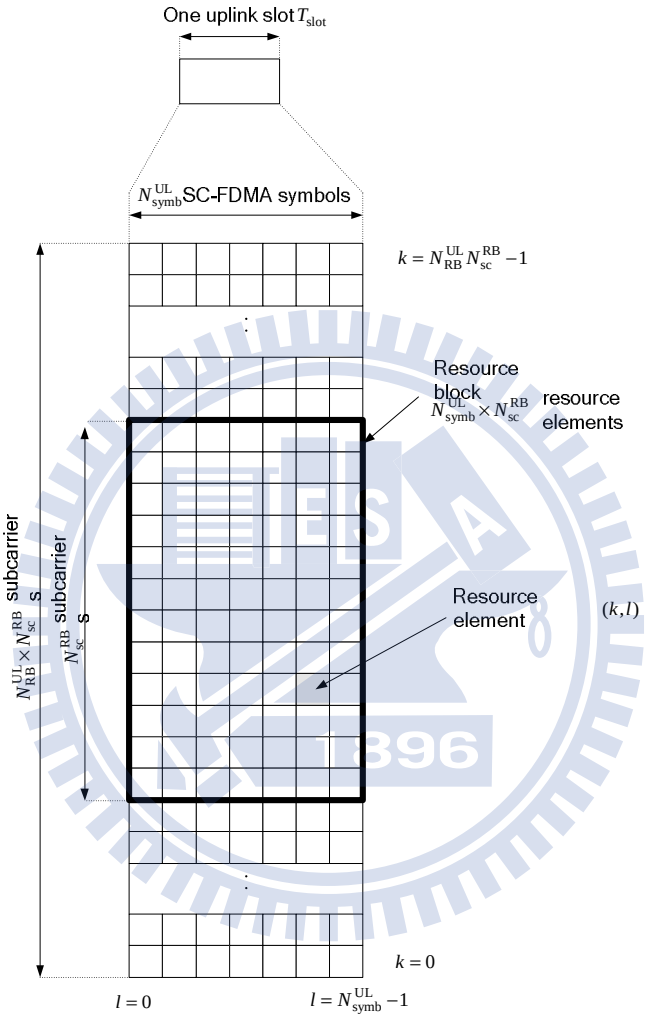

Figure 2.5: UL resource grid [2, Fig. 5.2.1-1].

Table 2.2: Antenna Ports Used for Different Physical Channels and Signals [2, Table 5.2.1-1]

Physical channel or signal	index $\widetilde{p}$	Antenna port number p as a function of the number of antenna ports configured for the respective physical channel signal		
		1	2	4
PUSCH	0	10	20	40
	1	-	21	41
	2	-	-	42
	3	-	-	43
SRS	0	10	20	40
	1	-	21	41
	2	-	-	42
	3	-	-	43
PUCCH	0	100	200	-
	1	-	201	-

Table 2.3: RB Parameters [2, Table 5.2.3-1]

Configuration	N_{sc}^{RB}	N_{symb}^{UL}
Normal CP	12	7
Extended CP	12	6

The relation between the physical RB number n_{PRB} in the FD and REs (k, l) in a slot is given by

$$n_{PRB} = \lfloor \frac{k}{N_{sc}^{RB}} \rfloor.$$

Figure 2.6 shows the detailed slot stucture. The normal CP length is 5.2 μs ($160 \times T_s$) in the first SC-FDMA or OFDM symbol and 4.7 μs ($144 \times T_s$) in the remaining six symbols.

2.4 Physical Uplink Shared Channel (PUSCH)

The contents of this section are mainly taken from [2].

The baseband signal representing the physical UL shared channel (PUSCH) in LTE is

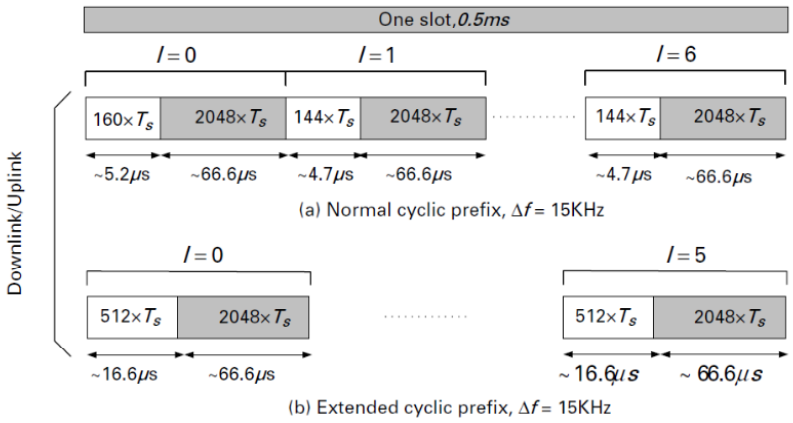

Figure 2.6: Slot structure for normal and extended CP [3, Fig. 8.3].

defined in terms of the following steps and illustrated in Figure 2.7:

- Scrambling.
- Modulation of scrambled bits to generate complex-valued symbols.
- Mapping of the complex-valued modulation symbols onto one or several transmission layers.
- Transform precoding to generate complex-valued symbols.
- Precoding of the complex-valued symbols.
- Mapping of complex-valued symbols to REs.
- Generation of complex-valued time-domain SC-FDMA signal for each antenna port.

2.4.1 Scrambling

The block of bits $b(0), ..., b(M_{bit} - 1)$, where M_{bit} is the number of bits transmitted on the PUSCH in one subframe, is scrambled with a UE-specific scrambling sequence prior to

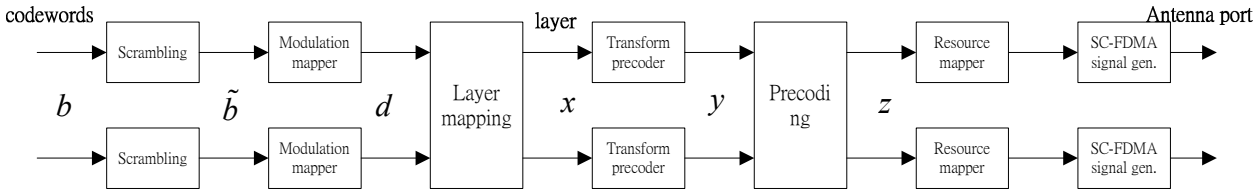

Figure 2.7: UL physical channel processing in the transmitter (modified from [2, Fig. 5.3-1]).

modulation. The detailed scramblimg method is not relevant to the present study and is omitted.

2.4.2 Modulation

The block of scrambled bits $\tilde{b}(0), ..., \tilde{b}(M_{bit} - 1)$ is modulated to yield a block of complex-valued symbols $d(0), ..., d(M_{symb} - 1)$. The modulations specified for PUSCH are QPSK, 16QAM and 64QAM.

2.4.3 Layer Mapping

The complex-valued modulation symbols for each of the codewords are mapped onto layers. Complex-valued modulation symbols $d^{(q)}(0), ..., d^{(q)}(M_{symb}^{(q)} - 1)$ for codeword q shall be mapped onto the layers as $x(i) = \left[x^{(0)}(i), ..., x^{(\nu-1)}(i)\right]^T, i = 0, 1, ..., M_{symb}^{(q)} - 1$, where ν the number of layers and $M_{symb}^{(q)}$ is the number of modulation symbols per layer.

For transmission on a single antenna port, a single layer is used, $\nu = 1$, and the mapping is defined by $x^{(0)}(i) = d^{(0)}(i)$ with $M_{symb}^{(layer)} = M_{symb}^{(0)}$.

For spatial multiplexing, the layer mapping is done according to Table 2.4. The number of layers ν is less than or equal to the number of antenna ports P used for transmission of the physical uplink shared channel. The case of a single codeword mapped to multiple layers is only applicable when the number of antenna ports used for PUSCH is four.

Table 2.4: Codeword-to-Layer Mapping for Spatial Multiplexing [2, Table 5.3.2A.2-1]

Number of layers	Number of codewords	Codeword-to-layer mapping $i = 0, 1, ..., M_{symb}^{layer} - 1$	
1	1	$x^{(0)}(i) = d^{(0)}(i)$	$M_{symb}^{layer} = M_{symb}^{0}$
2	1	$x^{(0)}(i) = d^{(0)}(2i)$ $x^{(1)}(i) = d^{(0)}(2i+1)$	$M_{symb}^{layer} = M_{symb}^{0}/2$
2	2	$x^{(0)}(i) = d^{(0)}(i)$ $x^{(1)}(i) = d^{(1)}(i)$	$M_{symb}^{layer} = M_{symb}^{0} = M_{symb}^{1}$
3	2	$x^{(0)}(i) = d^{(0)}(i)$ $x^{(1)}(i) = d^{(1)}(2i)$ $x^{(2)}(i) = d^{(1)}(2i+1)$	$M_{symb}^{layer} = M_{symb}^{0} = M_{symb}^{1}/2$
4	2	$x^{(0)}(i) = d^{(0)}(2i)$ $x^{(1)}(i) = d^{(0)}(2i+1)$ $x^{(2)}(i) = d^{(1)}(2i)$ $x^{(3)}(i) = d^{(1)}(2i+1)$	$M_{symb}^{layer} = M_{symb}^{0}/2 = M_{symb}^{1}/2$

2.4.4 Transform Precoding

For each layer $\lambda = 0, 1, ..., \nu - 1$, the block of complex-valued symbols $x^{(\lambda)}(0), ..., x^{(\lambda)}(M_{symb}^{layer} - 1)$ is divided into M_{symb}/M_{sc}^{PUSCH} sets, each corresponding to one SC-FDMA symbol. Transform precoding is applied according to

$$y^{\lambda}(l \cdot M_{sc}^{PUSCH} + k) = \frac{1}{\sqrt{M_{sc}^{PUSCH}}} \sum_{i=0}^{M_{sc}^{PUSCH}-1} x^{\lambda}(l \cdot M_{sc}^{PUSCH} + 1) e^{-j\frac{2\pi ik}{M_{sc}^{PUSCH}}}, \qquad (2.9)$$

where $k = 0, ..., M_{sc}^{PUSCH} - 1$ and $l = 0, ..., M_{symb}/M_{sc}^{PUSCH} - 1$. This results in a block of complex-valued symbols $y(0), ..., y(M_{symb} - 1)$. In the above $M_{sc}^{PUSCH} = M_{RB}^{PUSCH} \cdot N_{sc}^{RB}$ where M_{RB}^{PUSCH} represents the bandwidth of the PUSCH in terms of RBs and shall fulfill

$$M_{RB}^{PUSCH} = 2^{\alpha_2} \cdot 3^{\alpha_3} \cdot 5^{\alpha_5} \leqslant N_{RB}^{UL},$$

where $\alpha_2, \alpha_3, \alpha_5$ are nonnegative integers.

2.4.5 Precoding

The precoder takes as input a block of vectors $\left[y^{(0)}(i), ..., y^{(\nu-1)}(i)\right]^T$, $i = 0, 1, ..., M_{symb}^{layer} - 1$, from the transform precoder and generates a block of vectors $\left[z^{(0)}(i), ..., z^{(P-1)}(i)\right]^T$, $i = 0, 1, ..., M_{symb}^{ap} - 1$, to be mapped onto REs.

For transmission on a single antenna port, precoding is defined by $z^{(0)}(i) = y^{(0)}(i)$ where $i = 0, 1, ..., M_{symb}^{ap} - 1$, and $M_{symb}^{ap} = M_{symb}^{layer}$.

Precoding for spatial multiplexing is only used in combination with layer mapping for spatial multiplexing. Spatial multiplexing supports $P = 2$ or $P = 4$ antenna ports where the set of antenna ports used for spatial multiplexing is $p \in \{20, 21\}$ and $p \in \{40, 41, 42, 43\}$, respectively. Precoding for spatial multiplexing is defined by

$$\begin{bmatrix} z^{(0)}(i) \\ \vdots \\ z^{(P-1)}(i) \end{bmatrix} = W \begin{bmatrix} y^{(0)}(i) \\ \vdots \\ y^{(\nu-1)}(i) \end{bmatrix}$$

where $i = 0, 1, ..., M_{symb}^{ap} - 1$, and $M_{symb}^{ap} = M_{symb}^{layer}$. The precoding matrix W of size $P \times \nu$ is given by one of the entries in Table 2.5 for $P = 2$ and by Tables 2.6 through 2.9 for $P = 4$ where the entries in each row are ordered from left to right in increasing order of codebook indices.

2.4.6 Mapping to Physical Resources

The block of complex-valued symbols $z^{(P)}(0), ..., z^{(P)}(M_{symb}^{ap} - 1)$ is multiplied with the amplitude scaling factor β_{PUSCH} conforming to the transmit power P_{PUSCH} specified in [5, section 5.1.1.1] and mapped in sequence starting with $z(0)$ to physical RBs assigned for transmission of PUSCH. The mapping is applied only to REs (k, l) corresponding to the physical RB assigned for transmission and not used for transmission of RS and not reserved for possible sounding RS transmission. It is in increasing order of first the index k, then the index l,

Table 2.5: Codebook for Transmission on Antenna Ports {20, 21} [2, Table 5.3.3A.2-1]

Codebook index	Number of layers $\nu = 1$	$\nu = 2$
0	$\frac{1}{\sqrt{2}}\begin{bmatrix}1\\1\end{bmatrix}$	$\frac{1}{\sqrt{2}}\begin{bmatrix}1 & 0\\0 & 1\end{bmatrix}$
1	$\frac{1}{\sqrt{2}}\begin{bmatrix}1\\-1\end{bmatrix}$	-
2	$\frac{1}{\sqrt{2}}\begin{bmatrix}1\\j\end{bmatrix}$	-
3	$\frac{1}{\sqrt{2}}\begin{bmatrix}1\\-j\end{bmatrix}$	-
4	$\frac{1}{\sqrt{2}}\begin{bmatrix}1\\0\end{bmatrix}$	-
5	$\frac{1}{\sqrt{2}}\begin{bmatrix}0\\1\end{bmatrix}$	-

Table 2.6: Codebook for Transmission on Antenna Ports {40, 41, 42, 43} with $\nu = 1$ [2, Table 5.3.3A.2-2]

Codebook index	Number of layers $\nu = 1$							
0–7	$\frac{1}{2}\begin{bmatrix}1\\1\\1\\-1\end{bmatrix}$	$\frac{1}{2}\begin{bmatrix}1\\1\\j\\j\end{bmatrix}$	$\frac{1}{2}\begin{bmatrix}1\\1\\-1\\1\end{bmatrix}$	$\frac{1}{2}\begin{bmatrix}1\\1\\-j\\-j\end{bmatrix}$	$\frac{1}{2}\begin{bmatrix}1\\j\\1\\j\end{bmatrix}$	$\frac{1}{2}\begin{bmatrix}1\\j\\j\\1\end{bmatrix}$	$\frac{1}{2}\begin{bmatrix}1\\j\\-1\\-j\end{bmatrix}$	$\frac{1}{2}\begin{bmatrix}1\\j\\-j\\-1\end{bmatrix}$
8–15	$\frac{1}{2}\begin{bmatrix}1\\-1\\1\\1\end{bmatrix}$	$\frac{1}{2}\begin{bmatrix}1\\-1\\j\\-j\end{bmatrix}$	$\frac{1}{2}\begin{bmatrix}1\\-1\\-1\\-1\end{bmatrix}$	$\frac{1}{2}\begin{bmatrix}1\\-1\\-j\\j\end{bmatrix}$	$\frac{1}{2}\begin{bmatrix}1\\-j\\1\\-j\end{bmatrix}$	$\frac{1}{2}\begin{bmatrix}1\\-j\\j\\-1\end{bmatrix}$	$\frac{1}{2}\begin{bmatrix}1\\-j\\-1\\j\end{bmatrix}$	$\frac{1}{2}\begin{bmatrix}1\\-j\\-j\\1\end{bmatrix}$
16–23	$\frac{1}{2}\begin{bmatrix}1\\0\\1\\0\end{bmatrix}$	$\frac{1}{2}\begin{bmatrix}1\\0\\-1\\0\end{bmatrix}$	$\frac{1}{2}\begin{bmatrix}1\\0\\j\\0\end{bmatrix}$	$\frac{1}{2}\begin{bmatrix}1\\0\\-j\\0\end{bmatrix}$	$\frac{1}{2}\begin{bmatrix}0\\1\\0\\1\end{bmatrix}$	$\frac{1}{2}\begin{bmatrix}0\\1\\0\\-1\end{bmatrix}$	$\frac{1}{2}\begin{bmatrix}0\\1\\0\\j\end{bmatrix}$	$\frac{1}{2}\begin{bmatrix}0\\1\\0\\-j\end{bmatrix}$

starting with the first slot in the subframe.

Table 2.7: Codebook for Transmission on Antenna Ports {40,41,42,43} with $\nu = 2$ [2, Table 5.3.3A.2-3]

Codebook index	Number of layers $\nu = 2$			
0–3	$\frac{1}{2}\begin{bmatrix} 1 & 0 \\ 1 & 0 \\ 0 & 1 \\ 0 & -j \end{bmatrix}$	$\frac{1}{2}\begin{bmatrix} 1 & 0 \\ 1 & 0 \\ 0 & 1 \\ 0 & j \end{bmatrix}$	$\frac{1}{2}\begin{bmatrix} 1 & 0 \\ -j & 0 \\ 0 & 1 \\ 0 & 1 \end{bmatrix}$	$\frac{1}{2}\begin{bmatrix} 1 & 0 \\ -j & 0 \\ 0 & 1 \\ 0 & -1 \end{bmatrix}$
4–7	$\frac{1}{2}\begin{bmatrix} 1 & 0 \\ -1 & 0 \\ 0 & 1 \\ 0 & -j \end{bmatrix}$	$\frac{1}{2}\begin{bmatrix} 1 & 0 \\ -1 & 0 \\ 0 & 1 \\ 0 & j \end{bmatrix}$	$\frac{1}{2}\begin{bmatrix} 1 & 0 \\ j & 0 \\ 0 & 1 \\ 0 & 1 \end{bmatrix}$	$\frac{1}{2}\begin{bmatrix} 1 & 0 \\ j & 0 \\ 0 & 1 \\ 0 & -1 \end{bmatrix}$
8–11	$\frac{1}{2}\begin{bmatrix} 1 & 0 \\ 0 & 1 \\ 1 & 0 \\ 0 & 1 \end{bmatrix}$	$\frac{1}{2}\begin{bmatrix} 1 & 0 \\ 0 & 1 \\ 1 & 0 \\ 0 & -1 \end{bmatrix}$	$\frac{1}{2}\begin{bmatrix} 1 & 0 \\ 0 & 1 \\ -1 & 0 \\ 0 & 1 \end{bmatrix}$	$\frac{1}{2}\begin{bmatrix} 1 & 0 \\ 0 & 1 \\ -1 & 0 \\ 0 & -1 \end{bmatrix}$
12–15	$\frac{1}{2}\begin{bmatrix} 1 & 0 \\ 0 & 1 \\ 0 & 1 \\ 1 & 0 \end{bmatrix}$	$\frac{1}{2}\begin{bmatrix} 1 & 0 \\ 0 & 1 \\ 0 & -1 \\ 1 & 0 \end{bmatrix}$	$\frac{1}{2}\begin{bmatrix} 1 & 0 \\ 0 & 1 \\ 0 & 1 \\ -1 & 0 \end{bmatrix}$	$\frac{1}{2}\begin{bmatrix} 1 & 0 \\ 0 & 1 \\ 0 & 1 \\ -1 & 0 \end{bmatrix}$

Table 2.8: Codebook for Transmission on Antenna Ports {40,41,42,43} with $\nu = 3$ [2, Table 5.3.3A.2-4]

Codebook index	Number of layers $\nu = 3$			
0–3	$\frac{1}{2}\begin{bmatrix} 1 & 0 & 0 \\ 1 & 0 & 0 \\ 0 & 1 & 0 \\ 0 & 0 & 1 \end{bmatrix}$	$\frac{1}{2}\begin{bmatrix} 1 & 0 & 0 \\ -1 & 0 & 0 \\ 0 & 1 & 0 \\ 0 & 0 & 1 \end{bmatrix}$	$\frac{1}{2}\begin{bmatrix} 1 & 0 & 0 \\ 0 & 1 & 0 \\ 1 & 0 & 0 \\ 0 & 0 & 1 \end{bmatrix}$	$\frac{1}{2}\begin{bmatrix} 1 & 0 & 0 \\ 0 & 1 & 0 \\ -1 & 0 & 0 \\ 0 & 0 & 1 \end{bmatrix}$
4–7	$\frac{1}{2}\begin{bmatrix} 1 & 0 & 0 \\ 0 & 1 & 0 \\ 0 & 0 & 1 \\ 1 & 0 & 0 \end{bmatrix}$	$\frac{1}{2}\begin{bmatrix} 1 & 0 & 0 \\ 0 & 1 & 0 \\ 0 & 0 & 1 \\ -1 & 0 & 0 \end{bmatrix}$	$\frac{1}{2}\begin{bmatrix} 0 & 1 & 0 \\ 1 & 0 & 0 \\ 1 & 0 & 0 \\ 0 & 0 & 1 \end{bmatrix}$	$\frac{1}{2}\begin{bmatrix} 0 & 1 & 0 \\ 1 & 0 & 0 \\ -1 & 0 & 0 \\ 0 & 0 & 1 \end{bmatrix}$
8–11	$\frac{1}{2}\begin{bmatrix} 0 & 1 & 0 \\ 1 & 0 & 0 \\ 0 & 0 & 1 \\ 1 & 0 & 0 \end{bmatrix}$	$\frac{1}{2}\begin{bmatrix} 0 & 1 & 0 \\ 1 & 0 & 0 \\ 0 & 0 & 1 \\ -1 & 0 & 0 \end{bmatrix}$	$\frac{1}{2}\begin{bmatrix} 0 & 1 & 0 \\ 0 & 0 & 1 \\ 1 & 0 & 0 \\ 1 & 0 & 0 \end{bmatrix}$	$\frac{1}{2}\begin{bmatrix} 0 & 1 & 0 \\ 0 & 0 & 1 \\ 1 & 0 & 0 \\ -1 & 0 & 0 \end{bmatrix}$

Table 2.9: Codebook for Transmission on Antenna Ports {40,41,42,43} with $\nu = 4$ [2, Table 5.3.3A.2-5]

Codebook index	Number of layers $\nu = 4$
0	$\frac{1}{2}\begin{bmatrix} 1 & 0 & 0 & 0 \\ 0 & 1 & 0 & 0 \\ 0 & 0 & 1 & 0 \\ 0 & 0 & 0 & 1 \end{bmatrix}$

2.5 Reference Signal (RS)

The contents of this section are mainly taken from [3].

Two kinds of sequence are used in the LTE system for scrambling or generating RS:

- Pseudo-noise (PN) sequence: used for various purposes such as scrambling of RS, scrambling of DL and UL data transmissions, etc.
- Zadoff-Chu (ZC) sequences: used for primary synchronization signals, UL RS, UL PUCCH and random access channel (RACH).

2.5.1 Pseudo-Noise (PN) Sequence

The PN-sequence is defined by a length-31 Gold sequence as illustrated in Figure 2.8 [3]. The output sequence $c(n)$, where $n = 0, 1, ..., (M_{PN} - 1)$, is define by

$$c(n) = (x_1(n + N_C) + x_2(n + N_C)) \bmod 2,$$

where $N_C = 1600$ to discard the first 1600 samples . The first m-sequence is initialized as

$$x_1(n) = \begin{cases} 1, & n = 0, \\ 0, & 0<n<31, \end{cases}$$

the initialization of the second m-sequence is given by

$$c_{init} = \sum_{i=0}^{30} x_2(i) \cdot 2^i,$$

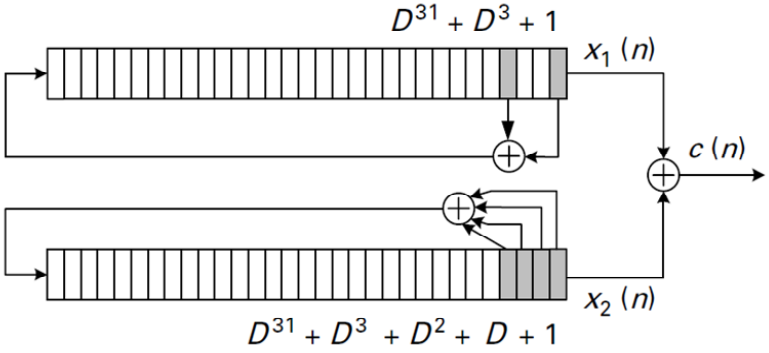

Figure 2.8: PN scrambling code generation in the LTE system [3, Fig. 9.2].

with the value depending on the application of the sequence. For example, when c_{init} is determined based on a cell ID of 63, that is $c_{init} = N_{ID}^{cell} = 63$, the second m-sequence $x_2(n)$ is initialized as

$$x_2(n) = \begin{cases} 1, & n<6, \\ 0, & 6 \leqslant n \leqslant 31. \end{cases}$$

2.5.2 Zadoff-Chu (ZC) Sequences

A ZC sequence of length N_{ZC} is defined as

$$x_u(m) = \begin{cases} e^{-j\frac{\pi u m^2}{N_{ZC}}}, & \text{when } N_{ZC} \text{ is even}, \\ e^{-j\frac{\pi u m(m+1)}{N_{ZC}}}, & \text{when } N_{ZC} \text{ is odd}, \end{cases}$$

with $m = 0, 1, ..., (N_{ZC} - 1)$, where u, the sequence index, is relatively prime with N_{ZC}.

For a fixed u, the periodic autocorrelation of a ZC sequence is zero for all time shifts other than zero. For different u values, ZC sequences are not orthogonal, but show low cross-correlation. If the sequence length N_{ZC} is a prime number, then there are $(N_{ZC} - 1)$ different sequences with periodic cross-correlation of $1/\sqrt{N_{ZC}}$ between any two sequences regardless of time shift.

2.5.3 Generation of RS Sequence

Two types of UL RS are supported:

- Demodulation RS (DMRS), associated with transmission of PUSCH or PUCCH.
- Sounding RS (SRS), not associated with transmission of PUSCH or PUCCH.

The same set of base sequences is used for DMRS and SRS. We introduce DMRS only.

RS sequence $r_{u,v}^{(\alpha)}(n)$ is defined by a cyclic shift α of a base sequence $\bar{r}_{u,v}(n)$ according to

$$r_{u,v}^{(\alpha)}(n) = e^{j\alpha n}\bar{r}_{u,v}(n), \quad 0 \leqslant n < M_{sc}^{RS},$$

where $M_{sc}^{RS} = mN_{sc}^{RB}$ is the length of the RS sequence and $1 \leqslant m \leqslant N_{RB}^{max,UL}$. Multiple RS sequences are defined from a single base sequence through different values of α.

Base sequences $\bar{r}_{u,v}(n)$ are divided into groups, where $u \in \{0, 1, ..., 29\}$ is the group number and v is the base sequence number within the group, such that each group contains one base sequence ($v = 0$) of each length $M_{sc}^{RS} = mN_{sc}^{RB}$, $1 \leqslant m \leqslant 5$, and two base sequences ($v = 0, 1$) of each length $M_{sc}^{RB} = mN_{sc}^{RB}$, $6 \leqslant m \leqslant N_{RB}^{max,UL}$.

The sequence group number u and the number v within the group may vary in time as described later. The definition of the base sequence $\bar{r}_{u,v}(0), ..., \bar{r}_{u,v}(M_{sc}^{RS} - 1)$ depends on the sequence length M_{sc}^{RS}.

For $M_{sc}^{RS} \geqslant 3N_{sc}^{RB}$, the base sequence $\bar{r}_{u,v}(0), ..., \bar{r}_{u,v}(M_{sc}^{RS} - 1)$ is given by

$$\bar{r}_{u,v}(n) = x_q(n \bmod N_{ZC}^{RS}), \quad 0 \leqslant n \leqslant M_{sc}^{RS},$$

where $x_q(m)$ is the qth root ZC sequence defined by

$$x_q(m) = e^{-j\frac{\pi q m(m+1)}{N_{ZC}^{RS}}}, \quad 0 \leqslant m \leqslant N_{ZC}^{RS} - 1,$$

with q given by

$$q = \lfloor \bar{q} + 1/2 \rfloor + v \cdot (-1)^{\lfloor 2\bar{q} \rfloor}, \ \bar{q} = N_{ZC}^{RS} \cdot (u+1)/31,$$

and the length N_{ZC}^{RS} of the ZC sequence given by the largest prime number such that $N_{ZC}^{RS} < M_{sc}^{RS}$.

For $M_{sc}^{RS} = N_{sc}^{RB}$ and $M_{sc}^{RS} = 2N_{sc}^{RB}$, the base sequence is given by

$$\bar{r}_{u,v}(n) = \ e^{j\phi(n)\pi/4}, \ \ 0 \leqslant n \leqslant M_{sc}^{RS} - 1,$$

where the value of $\phi(n)$ is given by Table 2.10 for $M_{sc}^{RS} = N_{sc}^{RS}$.

2.5.4 Demodulation Reference Signal (DMRS)

Figure 2.9 shows the placement of UL DMRS under normal CP. Note that there are two different kind of placement of DMRS, one for PUSCH and one for PUCCH. For PUSCH, the DMRS is placed on the fourth and eleventh symbols in a subframe, and for PUCCH, it is placed on the third, fourth and fifth symbols in a format-1 slot and the second and sixth symbols in a format-2 slot. The DMRS sequence $r_{PUSCH}^{\lambda}(\cdot)$ with layer $\lambda \in \{0, 1, ..., \nu - 1\}$ for PUSCH is defined by

$$r_{PUSCH}^{\lambda}(m \cdot M_{sc}^{RS} + n) = w^{\lambda}(m) r_{u,v}^{(\alpha_\lambda)}(n),$$

where $m = 0, 1, \ n = 0, ..., \ M_{sc}^{RS} - 1$, and $M_{sc}^{RS} = M_{sc}^{PUSCH}$.

Section 2.5.3 has defined the sequence $r_{u,v}^{(\alpha_\lambda)}(0), ..., r_{u,v}^{(\alpha_\lambda)}(M_{sc}^{RS} - 1)$. The orthogonal sequence $w^{(\lambda)}(m)$ is given by $\begin{bmatrix} w^{(\lambda)}(0) & w^{(\lambda)}(1) \end{bmatrix} = \begin{bmatrix} 1 & 1 \end{bmatrix}$ for DCI format 0, and other formats are given in Table 2.11.

The cyclic shift α_λ in a slot n_s is given as $\alpha_\lambda = 2\pi n_{cs,\lambda}/12$ with

$$n_{cs,\lambda} = (n_{DMRS}^{(1)} + n_{DMRS,\lambda}^{(2)} + n_{PN}(n_s)) \bmod 12,$$

Table 2.10: Definition of $\phi(n)$ for $M_{sc}^{RS} = N_{sc}^{RB}$ [2, Table 5.5.1.2-1]

u	$\phi(0), ..., \phi(11)$											
0	-1	1	3	-3	3	3	1	1	3	1	-3	3
1	1	1	3	3	3	-1	1	-3	-3	1	-3	3
2	1	1	-3	-3	-3	-1	-3	-3	1	-3	1	-1
3	-1	1	1	1	1	-1	-3	-3	1	-3	3	-1
4	-1	3	1	-1	1	-1	-3	-1	1	-1	1	3
5	1	-3	3	-1	-1	1	1	-1	-1	3	-3	1
6	-1	3	-3	-3	-3	3	1	-1	3	3	-3	1
7	-3	-1	-1	-1	1	-3	3	-1	1	-3	3	1
8	1	-3	3	1	-1	-1	-1	1	1	3	-1	1
9	1	-3	-1	3	3	-1	-3	1	1	1	1	1
10	-1	3	-1	1	1	-3	-3	-1	-3	-3	3	-1
11	3	1	-1	-1	3	3	-3	1	3	1	3	3
12	1	-3	1	1	-3	1	1	1	-3	-3	-3	1
13	3	3	-3	3	-3	1	1	3	-1	-3	3	3
14	-3	1	-1	-3	-1	3	1	-3	3	3	-1	1
15	3	-1	1	-3	-1	-1	1	1	3	1	-1	-3
16	1	3	1	-1	1	3	3	3	-1	-1	3	-1
17	-3	1	1	3	-3	3	-3	-3	3	1	3	-1
18	-3	3	1	1	-3	1	-3	-3	-1	-1	1	-3
19	-1	3	1	3	1	-1	-1	3	-3	-1	-3	-1
20	-1	-3	1	1	1	1	3	1	-1	1	-3	-1
21	-1	3	-1	1	-3	-3	-3	-3	-3	1	-1	-3
22	1	1	-3	-3	-3	-3	-1	3	-3	1	-3	3
23	1	1	-1	-3	-1	-3	1	-1	1	3	-1	1
24	1	1	3	1	3	3	-1	1	-1	-3	-3	1
25	1	-3	3	3	1	3	3	1	-3	-1	-1	3
26	1	3	-3	-3	3	-3	1	-1	-1	3	-1	-3
27	-3	-1	-3	-1	-3	3	1	-1	1	3	-3	-3
28	-1	3	-3	3	-1	3	3	-3	3	3	-1	-1
29	3	-3	-3	-1	-1	-3	-1	3	-3	3	1	-1

where the value of $n_{DMRS}^{(1)}$ is given by Table 2.12 according to the parameter "cyclicShift" provided by higher layers, $n_{DMRS,\lambda}^{(2)}$ is given by the cyclic shift for DMRS field in the most recent DCI format 0 [4] for the transport block associated with the corresponding PUSCH transmission where the values of $n_{DMRS}^{(2),\lambda}$ is given in Table 2.11 depending on some conditions.

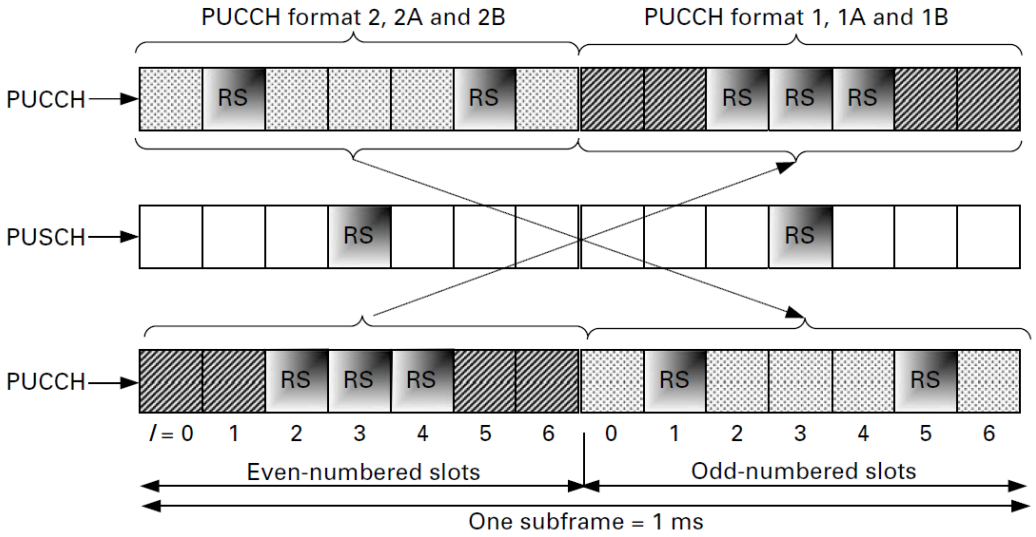

Figure 2.9: UL DMRS placement under normal CP [3, Fig. 9.18].

The first row of Table 2.11 is used to obtain $n^{(2)}_{DMRS,\lambda}$ and $w^{(\lambda)}(m)$ if there is no uplink-related DCI for the same transport block associated with the corresponding PUSCH transmission, and

- if the initial PUSCH for the same transport block is semi-persistently scheduled, or
- if the initial PUSCH for the same transport block is scheduled by the random access response grant.

The quantity $n_{PN}(n_s)$ is given by

$$n_{PN}(n_s) = \sum_{i=0}^{7} c(8N^{UL}_{symb} \cdot n_s + i) \cdot 2^i,$$

where the PN sequence $c(i)$ is defined in section 2.5.1. The application of $c(i)$ is cell-specific. The PN sequence generator is initialized with $c_{init} = \lfloor \frac{N^{cell}_{ID}}{30} \rfloor \cdot 2^5 + f^{PUSCH}_{ss}$ at the beginning of each radio frame.

Table 2.11: Mapping of Cyclic Shift Field in DCI Format 0 to $n^{(2)}_{DMRS,\lambda}$ and $w^{(\lambda)}(0), w^{(\lambda)}(1)$ [2, Table 5.5.2.1.1-1]

CS field in DCI format [4]	$n^{(2)}_{DMRS,\lambda}$				$\left[w^{(\lambda)}(0) \quad w^{(\lambda)}(1)\right]$			
	$\lambda=0$	$\lambda=1$	$\lambda=2$	$\lambda=3$	$\lambda=0$	$\lambda=1$	$\lambda=2$	$\lambda=3$
000	0	6	3	9	$\begin{bmatrix}1 & 1\end{bmatrix}$	$\begin{bmatrix}1 & 1\end{bmatrix}$	$\begin{bmatrix}1 & -1\end{bmatrix}$	$\begin{bmatrix}1 & -1\end{bmatrix}$
001	6	0	9	3	$\begin{bmatrix}1 & -1\end{bmatrix}$	$\begin{bmatrix}1 & -1\end{bmatrix}$	$\begin{bmatrix}1 & 1\end{bmatrix}$	$\begin{bmatrix}1 & 1\end{bmatrix}$
010	3	9	6	0	$\begin{bmatrix}1 & -1\end{bmatrix}$	$\begin{bmatrix}1 & -1\end{bmatrix}$	$\begin{bmatrix}1 & 1\end{bmatrix}$	$\begin{bmatrix}1 & 1\end{bmatrix}$
011	4	10	7	1	$\begin{bmatrix}1 & 1\end{bmatrix}$	$\begin{bmatrix}1 & 1\end{bmatrix}$	$\begin{bmatrix}1 & 1\end{bmatrix}$	$\begin{bmatrix}1 & 1\end{bmatrix}$
100	2	8	5	11	$\begin{bmatrix}1 & 1\end{bmatrix}$	$\begin{bmatrix}1 & 1\end{bmatrix}$	$\begin{bmatrix}1 & 1\end{bmatrix}$	$\begin{bmatrix}1 & 1\end{bmatrix}$
101	8	2	11	5	$\begin{bmatrix}1 & -1\end{bmatrix}$	$\begin{bmatrix}1 & -1\end{bmatrix}$	$\begin{bmatrix}1 & -1\end{bmatrix}$	$\begin{bmatrix}1 & -1\end{bmatrix}$
110	10	4	1	7	$\begin{bmatrix}1 & -1\end{bmatrix}$	$\begin{bmatrix}1 & -1\end{bmatrix}$	$\begin{bmatrix}1 & -1\end{bmatrix}$	$\begin{bmatrix}1 & -1\end{bmatrix}$
111	9	3	0	6	$\begin{bmatrix}1 & 1\end{bmatrix}$	$\begin{bmatrix}1 & 1\end{bmatrix}$	$\begin{bmatrix}1 & -1\end{bmatrix}$	$\begin{bmatrix}1 & -1\end{bmatrix}$

Table 2.12: Mapping of Cyclic Shift to $n^{(1)}_{DMRS}$ Values [2, Table 5.5.2.1.1-2]

Cyclic Shift	$n^{(1)}_{DMRS}$
0	0
1	2
2	3
3	4
4	6
5	8
6	9
7	10

The vector of reference signals is precoded according to

$$\begin{bmatrix} \tilde{r}^{(0)}_{PUSCH} \\ \vdots \\ \tilde{r}^{(P-1)}_{PUSCH} \end{bmatrix} = W \begin{bmatrix} r^{(0)}_{PUSCH} \\ \vdots \\ r^{(\nu-1)}_{PUSCH} \end{bmatrix}$$

where P is the number of antenna ports used for PUSCH transmission. For PUSCH transmission using a single antenna port, $P = 1$, $W = 1$ and $\nu = 1$. For spatial multiplexing, $P = 2$ or $P = 4$ and the precoding matrix W shall be identical to the precoding matrix used in Tables 2.5 to 2.8 for precoding of the PUSCH in the same subframe.

Chapter 3

Transmission System Structure and Channel Estimation

In this chapter, first we will introduce the system structure and signal model. Then we will describe several channel estimation techniques considered in the thesis.

3.1 Transmission System Structure

The transmission system structure is shown in Figure 3.1. To describe the overall transmission system in terms of a mathematical model that captures the essence, we follow the formulation of [10] for SISO systems, which is a rather commonly used matrix-vector formulation. And we extend it to MIMO systems. The baseband data signal vector x_d^{t,i_d} transported on the $t+1$th transmit antenna (we define first transmit antenna is $t=0$ and first receive antenna is $l=0$) after modulation in the i_dth SC-FDMA symbol interval is precoded by an M-point DFT matrix F_M as

$$X_d^{t,i_d} = F_M \cdot x_d^{t,i_d}, \tag{3.1}$$

where X_d^{t,i_d} is the data signal vector in FD. Note that, for PUSCH, there are 12 data symbols ($i_d = 0, 1, ..., 11$) in a subframe. The elements of the DFT matrix F_M are given by

$$[F_M]_{m_r m_c} = (1/\sqrt{M})\exp[-j2\pi m_r m_c/M], \tag{3.2}$$

where m_r and m_c denote the row and column indices, respectively, of the DFT matrix F_M, which is unitary, i.e., $F_M F_M^H = F_M^H F_M = I_M$.

In the LTE uplink, the RS sequences are determined according to the number of RBs used, as described in chapter 2. For an allocation of less than two RBs or larger than three RBs, the RS is generated from a CAZAC sequence and a ZC sequence, respectively, with length QN_{sc}^{RB}, where Q is the number of RBs and $N_{sc}^{RB} = 12$ is the RB size in the FD. The sequence $X_P^{t,i_P}(m)$ for LTE-A uplink is given by, for $0 \leq m < QN_{SC}^{RB}$,

$$X_P^{t,i_P}(m) = \begin{cases} \alpha(t) \cdot \exp[\frac{-j\pi qm(m+1)}{N_{ZC}}], & Q \geq 3, \\ \alpha(t) \cdot \exp[\frac{j\phi m\pi}{4}], & Q < 3, \end{cases} \tag{3.3}$$

where N_{ZC} is the length of ZC sequence and its value is the biggest prime number less than $M = QN_{SC}^{RB}$, i_P is the RS index in TD, and q is the sequence index which is relatively prime with N_{ZC}. The values of $\phi(m)$ all as given by Table 2.10. The number $\alpha(t)$ is a cyclic shift for transmit antenna t. Other details are described in section 2.5.2.

Note that, for PUSCH, there are 2 RS symbols ($i_P = 0, 1$) in a subframe. Unlike data signals, the RS is directly conveyed on subcarriers without precoding.

According to the LTE-A specifications, a time slot contains $N_{symb}^{slot} = 7$ SC-FDMA symbols under normal CP, and thus a subframe consisting of two consecutive time slots contains $N_{symb}^{sf} = 14$ SC-FDMA symbols under normal CP. The base station (BS) has to allocate different transmission bands to different users.

The precoded data signals and RS for different mobile stations (MSs) should be mapped to different bands in a given subframe. Consider PUSCH at normal CP let X_{sf}^t denote the $M \times N_{symb}^{sf}$ matrix of data and RS transmitted from antenna t in a subframe. Its kth column can be expressed as

$$\text{column}^{(k)} X_{sf}^t = \begin{cases} X_P^{t,\lfloor \frac{k}{N_{symb}^{slot}} \rfloor}, & k \bmod N_{symb}^{sf} = 3 \text{ or } 10, \\ X_d^{t,k-\lfloor \frac{2k}{N_{symb}^{slot}} \rfloor + \lfloor \frac{k}{N_{symb}^{slot}} \rfloor}, & \text{otherwise}, \end{cases} \tag{3.4}$$

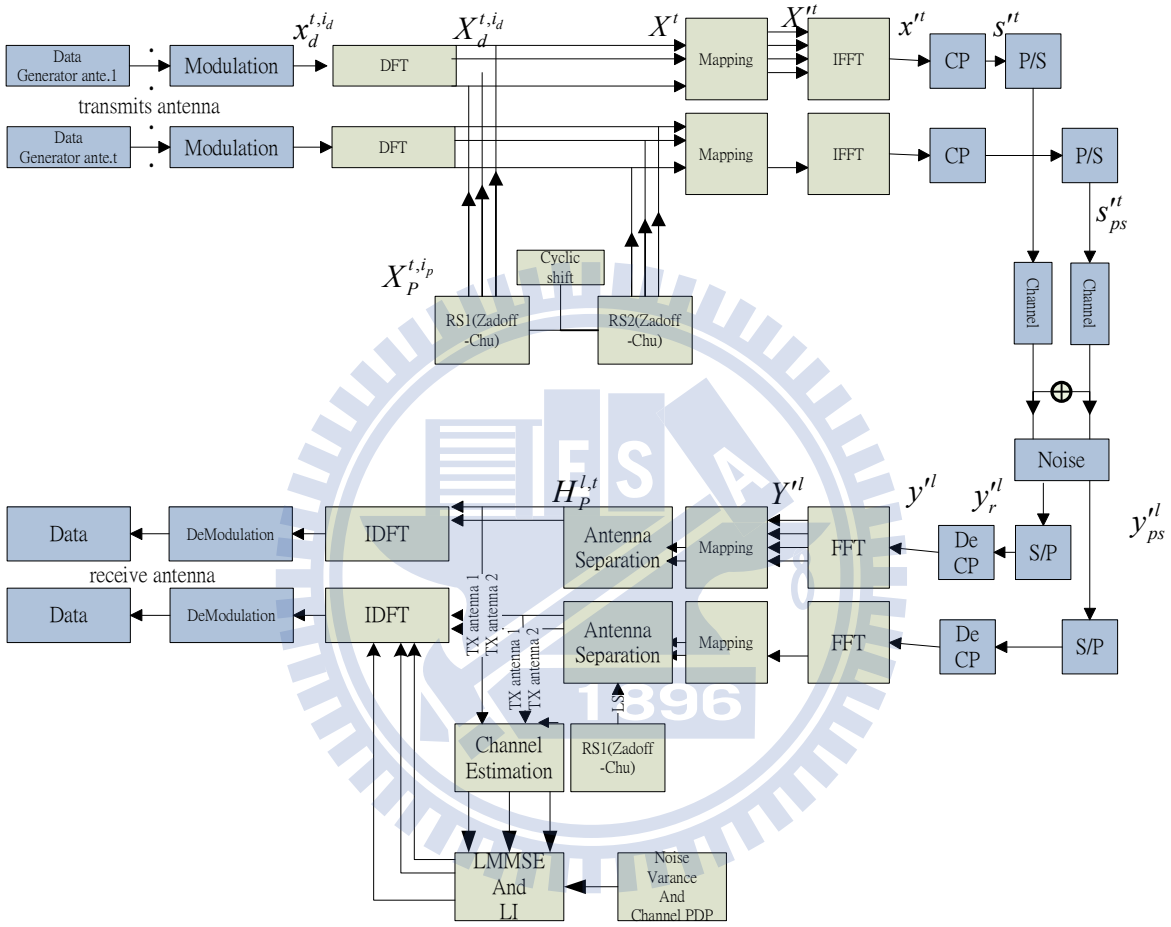

Figure 3.1: Transmission system structure.

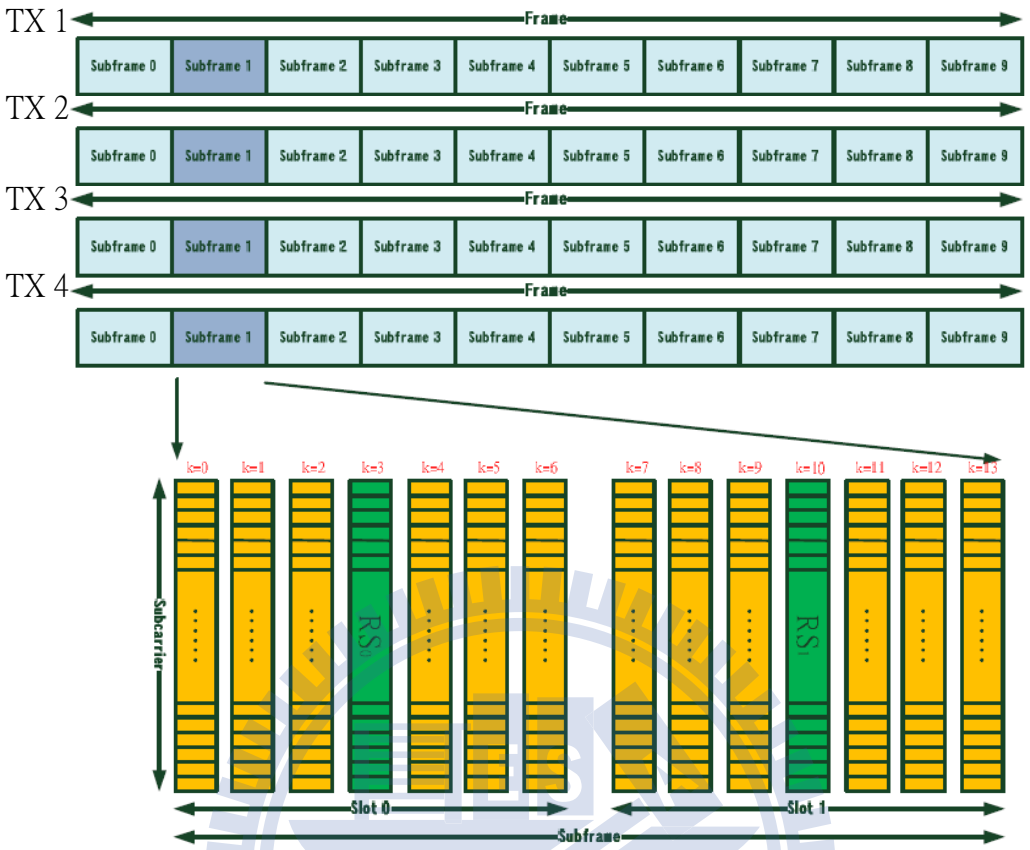

Figure 3.2: Frame structure for PUSCH [22, Figure 3.2].

where $X_P^{t,i_P} = [X_P^{t,i_P}(0)\ X_P^{t,i_P}(1)\ ...\ X_P^{t,i_P}(M-1)]^T$. Figures 3.2 shows the data and RS allocation in a subframe in more detail. The signals entering the IFFT in the transmitter can be expressed as

$$X'^t = [X^{t,0}\ X^{t,1}\ ...\ X^{t,(N_{symb}^{sf}-1)}] = A \cdot X_{sf}^t, \tag{3.5}$$

where X'^t is an $N \times N_{symb}^{sf}$ matrix and A is the matrix used to map the signals to the subcarriers in the assigned RBs, which can be written as

$$A = \begin{bmatrix} 0_{\nu \times M} \\ I_{M \times M} \\ 0_{(N-M-\nu) \times M} \end{bmatrix}_{N \times M}. \tag{3.6}$$

Note that ν depends on the user and $0 \leqslant \nu \leqslant N - M$, N is the FFT size and $N > M$.

Then, X'^t is transformed into the TD by an N-point IFFT operator F_N^H as

$$x'^t = [x^{t,0}\ x^{t,1}\ ...\ x^{t,N_{symb}^{sf}-1}] = F_N^H \cdot X'^t. \tag{3.7}$$

Before transmission, CP is added to the TD signals to yield $s^{t,k}$ for $x^{t,k}$, $k = 0, ..., N_{symb}^{sf} - 1$, where for k mod $(N_{symb}^{slot} - 1) = 0$,

$$s^{t,k} = \begin{bmatrix} 0_{cp_1 \times (N-cp_1)} & I_{cp_1 \times cp_1} \\ & I_N \end{bmatrix} \cdot x^{t,k}, \tag{3.8}$$

and for k mod $(N_{symb}^{slot} - 1) \neq 0$,

$$s^{t,k} = \begin{bmatrix} 0_{cp_2 \times (N-cp_2)} & I_{cp_2 \times cp_2} \\ & I_N \end{bmatrix} \cdot x^{t,k}, \tag{3.9}$$

with $\text{cp}_1 = 160 \times N/2048$ and $\text{cp}_2 = 144 \times N/2048$. The transmitted signal s'^t after CP insertion can be written as

$$s'^t = [s^{t,0}\ s^{t,1}\ ...\ s^{t,N_{symb}^{sf}-1}]. \tag{3.10}$$

Note that the length of CP for the first symbol in a slot is different from others in length, and hence s'^t is not a rectangular matrix.

We concatenate the columns of S'^t together to yield the transmitted sequence $s_{ps}'^t$ as

$$s_{ps}'^t = \begin{bmatrix} [s^{t,0}]^T & [s^{t,1}]^T & ... & [s^{t,N_{symb}^{sf}-1}]^T \end{bmatrix}^T, \tag{3.11}$$

which includes data and pilots. It is transmitted through the wireless channel.

The BS receives the signals from the UEs. The received signal on the receive antenna l at the BS can be written as

$$y_{ps}'^l = \sum_t h_{l,t} * s_{ps}'^t + w_n = \begin{bmatrix} [y_r^{l,0}]^T & [y_r^{l,1}]^T & ... & [y_r^{l,N_{symb}^{sf}-1}]^T \end{bmatrix}^T, \tag{3.12}$$

where $h_{l,t}$ is the complex channel impulse response (CIR) from transmit antenna t to receive antenna l, $*$ denotes convolution, w_n is white Gaussian noise, and $y_r^{l,k}$ is the kth received

SC-FDMA symbol in the subframe. After removing the CP for each received symbol, we obtain, for $k = 0, \cdots, N_{symb}^{sf} - 1$,

$$y'^{l,k} = G'_{cp_1} \cdot y_r^{l,k} = \left[\begin{array}{cc} 0_{cp_1 \times N} & I_{N \times N} \end{array} \right] \cdot y_r^{l,k} \tag{3.13}$$

if $k \bmod (N_{symb}^{slot} - 1) = 0$ and

$$y'^{l,k} = G'_{cp_2} \cdot y_r^{l,k} = \left[\begin{array}{cc} 0_{cp_2 \times N} & I_{N \times N} \end{array} \right] \cdot y_r^{l,k} \tag{3.14}$$

otherwise. Now let

$$y'^{l} = \left[\begin{array}{cccc} y'^{l,0} & y'^{l,1} & ... & y'^{l,N_{symb}^{sf}-1} \end{array} \right], \tag{3.15}$$

which is a matrix of the received signal for the whole subframe (including data and RS) after CP removal.

Transforming the received signal in (3.15) to the FD using N-point FFT, we get

$$Y'^{l} = F_N \cdot y'^{l} = \left[\begin{array}{cccc} Y^{l,0} & Y^{l,1} & ... & Y^{l,N_{symb}^{sf}-1} \end{array} \right]. \tag{3.16}$$

Then the de-mapping in the assigned RBs can be written as

$$Y^l = A^T Y'^l. \tag{3.17}$$

Let $Y^{l,k}$ be the kth column of Y^l, where $k = 0, ..., N_{symb}^{sf} - 1$. In PUSCH since the fourth symbol of each slot contains RS and the others contain data, define

$$Y_{RS}^{l,\lfloor \frac{k}{N_{symb}^{slot}} \rfloor} = Y^{l,k} \tag{3.18}$$

if $k \bmod N_{symb}^{sf} = 3$ or 10, and

$$Y_d^{l,k-\lfloor \frac{2k}{N_{symb}^{slot}-1} \rfloor + \lfloor \frac{k}{N_{symb}^{slot}-1} \rfloor} = Y^{l,k} \tag{3.19}$$

otherwise. The FD RS signal in (3.18) can be expressed as

$$Y_{RS}^{l,i_P} = \sum_t H_P^{l,t} \cdot X_P^{t,i_P} + W_n, \tag{3.20}$$

where $H_P^{l,t}$ is the FD channel gain matrix between transmit antenna t and receive antenna l, i_P is RS symbol index and W_n is the AWGN vector in FD.

In the next section, we will first introduce several channel estimation techniques. Then we will use equation (3.20) in these techniques to arrive at a solution for channel estimation.

3.2 SISO Channel Estimation Methods

Recall that the transmitted signal are divided into data signals and reference signals. The data signals contain user data and the reference signals contain data known to the transmitter and the receiver. The latter signals are used for channel estimation. In addition, for fading channels the channel responses must be constantly tracked; so the reference signal must be constantly transmitted.

For a time-varying multipath channel the channel responses varier both in time and in frequency. In this section we will describe some channel estimation methods for frequency-selective time-varying single-input single-output (SISO) systems. Then in the next section we will extend them to multiple-input multiple-output (MIMO) systems.

3.2.1 Least-Squares (LS) Estimation

Based on the a priori known data (i.e., RS), we can estimate the channel response on the RS carriers roughly by LS estimation. The LS estimation minimizes the squared error [11]. In this section, we omit antenna indices t and l for simplicity, because we only consider SISO transmission, In LS channel estimation for a specific RS symbol i_P, we minimize.

$$\|Y_{RS} - \hat{H}_{P,LS} \cdot X_P\|^2, \tag{3.21}$$

where Y_{RS} is the received RS signal after passing through the channel and X_P is the a priori known RS signal, both in the FD and both being $M \times 1$ vectors where M is the DFT

(precoder) size. The quantities in (3.21) can be written in terms of their element as

$$Y_{RS} = [Y_{RS}(0)\ Y_{RS}(1)\ ...\ Y_{RS}(M-1)]^T, \tag{3.22}$$

$$X_P = [X_P(0)\ X_P(1)\ ...\ X_P(M-1)]^T, \tag{3.23}$$

and

$$\hat{H}_{P,LS} = \begin{bmatrix} \hat{H}_{P,LS}(0) & ... & 0 & ... \\ 0 & \hat{H}_{P,LS}(1) & 0 & ... \\ 0 & ... & \hat{H}_{P,LS}(2) & ... \\ 0 & ... & 0 & \hat{H}_{P,LS}(M-1) \end{bmatrix}. \tag{3.24}$$

The LS channel estimate at subcarrier m, based on one observed SC-FDMA symbol Y_{RS} only, is given by

$$\hat{H}_{P,LS}(m) = \frac{Y_{RS}(m)}{X_{RS}(m)} = H_P + W_n(m)/X_{RS}(m), \tag{3.25}$$

where $m = 0, ..., M-1$, and $W_n(m)$ is the complex white Gaussian noise at subcarrier m.

3.2.2 Frequency Domain Noise Reduction

In order to lower the noise in the LS channel estimate, we follow it by a frequency-domain noise reduction operation. In this subsection we will describe two methods. The first is the linear minimum mean-square error (LMMSE) estimator [10], which assumes a known channel power delay profile (PDP) and a known channel noise variance. But LMMSE is rather complex, so we research on how to reduce the complexity. The second method is windowing, which is similar to the constant windowing of [10]. However, propose a more appropriate window shape, namely, the Gaussian window (GWD). This method only requires knowing the variance of the channel noise to estimate the channel response and does not require knowing the channel PDP.

Linear Minimum-Mean Square Error (LMMSE)

The linear minimum mean square error (LMMSE) estimator uses second-order statistics about the channel and the noise to reduce the amount of noise in the LS channel estimate as

$$\hat{H}_{P,LMMSE} = R'_C[R'_C + \sigma_W^2(X_{P,diag}^H X_{P,diag})]^{-1}\hat{H}_{P,LS} \tag{3.26}$$

where R'_C is the channel autocovariance matrix, σ_W^2 is the AWGN noise variance, and $X_{P,diag}$ is a diagonal matrix of RS signal values. Note that $X_{P,diag}^H X_{P,diag}$ is an identity matrix because the ZC sequence is a complex exponential signal. Because we map the transmitted signal and de-map the received signal to the subcarriers in the assigned RBs, R'_C can be written as $R'_C = A^T R_C A$ where R_C is the channel autocovariance matrix over all subcarriers as

$$R_C = E[C_n C_n^H] = E[F_N c_n c_n^H F_N^H] = F_N R_c F_N^H, \tag{3.27}$$

where $C_n = F_N \cdot c_n$ is the channel frequency response vector at time n,

$$c_n \equiv [h_{n,0}, h_{n,1}, \cdots, h_{n,L_c-1}, 0, \cdots, 0]^T, \tag{3.28}$$

is the CIR vector at time n with L_c being the length of the CIR, and $R_c = E[c_n c_n^H]$. For a WSSUS channel, R_c is an $N \times N$ diagonal matrix of the channel PDP as

$$R_c = diag([P_0, \cdots, P_{l_c}, \cdots, P_{L_c-1}, 0, \cdots, 0]^T). \tag{3.29}$$

Direct use of (3.26) may run into some problems. First, if the σ_W^2 is very small, then the matrix to be inverted may have a very large condition number, which causes numerical problem in computing the inversion. Therefore, we may take the SVD of R'_C as $R'_C = U\Lambda U^H$, which results in

$$\hat{H}_{P,LMMSE} = R'_C[R'_C + \sigma_W^2 I_M]^{-1}\hat{H}_{P,LS} = U\Delta U^H \hat{H}_{P,LS} \tag{3.30}$$

where Δ is a diagonal matrix, whose i_{eg}th elements are given by

$$\delta_{i_{eg}} = \frac{\lambda_{i_{eg}}}{\lambda_{i_{eg}} + \sigma_W^2} \qquad i_{eg} = 0, 1, \cdots, M-1, \tag{3.31}$$

with $\lambda_{i_{eg}}$ being the i_{eg}th eigenvalue of R'_C, arranged in descending numerical order. We may then keep only a subset of the eigenvalues, say r_{eg}, and set the others to zero as

$$\delta_{i_{eg}} = \begin{cases} \frac{\lambda_{i_{eg}}}{\lambda_{i_{eg}} + \sigma_W^2}, & i_{eg} = 0, 1, \cdots, r_{eg} - 1, \\ 0, & i_{eg} = r_{eg}, \cdots, M-1. \end{cases} \tag{3.32}$$

Then we may replace the matrix inverse by pseudo-inverse.

This method not only solves the matrix inversion problem, but also lowers the complexity. Without SVD the computation of (3.26) requires $O(M^3)$ flops (floating-point operations); after SVD, it reduces to $O(r_{eg}M^2)$. The complexity formula is recorded in the [17].

Secondly, we explore another method to reduce the complexity problem associated with matrix inversion. For this, note that the physical meaning of LMMSE is to use channel responses at nearby subcarriers to help minimize the estimation error. The subcarriers that are farther away are not important. Hence we may consider a segmented way of computing $H_{P,LMMSE}$ as illustrated in Figure 3.3, left plot, where each segment requires only the inversion of a smaller matrix and thus a lower complexity. Note that the submatrix size should depend on the coherence bandwidth of the channel. Typically, the shorter the channel PDP, the larger the coherence bandwidth. Conversely, the longer the PDP, the smaller the coherence bandwidth.

A problem with the submatrix organization shown in Figure 3.3's left plot is that the subcarriers near the corners of each submatrix are not treated in a "balanced" way as those at the center. In order to solve this problem we let the submatrices overlap, as shown in Figure 3.3, right plot. This will calculate some matrix in inversions the sections that were not calculated previously, increasing estimation accuracy level at a higher complexity.

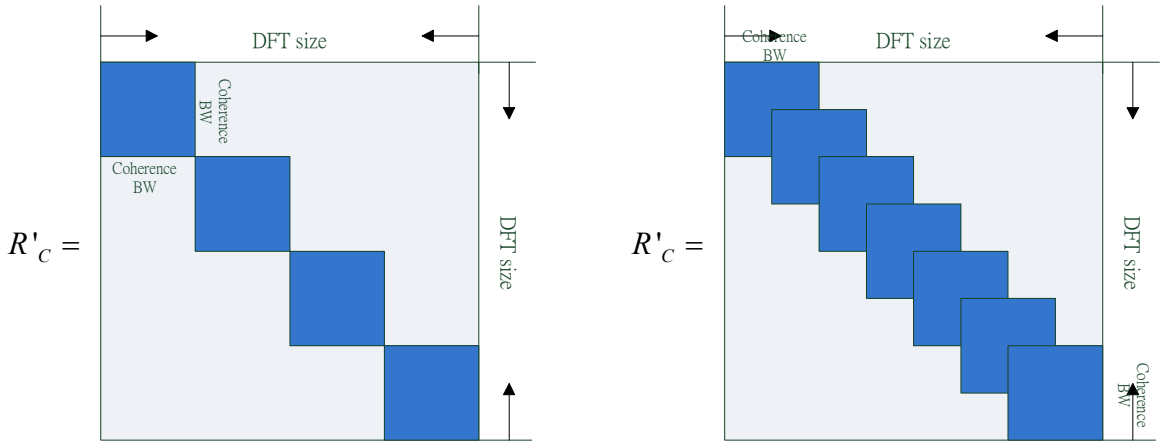

Figure 3.3: Two ways to reduce the computational complexity of the inversion of the auto-correlation matrix in LMMSE channel estimation.

Either way the number of multiplications in the estimation calculation will be reduced from $M^3 + 2M^2$ to $S_L^3 + 2(2Q-1)S_L^2$, where S_L is the submatrix size, and Q is the number of submatrices. The complexity formula is recorded in the [17].

Frequency-Domain Windowing

LMMSE estimator's complexity is quite high. Even with the above complexity-reduction means, the required amount of computation is still considerable. So we also propose a windowing method in the frequency domain for noise reduction at a lower complexity. Reference [10] proposes a method using a of constant window (CWD). Its basic principle is to average over the frequency responses within the coherence bandwidth. This method can reduce channel estimation errors in low signal-to-noise-ratios (SNRs), but can increase them in high SNRs.

We propose to use a kind of Gaussian window (GWD) which can be interpreted as premultiplying the estimated channel frequency response (CFR) vector by a matrix as shown in Figure 3.4. Each row of the channel windowing matrix takes average over a number

of nearby CFR samples with Gaussian weighting where the standard deviation σ of the Gaussian distribution depends on the SNR as shown in Table 3.1 and the equation is written in (3.34). The window is defined mathematically as

$$[D_R] = \begin{cases} G[-(m_c - m_r) + \lfloor \frac{S_G}{2} \rfloor], & \text{if } 1 - \lfloor \frac{S_G}{2} \rfloor \leq m_c - m_r \leq \lceil \frac{S_G}{2} \rceil, \\ 0, & \text{otherwise ,} \end{cases} \tag{3.33}$$

where

$$G[i] = \frac{S_G}{\text{OS}} \cdot \frac{1}{\sigma\sqrt{2\pi}} \exp(-\frac{i^2}{2\sigma^2}), \qquad 1 - \lfloor \frac{S_G}{2} \rfloor \leq i \leq \lceil \frac{S_G}{2} \rceil,$$

with

$$\text{OS} = \sum_{i=1}^{S_G} \frac{1}{\sigma\sqrt{2\pi}} \exp(-\frac{i^2}{2\sigma^2}),$$
$$\sigma = 10^{(3-\frac{SNR}{10})}, \tag{3.34}$$

and S_G being the length of Gaussian sequence based on the coherence bandwidth. We will compare different values of S_G in the next chapter. This design uses the Gaussian distribution characteristic, based on the variance of the noise, to change the subcarrier weights in the average. The further a subcarrier is away from another subcarrier, the smaller the correlation in channel responses, and hence the weight is smaller. Conversely, the larger the correlation, the larger the weight. This can mitigate the problem of increase in channel estimation error of CWD in high SNR, and it does not require knowing the complete channel PDP.

3.2.3 Time Domain Estimation

After obtaining the channel response estimates for the RS symbols, we can proceed to obtain the channel response estimates for the data symbols, which requires time-domain filtering (see Fig. 3.2).

Table 3.1: Dependence of Standard Deviation of Gaussian Distribution on SNR

SNR (dB)	Gaussian distributed standard deviation
0	1000
10	100
20	10
30	1
40	0.1
50	0.01

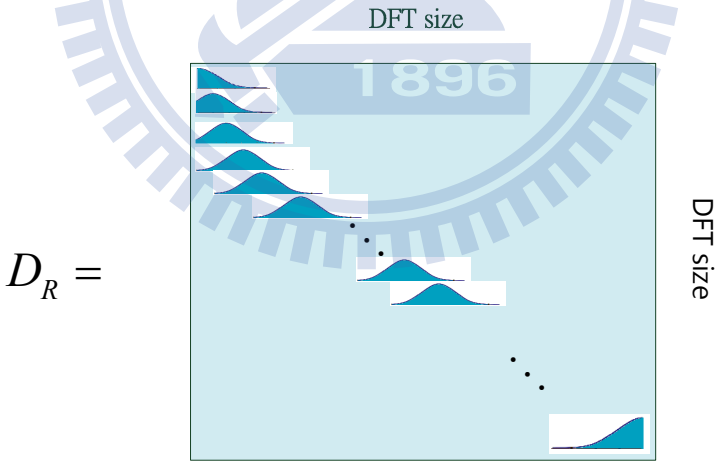

Figure 3.4: Gaussian distributed windowing matrix for noise reduction.

Linear Interpolation in TD

In this thesis, we only consider first-order polynomial interpolation that is, linear interpolation, based on two nearest reference points. Mathematically, suppose we have two points (x_1, y_1) and (x_2, y_2) that are assumed to satisfy a linear equation as

$$aX + b = Y, \tag{3.35}$$

where a and b are unknown. Then we have

$$ax_1 + b = y_1, \quad ax_2 + b = y_2.$$

We can write the equation in matrix form as

$$\begin{bmatrix} x_1 & 1 \\ x_2 & 1 \end{bmatrix} \begin{bmatrix} a \\ b \end{bmatrix} = \begin{bmatrix} y_1 \\ y_2 \end{bmatrix}. \tag{3.36}$$

Then the unknown parameters a and b can be solved as

$$\begin{bmatrix} a \\ b \end{bmatrix} = \begin{bmatrix} x_1 & 1 \\ x_2 & 1 \end{bmatrix}^{-1} \begin{bmatrix} y_1 \\ y_2 \end{bmatrix} = \frac{1}{x_2 - x_1} \begin{bmatrix} y_2 - y_1 \\ x_2 y_1 - x_1 y_2 \end{bmatrix}. \tag{3.37}$$

The above interpolation is carried out for each subcarrier in a data symbol in the TD between two RS subcarriers at the same frequency. The idea is illustrated in Figure 3.5.

3.3 MIMO Channel Estimation Techniques

LTE only supports use of one antenna in uplink transmission. In other words, it precludes single-user MIMO in uplink transmission. In LTE-A, in order to increase data throughput, the allowed number of transmission antennas for the UE is increased to four, facilitating MIMO transmission in the uplink, it can also support MU MIMO transmission. This section considers SU MIMO channel estimation, MU MIMO also use these methods (we analyze in future work).

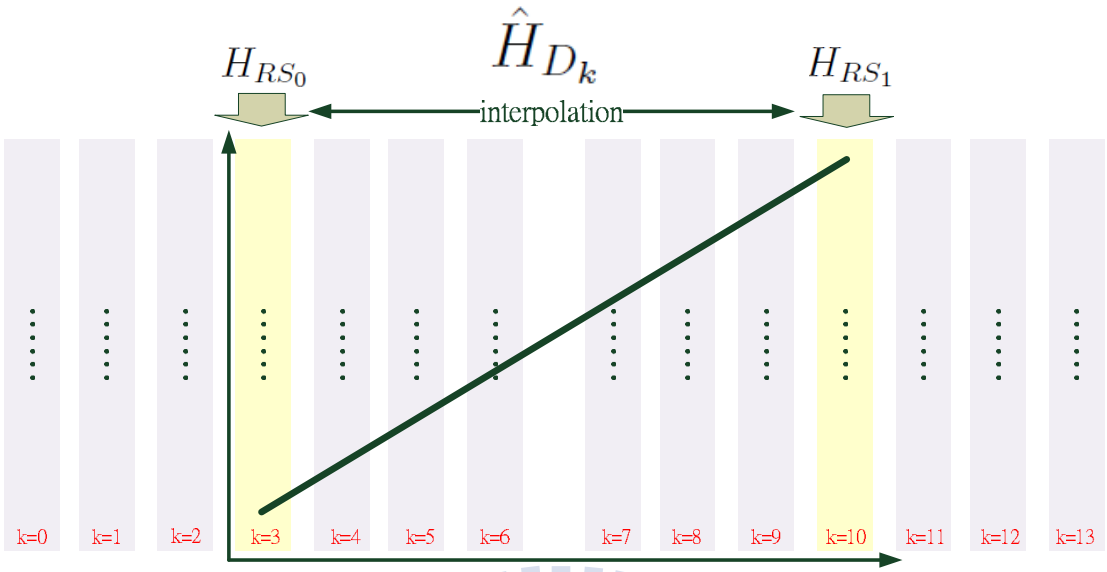

Figure 3.5: Illustration of linear interpolation in TD in a subframe.[22, Figure 3.4]

3.3.1 Demodulation Reference Signal (DMRS) Design

In section 2.5.4, we introduced the DMRS design in LTE-A. We can see that the parameter α_λ has different values for different antennas. That is to say, the DMRS transmitted by each antenna has a different linear phase shift. In the case of four antennas, we know from Table 2.11 that the antennas' $n^{(2)}_{DMRS}$ values are different by 3 which is one-fourth of N^{RB}_{sc}. That is, the four antennas evenly divide the phase. In the case of two antennas, we only consider $\lambda = 0$ and $\lambda = 1$ in Table 2.11, and the antennas' $n^{(2)}_{DMRS}$ values are different by 6. That is, the two antennas also evenly divide the phase. We repeat two relevant equations from section 2.5.4 below:

$$\alpha_\lambda = 2\pi n_{CS,\lambda}/12, \tag{3.38}$$

$$n_{CS,\lambda} = (n^{(1)}_{DMRS} + n^{(2)}_{DMRS} + n_{PN}(N_s))\text{mod}12. \tag{3.39}$$

The four phase for the case of four antennas are illustrated in Figure 3.6.

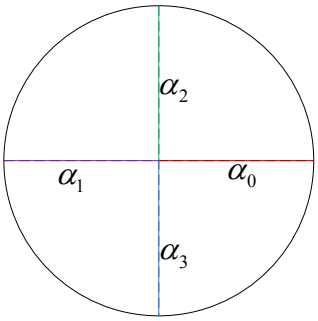

Figure 3.6: Cyclic shift by even phase division via α_λ.

3.3.2 Channel Separation

In an MIMO system, a receive antenna will receive the sum signal transmitted from all transmit antennas. In order to accurately estimate the channel response associated with each transmit antenna, the channel responses should be separable by proper signal design. We introduce two channel estimation methods, using the property of the previously described DMRS cyclic shift. The first is that of [13] and [19], which does TD channel separation. The second method is an FD technique that is built on the concept of coherence bandwidth, which we will introduce shortly.

Time Domain Channel Separation

With DMRS cyclic shift, (3.20) can be rewritten as

$$Y_{RS}^{l} = \sum_{t} H_{P}^{l,t} \cdot X_{P.} * \alpha_t' + W_n, \tag{3.40}$$

where we have dropped the superscript i_p because we will concentrate on one RS symbol in the present discussion. In the above equation, we have also let $\alpha_t' = \begin{bmatrix}\alpha_t'(0) & \alpha_t'(1) & \cdots & \alpha_t'(M-1)\end{bmatrix}^T$ where $\alpha_t'(m) = e^{j\alpha_t m}$, $0 \le m \le M$, is the cyclic shift for the $(t+1)$th transmit antenna, X_P is the X_P^{0,i_p} in (3.20) for the first transmit antenna, and the notation $.*$ denotes element-

wise product as in MATLAB. The "channel separation" block in Figure 3.7 work as follows. After FFT on the received reference signal to obtain Y_{RS}^l, we multiply it with the complex conjugate of $X_P. * \alpha_0'$ to obtain

$$\hat{H}_P^l \equiv Y_{RS}^l. * \text{conj}(X_P. * \alpha_0') = \sum_t H_P^{l,t} \cdot [\alpha_t'. * \text{conj}(\alpha_0')] + W_n. * \text{conj}(X_P. * \alpha_0'), \tag{3.41}$$

where conj$(\cdot)$ denotes the complex conjugate operation. Note that

$$[\alpha_t'. * \text{conj}(\alpha_0')]_m = e^{j(\alpha_t - \alpha_0)m}.$$

The above is simply LS channel estimation.

In the absence of noise, from the derivation in section 3.1 we see that

$$\hat{H}_P^l = \frac{A^T F_N \hat{h}_P^l F_N^H A}{N} \cdot (\alpha_t'. * \text{conj}(\alpha_0')) \tag{3.42}$$

where $\hat{h}_P^l$ is the corresponding CIR estimation (corresponding to $\hat{H}_P^l$). After mapping and IFFT, we have

$$F_N^H A \cdot \hat{H}_P^l = F_N^H A \frac{A^T F_N \hat{h}_P^l F_N^H A}{N} \cdot (\alpha_t'. * \text{conj}(\alpha_0')) \simeq \frac{\hat{h}_P^l}{N} F_N^H A \cdot (\alpha_t'. * \text{conj}(\alpha_0')). \tag{3.43}$$

Therefore, we see that the frequency domain phase shift causes time domain shift of the CIR, as illustrated in Figure 3.8 for 2×2 MIMO and in Figure 3.9 for 4×4 MIMO. The different CIRs from the different transmit antennas to any one receive antenna are evenly spread over one symbol interval. The TD channel separation method thus uses a window to separate the CIRs and then does an FFT to transform to the FD. The "window filter" can be described in matrix form as

$$A_s^t = diag(D(n,t)), \tag{3.44}$$

where

$$D(n,t) = \begin{cases} 1, & t \cdot \frac{N}{T} - \lfloor \frac{R_l}{2} \rfloor \le n \le t \cdot \frac{N}{T} + \lfloor \frac{R_l}{2} \rfloor, \quad t \neq 0 \\ 1, & n \ge 1 + \lfloor \frac{R_l}{2} \rfloor, \quad n \le N - \lfloor \frac{R_l}{2} \rfloor, \quad t = 0 \\ 0, & \text{otherwise} \end{cases}$$

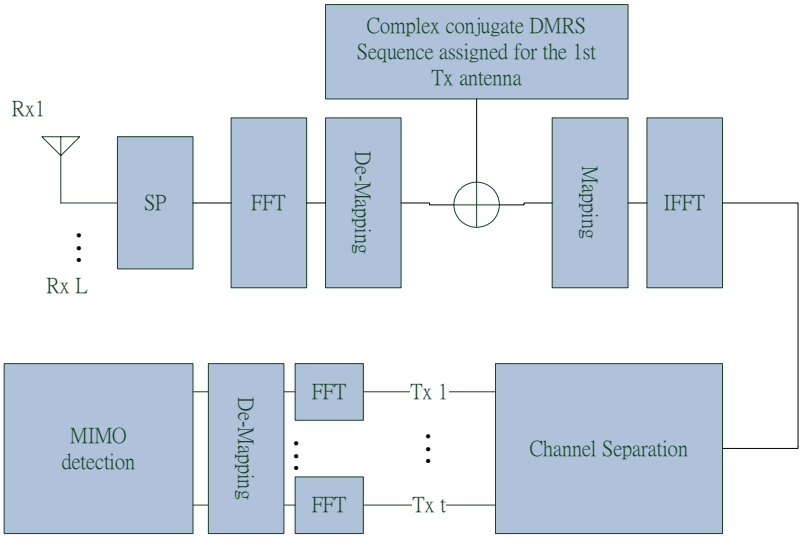

Figure 3.7: Time domain channel separation.

with R_l being the assumed length of each CIR. After FFT and de-mapping, we get

$$\hat{H}_P^{l,t} = A^T F_N A_s^t F_N^H A \cdot \hat{H}_P^l. \tag{3.45}$$

The time domain channel separation method requires adding a set of FFT and IFFT to the receiver. If there are multiple antennas, the number of added FFT and IFFT will also multiply, and the complexity will also increase. More importantly, because it uses time shift to distinguish the channels of different transmission antennas, these is a leakage power problem which increase the channel estimation error [13]. So we develop another method, namely, the FD channel separation method.

Frequency Domain Channel Separation

To motivate this method, note that from Table 2.11, the phase difference between two antenna channels, in a two-transmit-antenna case, is such that it alternates between 0 and π for successive subcarriers, as shown in Figure 3.10. The first column depicts the composite received signal at receive antennas l from transmit antenna 0 and 1, after multiplying with

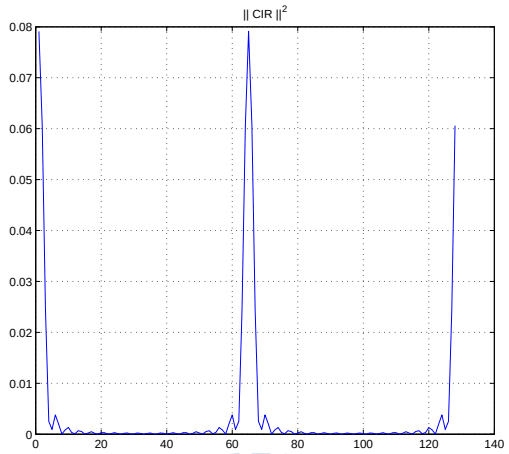

Figure 3.8: Composite CIR obtained LS channel estimation in 2×2 MIMO.

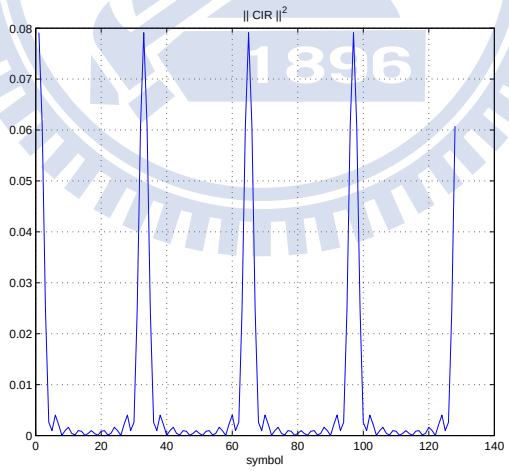

Figure 3.9: Composite CIR obtained LS channel estimation in 4×4 MIMO.

the complex conjugate of the RS from transmit antenna 0. Assume that the coherence bandwidth is such that the channel responses do not differ much between two successive subcarriers. Then for each pairs of subcarriers, say m and $m+1$, the channel responses can be estimated by solving the system of linear equations

$$\begin{cases} \hat{H}_P^{l,0}(m) + \hat{H}_P^{l,1}(m) = \hat{H}_P^l(m), \\ \hat{H}_P^{l,0}(m+1) - \hat{H}_P^{l,1}(m+1) = \hat{H}_P^l(m+1). \end{cases} \tag{3.46}$$

To solve these equations we can multiply with an $M \times M$ matrix Q_t for antenna t, as shown in Figure 3.10's last two columns, where

$$Q_t = \begin{cases} \frac{1}{2}\begin{bmatrix} 1 & 1 & 0 & 0 & \cdots & 0 \\ 0 & 1 & 1 & 0 & \cdots & 0 \\ \vdots & & \ddots & \ddots & & \vdots \\ & & & 1 & 1 & 0 \\ & & & 0 & 1 & 1 \\ 0 & \cdots & & 0 & 1 & 1 \end{bmatrix}, & t = 0, \\ \frac{1}{2}\begin{bmatrix} 1 & -1 & 0 & 0 & \cdots & 0 \\ 0 & -1 & 1 & 0 & \cdots & 0 \\ \vdots & & \ddots & \ddots & & \vdots \\ & & & -1 & 1 & 0 \\ & & & 0 & 1 & 1 \\ 0 & \cdots & & 0 & 1 & 1 \end{bmatrix}, & t = 1. \end{cases} \tag{3.47}$$

When there are four antennas in the transmitter, we use a system of four linear equations to obtain the solution:

$$\begin{cases} \hat{H}_P^{l,0}(m) + \hat{H}_P^{l,1}(m) + \hat{H}_P^{l,2}(m) + \hat{H}_P^{l,3}(m) = \hat{H}_P^{l,t}(m), \\ \hat{H}_P^{l,0}(m+1) + j\hat{H}_P^{l,1}(m+1) - \hat{H}_P^{l,2}(m+1) - j\hat{H}_P^{l,3}(m+1) = \hat{H}_P^{l,t}(m+1), \\ \hat{H}_P^{l,0}(m+2) - \hat{H}_P^{l,1}(m+2) + \hat{H}_P^{l,2}(m+2) - \hat{H}_P^{l,3}(m+2) = \hat{H}_P^{l,t}(m+2), \\ \hat{H}_P^{l,0}(m+3) - j\hat{H}_P^{l,1}(m+3) - \hat{H}_P^{l,2}(m+3) + j\hat{H}_P^{l,3}(m+3) = \hat{H}_P^{l,t}(m+3). \end{cases} \tag{3.48}$$

Similar to (3.26), the equations can be solved by multiplying with some $M \times M$ matrices Q_t

as given by

$$Q_t = \begin{cases} \frac{1}{4}\begin{bmatrix} 1 & 1 & 1 & 1 & 0 & \cdots & 0 \\ 0 & 1 & 1 & 1 & 1 & 0 & 0 \\ \vdots & \ddots & \ddots & \ddots & \ddots & \ddots & \vdots \\ & & & \ddots & & & \\ & & & & & & 0 \\ & & & 1 & 1 & 1 & 1 \\ 0 & \cdots & 0 & 1 & 1 & 1 & 1 \end{bmatrix}, & t = 0, \\ \frac{1}{4}\begin{bmatrix} 1 & j & -1 & -j & 0 & \cdots & 0 \\ 0 & j & -1 & -j & 1 & 0 & 0 \\ \vdots & \ddots & \ddots & \ddots & \ddots & \ddots & \vdots \\ & & & \ddots & & & \\ & & & & & & 0 \\ & & & -j & 1 & j & -1 \\ 0 & \cdots & 0 & -j & 1 & j & -1 \end{bmatrix}, & t = 1, \\ \frac{1}{4}\begin{bmatrix} 1 & -1 & 1 & -1 & 0 & \cdots & 0 \\ 0 & -1 & 1 & -1 & 1 & 0 & 0 \\ \vdots & \ddots & \ddots & \ddots & \ddots & \ddots & \vdots \\ & & & \ddots & & & \\ & & & & & & 0 \\ & & & -1 & 1 & -1 & 1 \\ 0 & \cdots & 0 & -1 & 1 & -1 & 1 \end{bmatrix}, & t = 2, \\ \frac{1}{4}\begin{bmatrix} 1 & -j & -1 & j & 0 & \cdots & 0 \\ 0 & -j & -1 & j & 1 & 0 & 0 \\ \vdots & \ddots & \ddots & \ddots & \ddots & \ddots & \vdots \\ & & & \ddots & & & \\ & & & & & & 0 \\ & & & j & 1 & -j & -1 \\ 0 & \cdots & 0 & j & 1 & -j & -1 \end{bmatrix}, & t = 3. \end{cases} \tag{3.49}$$

This method has low complexity, and the resulting channel estimates can also be more accurate than TD method. However, it is suitable for smaller delay spread channels model because it requires the channel to have a sufficiently wide coherence bandwidth. If the bandwidth is not wide enough, the estimation accuracy will suffer. We will present the simulation results in the next chapter.

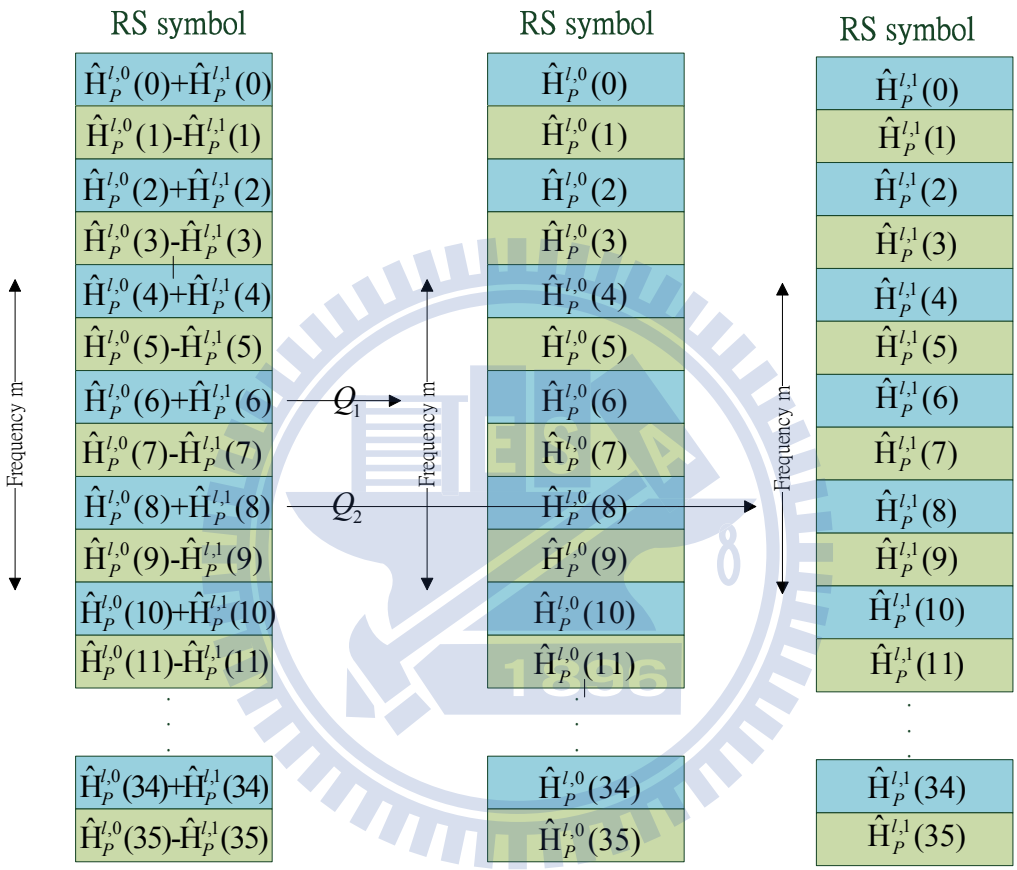

Figure 3.10: Frequency domain channel separation.

Chapter 4

Simulation Results and Analysis

In this chapter we discuss the simulation of the different channel estimation methods in frequency domain discussed previously for the LTE release 8 and LTE-A release 10 systems. We evaluate the performance of the methods mainly by observing the mean square error (MSE) and the symbol error rate (SER).

4.1 Simulation Conditions

This section introduces the system parameters and the channel models used in our simulation work. In chapter 2, we introduced the specification of the LTE release 8 and the LTE-A release 10 UL systems. The system parameters used in our simulation are listed in Table 4.1. We consider the following channel models: AWGN, single-path Rayleigh and SUI. The SUI models consist of 6 different radio channel models in three terrain categories [20, 21]. The three terrain types in suburban area are:

- A: hilly terrain, heavy tree,
- C: flat terrain, light tree, and
- B: between A and C.

Table 4.1: Simulated LTE UL System Parameters

Parameters	Values
Carrier frequency	2 GHz
CP type	Normal
Precoder DFT size	36
IFFT size	128
Allocated subcarriers	65–100
DC subcarriers	64
RS sequence	ZC
Modulation type	QPSK
Sampling time (T_s)	0.521 μs
Number of transmit antennas	1,2,4
Number of receiver antennas	1,2,4
Antenna correlation matrix 2×2	$\begin{bmatrix} 1 & 0.9 \\ 0.9 & 1 \end{bmatrix}$
Antenna correlation matrix 4×4	$\begin{bmatrix} 1 & 0.9^{1/9} & 0.9^{4/9} & 0.9^{9/9} \\ 0.9^{1/9} & 1 & 0.9^{1/9} & 0.9^{4/9} \\ 0.9^{4/9} & 0.9^{1/9} & 1 & 0.9^{1/9} \\ 0.9^{9/9} & 0.9^{4/9} & 0.9^{1/9} & 1 \end{bmatrix}$

Table 4.2: Channel Characteristics of SUI1 [20]

SUI – 1 Channel				
	Tap 1	**Tap 2**	**Tap 3**	**Units**
Delay	0	0.4	0.9	μs
Power (omni ant.)	0	-15	-20	dB
90% K-fact. (omni)	4	0	0	
75% K-fact. (omni)	20	0	0	
Power (30° ant.)	0	-21	-32	dB
90% K-fact. (30°)	16	0	0	
75% K-fact. (30°)	72	0	0	
Doppler	0.4	0.3	0.5	Hz
Antenna Correlation: $\rho_{ENV} = 0.7$ **Gain Reduction Factor:** GRF = 0 dB **Normalization Factor:** $F_{omni} = -0.1771$ dB, $F_{30°} = -0.0371$ dB			**Terrain Type:** C **Omni antenna:** $\tau_{RMS} = 0.111$ μs, overall K: K = 3.3 (90%); K = 10.4 (75%) **30° antenna:** $\tau_{RMS} = 0.042$ μs, overall K: K = 14.0 (90%); K = 44.2 (75%)	

The correspondence with the so-called SUI channels is as follows:

- C: SUI-1, SUI-2,
- B: SUI-3, SUI-4, and
- A: SUI-5, SUI-6.

In the above, SUI-1 and SUI-2 are Ricean multipath channels, whereas the other four are Rayleigh multipath channels. The Rayleigh channels are more hostile and exhibit a greater root-mean-square (RMS) delay spread. The SUI-2 represents a worst-case link for terrain type C. We employ the SUI models in our simulation, and here we only show the channel characteristics of SUI-1 to SUI-3 in Tables 4.2 to 4.4. The mean delay and RMS delay spread of each model are shown in Table 4.5.

4.2 Channel Estimation MSE of SISO Channels

As mentioned, we evaluate the performance of channel estimation methods in terms of the MSE and SER. Figure 4.1 illustrates the block diagram for the simulation.

Table 4.3: Channel Characteristics of SUI2 [20]

SUI – 2 Channel				
	Tap 1	**Tap 2**	**Tap 3**	**Units**
Delay	0	0.4	1.1	μs
Power (omni ant.)	0	-12	-15	dB
90% K-fact. (omni)	2	0	0	
75% K-fact. (omni)	11	0	0	
Power (30° ant.)	0	-18	-27	dB
90% K-fact. (30°)	8	0	0	
75% K-fact. (30°)	36	0	0	
Doppler	0.2	0.15	0.25	Hz
Antenna Correlation: $\rho_{ENV} = 0.5$ **Gain Reduction Factor:** GRF = 2 dB **Normalization Factor:** $F_{omni} = -0.3930$ dB, $F_{30°} = -0.0768$ dB			**Terrain Type:** C **Omni antenna:** $\tau_{RMS} = 0.202$ μs, overall K: K = 1.6 (90%); K = 5.1 (75%) **30° antenna:** $\tau_{RMS} = 0.069$ μs, overall K: K = 6.9 (90%); K = 21.8 (75%)	

Table 4.4: Channel Characteristics of SUI3 [20]

SUI – 3 Channel				
	Tap 1	**Tap 2**	**Tap 3**	**Units**
Delay	0	0.4	0.9	μs
Power (omni ant.)	0	-5	-10	dB
90% K-fact. (omni)	1	0	0	
75% K-fact. (omni)	7	0	0	
Power (30° ant.)	0	-11	-22	dB
90% K-fact. (30°)	3	0	0	
75% K-fact. (30°)	19	0	0	
Doppler	0.4	0.3	0.5	Hz
Antenna Correlation: $\rho_{ENV} = 0.4$ **Gain Reduction Factor:** GRF = 3 dB **Normalization Factor:** $F_{omni} = -1.5113$ dB, $F_{30°} = -0.3573$ dB			**Terrain Type:** B **Omni antenna:** $\tau_{RMS} = 0.264$ μs, overall K: K = 0.5 (90%); K = 1.6 (75%) **30° antenna:** $\tau_{RMS} = 0.123$ μs, overall K: K = 2.2 (90%); K = 7.0 (75%)	

Table 4.5: Mean Delay and RMS Delay Spread of Each SUI Channel Model

Channel type	Path delay (μs)	Path power (dB)	Mean delay (μs)	RMS delay spread (μs)
SUI1	0, 0.4, 0.9	0, -15, -20	0.0208	0.1105
SUI2	0, 0.4, 1.1	0, -12, -15	0.0548	0.2029
SUI3	0, 0.4, 0.9	0, -5, -10	0.1529	0.2637
SUI4	0, 1.5, 4	0, -4, -8	0.7909	1.2566
SUI5	0, 4, 10	0, -5, -10	1.5993	2.8418
SUI6	0, 14, 20	0, -10, -14	1.9268	5.2397

In our simulation, all the figures are the average result over 200 frames. We consider PUSCH only. In the 200 frames, there are 4000 RS symbol and 864000 data signal points excluding RS.

First, we consider the AWGN channel. Even though we usually do not encounter AWGN channels in wireless communication, it is a channel condition that facilitates easy theoretical analysis. Hence we may use it to examine the performance of channel estimation methods and to verify the correctness of simulation programs. Figure 4.2 illustrate a simple model concerning how the channel response evolves between two successive symbols. The theoretical MSE for linear TD interpolation over the data symbols in AWGN can be found as [22]:

$$\begin{aligned} MSE &= \frac{1}{6}E[|\sum_{k=1}^{6} h_k - \hat{h_k}|^2] \\ &= \frac{1}{6}E[\sum_{k=1}^{6} |\{h_k - [h_{RS0} + \frac{k}{7}(h_{RS1} - h_{RS0})]\}|^2] \\ &= \frac{1}{6}E[\sum_{k=1}^{6} |\{(\frac{k}{7})^2 + (\frac{7-k}{7})^2\}\sigma_W^2] \\ &= \frac{13}{21}\sigma_W^2. \end{aligned} \tag{4.1}$$

Figure 4.3 shows LS, LS + FD LMMSE and LS + FD GWD simulation results for MSE,

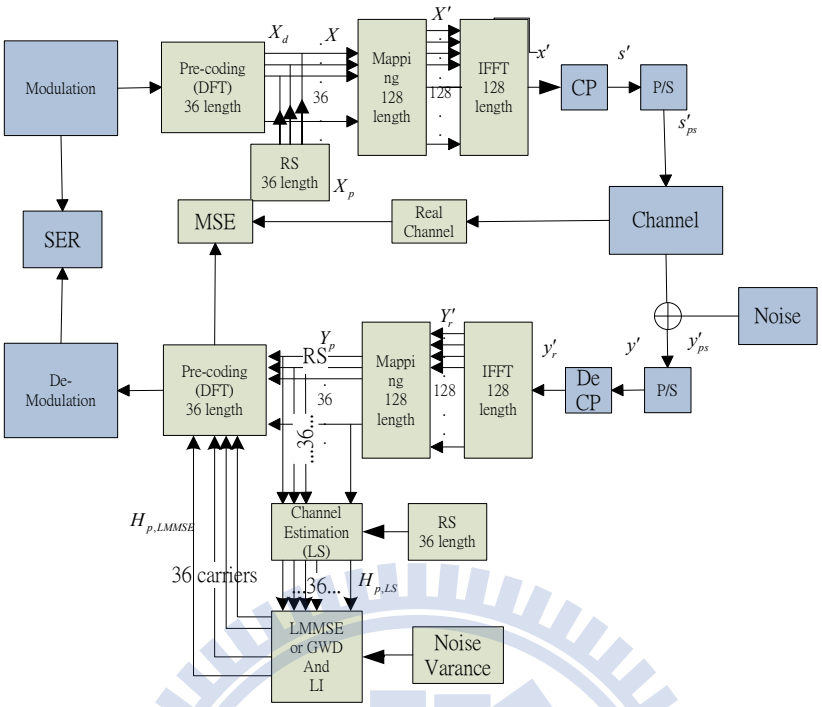

Figure 4.1: Block diagram for MSE and SER simulation.

along with the theoretical values for LS, all with linear TD interpolation. We will use LS, LMMSE and GWD to denote LS, LS + FD LMMSE and LS + FD GWD below in this chapter, all with do linear TD interpolation. We note that, in this case, FD LMMSE can reduce noise. The reduction has to do with the size of the autocorrelation submatrix used (see corresponding discussion in section 3.2.2). For example, the MSE of FD LMMSE in using 12×12 submatrices of R'_C such as in Figure 3.3 left, the LMMSE matrix is expressed

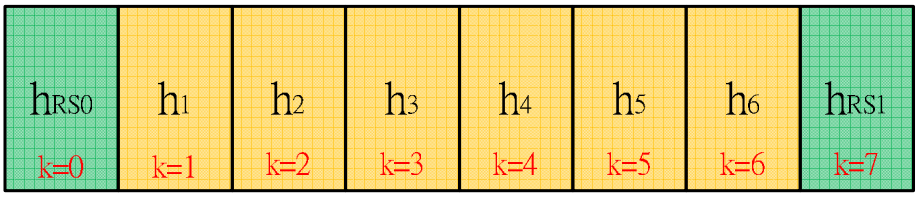

Figure 4.2: A simple model for the the evolution of channel response between two successive RS symbol in PUSCH [22, Fig. 4.3].

as:

$$R'_C \cdot (R'_C + \sigma_W^2 I_k)^{-1} = \begin{bmatrix} 1 & 1 & \cdots & 1 \\ 1 & 1 & & \\ \vdots & & \ddots & \vdots \\ 1 & \cdots & & 1 \end{bmatrix} \cdot \begin{bmatrix} 1+\sigma_W^2 & 1 & \cdots & 1 \\ 1 & 1+\sigma_W^2 & & \\ \vdots & & \ddots & \vdots \\ 1 & & \cdots & 1+\sigma_W^2 \end{bmatrix}^{-1}$$
$$= \begin{bmatrix} (S_L+\sigma_W^2)^{-1} & (S_L+\sigma_W^2)^{-1} & \cdots & (S_L+\sigma_W^2)^{-1} \\ (S_L+\sigma_W^2)^{-1} & (S_L+\sigma_W^2)^{-1} & & \\ \vdots & & \ddots & \vdots \\ (S_L+\sigma_W^2)^{-1} & & \cdots & (S_L+\sigma_W^2), \end{bmatrix} \quad (4.2)$$

so

$$E(\left|\hat{H}_{P,LMMSE} - H_P\right|^2) = \frac{\sigma_W^2}{S_L + \sigma_W^2}. \quad (4.3)$$

the MSE should be reduced by approximately S_L times compared to LS as

$$MSE_{LMMSE} = \frac{13}{21}\sigma_W^2 \frac{1}{S_L + \sigma_W^2}, \quad (4.4)$$

where S_L is size of the R'_c submatrix. The FD GWD which uses a Gaussian sequence of length $S_G = 12$ has a similar performance as FD LMMSE in low SNR, but its MSE cannot be reduced in high SNR due to the bandwidth of Gaussian distribution is narrower in high SNR. We will discuss other values of S_L and S_G later.

Next, we consider single-path Rayleigh fading channel. According to [22] we can understand the theoretical MSE performance floor of LS, after linear TD interpolation, will be proportional to the fourth power of the speed in high SNR. It was found to be the case in

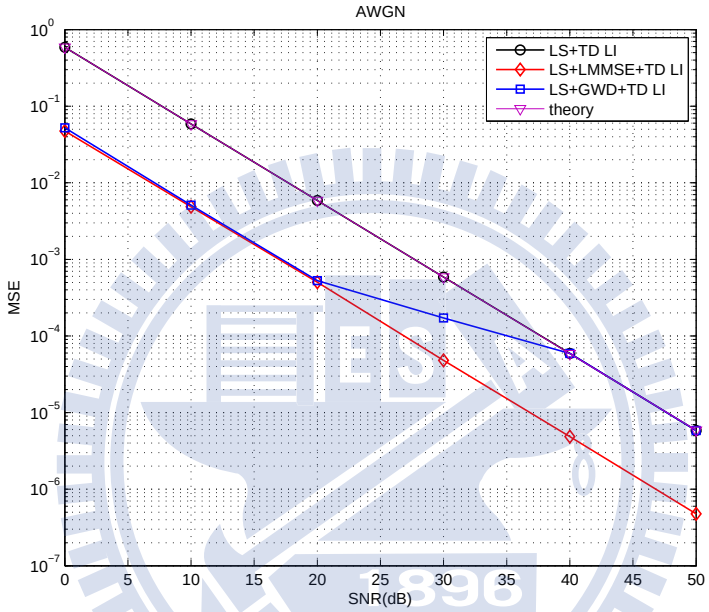

Figure 4.3: MSE performance of linear LS, LS + LMMSE and LS + GWD (all with linear TD interpolation) in AWGN channel, compared with theory for LS + linear TD interpolation where LMMSE uses 12×12 submatrix of R'_C and GWD uses length 12 Gaussian sequence.

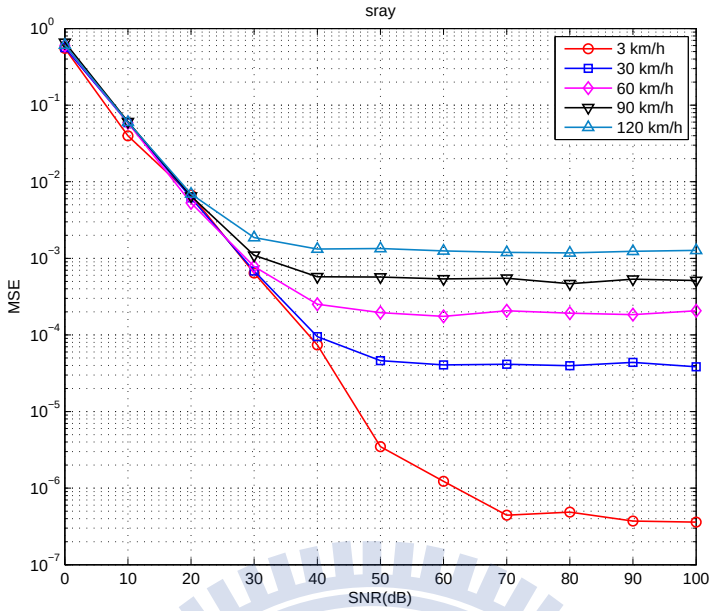

Figure 4.4: MSE performance for LS + linear TD interpolation under all-one RS in single-path Rayleigh channel.

simulation with all-one RS sequences and all-one test transmit data, as shown in Figure 4.4. But under ZC RS the MSE performance was found to be proportional to the third power of the speed, as shown in Figure 4.5. The reason for this situation still awaits a satisfactory explanation.

Figure 4.6 shows the results for single-path Rayleigh fading channel with FD LMMSE and FD GWD. Similar to AWGN, the FD LMMSE performance is inversely proportional to the size of R'_C submatrix and FD GWD performance depends on the window length. However, in high SNR the noise variance σ_W^2 will become smaller. Under the AWGN channel auto-correlation R'_C is a all-ones matrix, the mathematical derivation of LMMSE matrix is written in (4.2). We can note that when under larger delay channel, R'_C is not all-ones matrix, the gain of LMMSE is not $(S_L + \sigma_W^2)^{-1}$. Because correlation of channel become lower, the influence of S_L also become smaller In high SNR situation FD LMMSE is similar to only

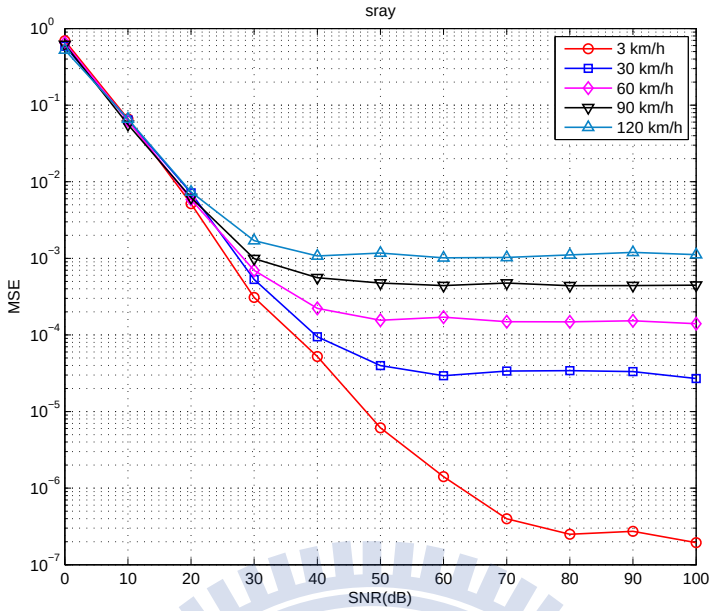

Figure 4.5: MSE performance for LS + linear TD interpolation under ZC RS in single-path Rayleigh channel.

doing LS due to the inter-carrier interference (ICI) still exist.

Gaussian distribution of variance in FD GWD is based on the noise energy. The greater the SNR, the smaller the Gaussian distribution of variance will be. That is, the width of the distribution will be narrower and the affect of FD GWD will also be smaller. The design of FD GWD is in order to reduce the complexity of the FD LMMSE and improve performance of CWD in [10]. However, we can not solve the real noise problem, just only ignore the impact of noise in high SNR.

Now consider multipath fading channels SUI1, SUI2 and SUI3. We display the simulation results in Figures 4.7, 4.8 and 4.9. They show the channel estimation performance of the three methods at the speeds of 3, 60, and 120 km/h. We see that, in high SNR the three methods exhibit a similar performance floor. In low SNR the MSE performance of both LMMSE and GWD are good.

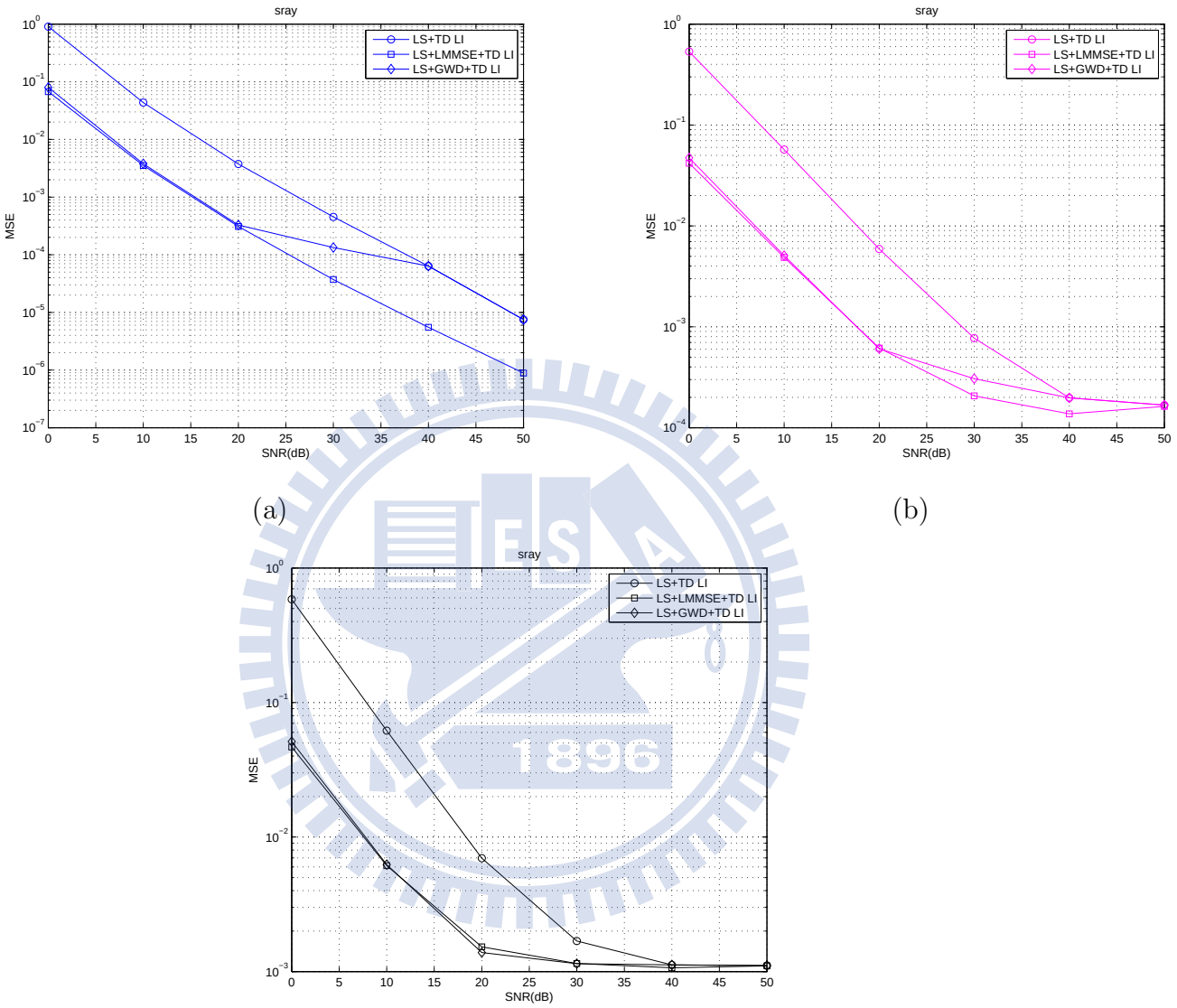

Figure 4.6: MSE performance of different channel estimation methods with $S_L = 12, S_G = 12$ in single-path Rayleigh fading channel at speeds (a) 3 km/h, (b) 60 km/h, and (c) 120 km/h.

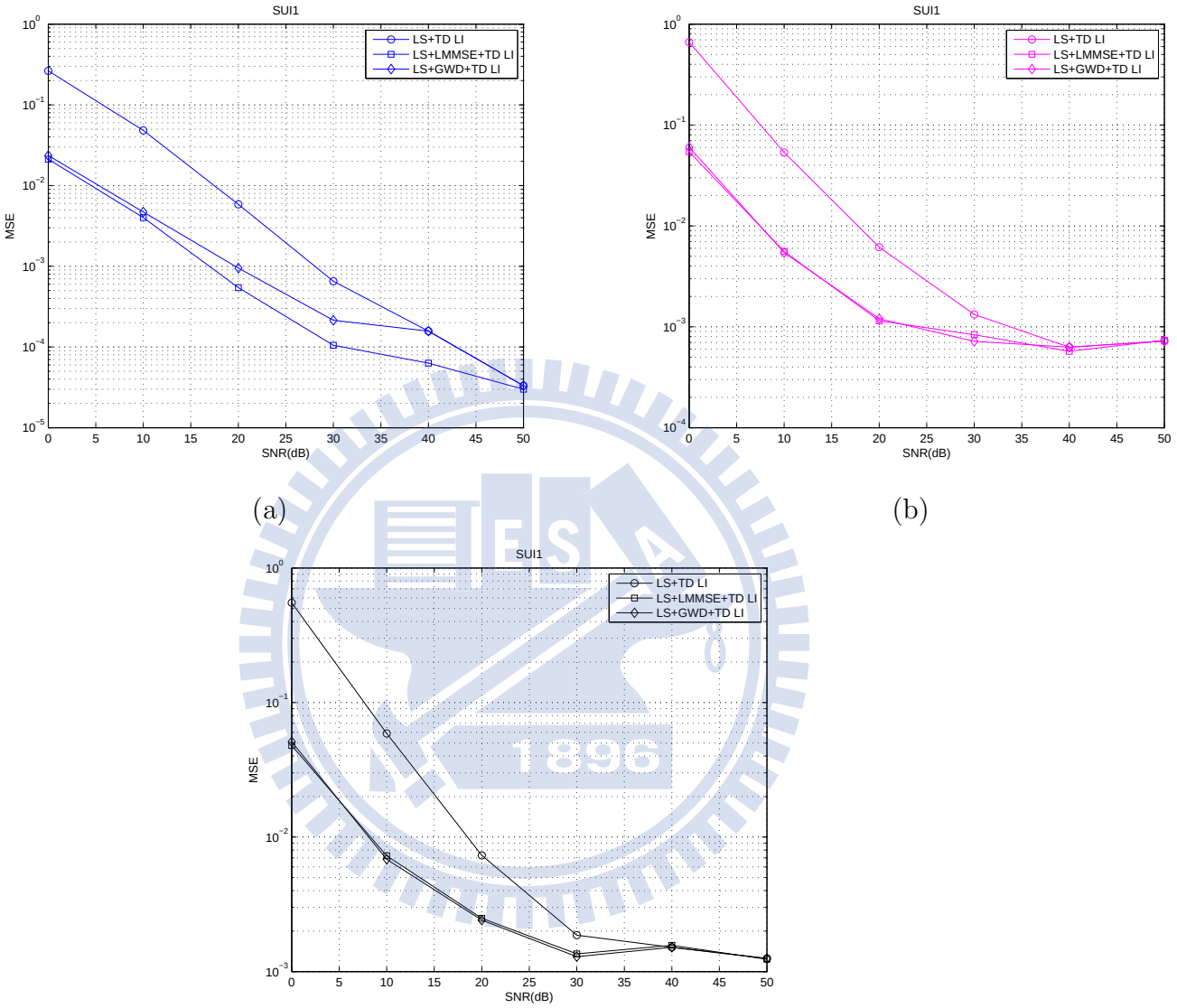

Figure 4.7: MSE performance of different channel estimation methods with $S_L = 12, S_G = 12$ in SUI1 fading channel at speeds (a) 3 km/h, (b) 60 km/h, and (c) 120 km/h.

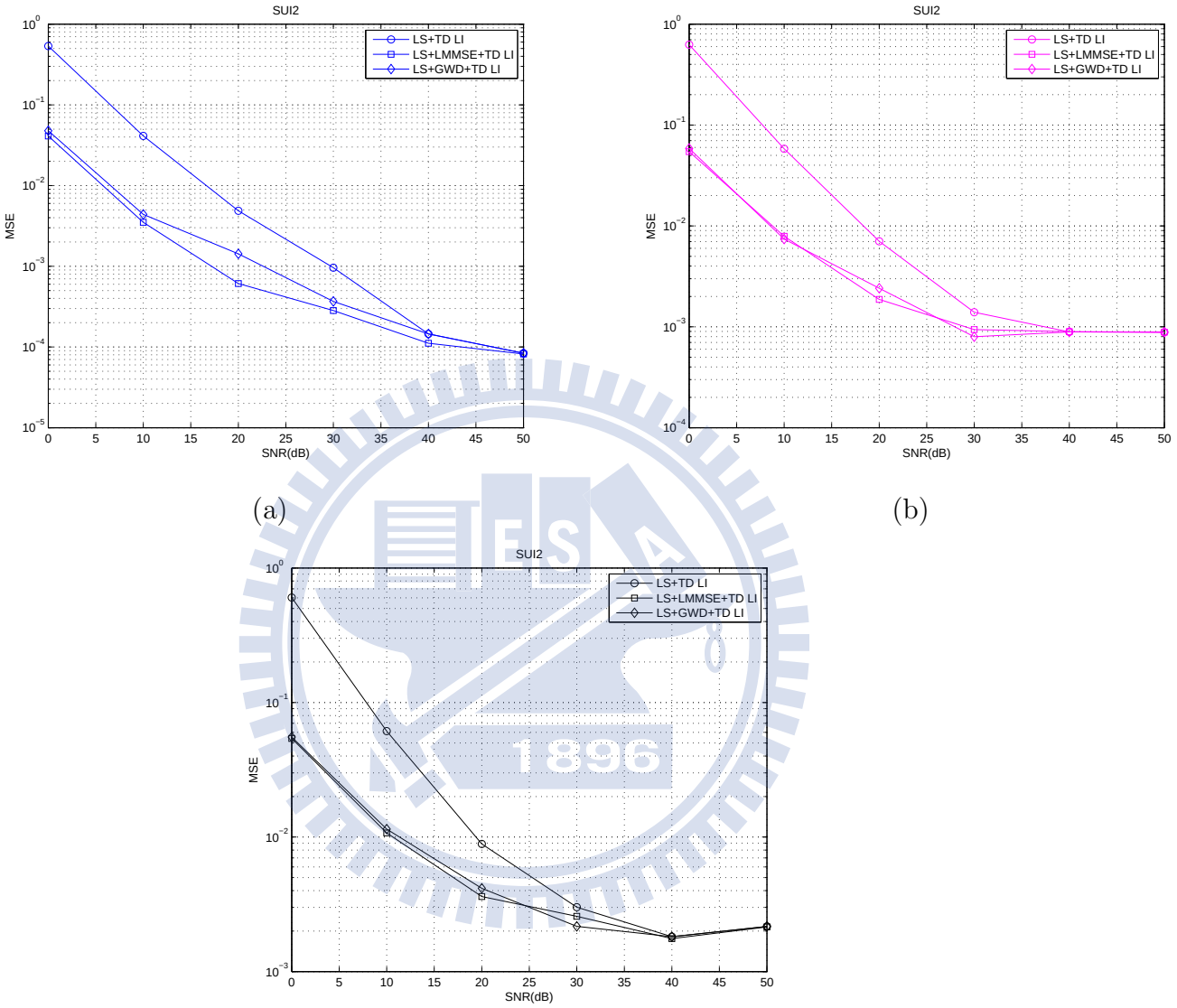

Figure 4.8: MSE performance of different channel estimation methods with $S_L = 12, S_G = 12$ in SUI2 fading channel at speeds (a) 3 km/h, (b) 60 km/h, and (c) 120 km/h.

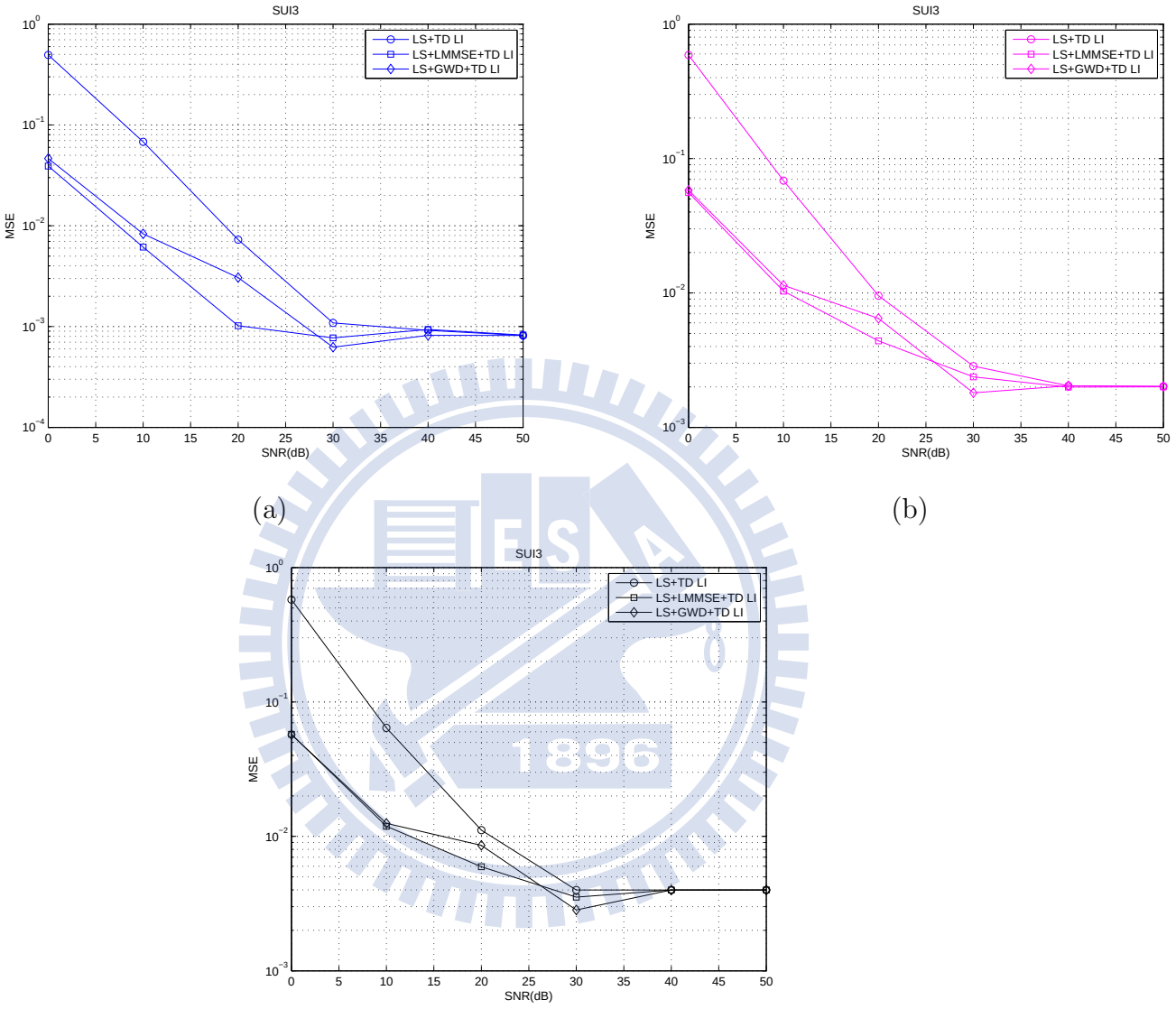

Figure 4.9: MSE performance of different channel estimation methods with $S_L = 12, S_G = 12$ in SUI3 fading channel at speeds (a) 3 km/h, (b) 60 km/h, and (c) 120 km/h.

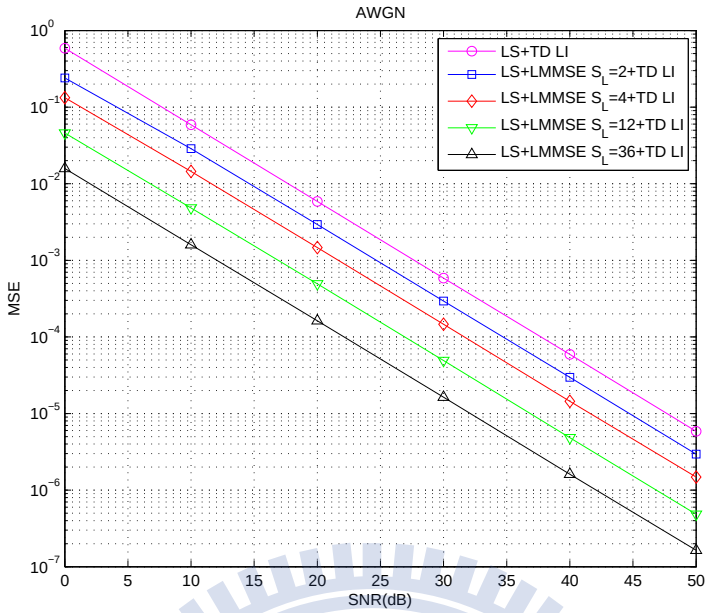

Figure 4.10: MSE performance of FD LMMSE at different autocorrelation submatrix sizes S_L in AWGN channel.

Next, consider the effect of the size of the autocorrelation matrix R'_C's submatrix, S_L, on the performance of the LMMSE method. Figure 4.10 shows the effect of different submatrix sizes in AWGN channel. We can clearly see that the MSE is inversely related to the submatrix size. However, in fading channels, because the performance high SNR is affected by channel time-variation, there is an error floor. Regardless of the size of the matrix, the MSE performance will all converge to the error floor value in high SNR. In low SNR, it will be affected by the coherence bandwidth, and the MSE performance will not be completely inversely proportional to the autocorrelation matrix size. We have the results as shown in Figure 4.11–4.14 for various channel conditions.

FD GWD shows somewhat similar performance characteristics as FD LMMSE. In AWGN channel the Gaussian distribution has narrower bandwidths in higher SNR values. So the MSE performance with FD GWD in high SNR similar to LS. But the performance improves

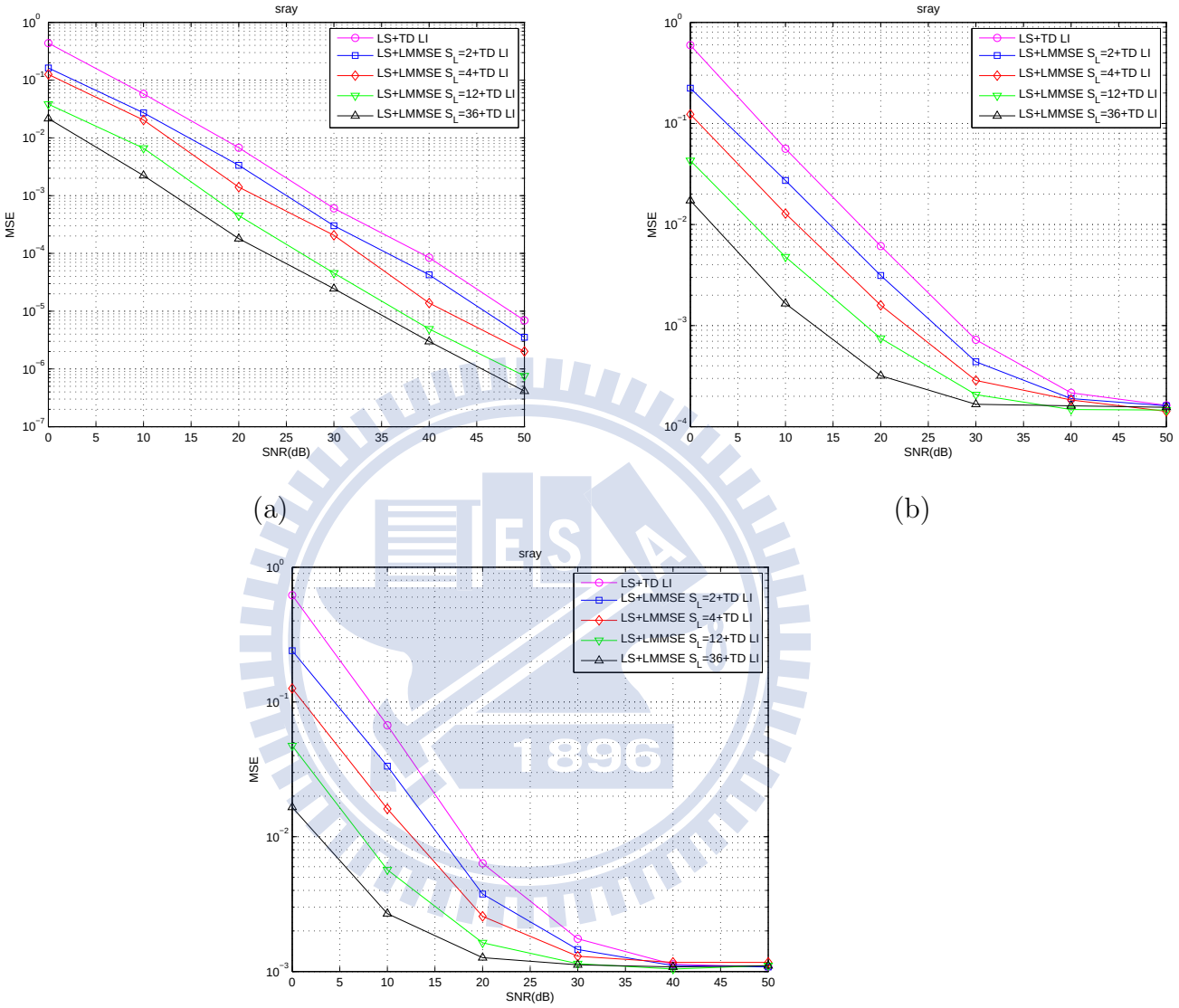

Figure 4.11: MSE performance at different FD LMMSE submatrix sizes S_L in single-path Rayleigh fading channel at speeds (a) 3 km/h, (b) 60 km/h, and (c) 120 km/h.

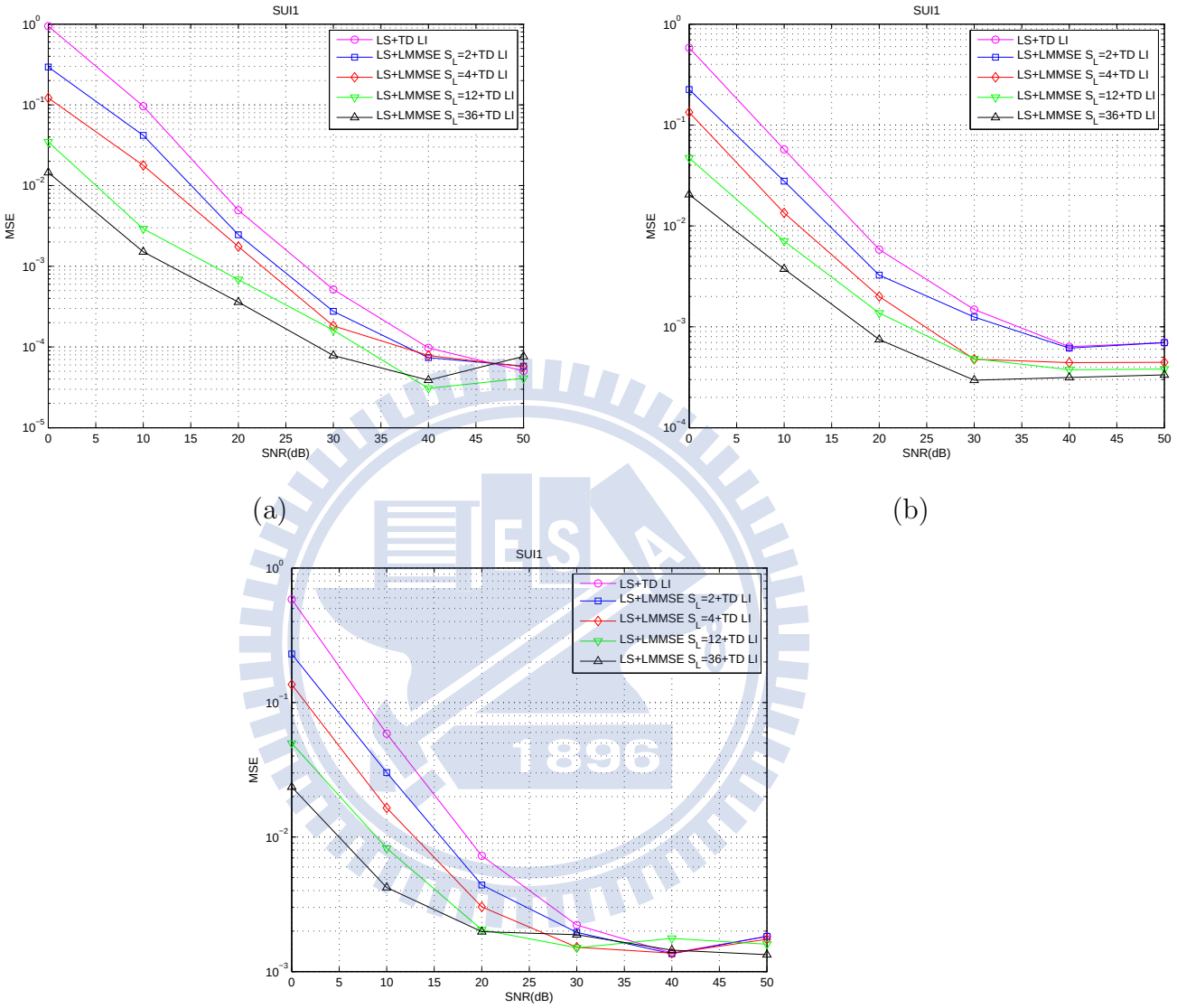

Figure 4.12: MSE performance at different FD LMMSE submatrix sizes S_L in SUI1 fading channel at speeds (a) 3 km/h, (b) 60 km/h, and (c) 120 km/h.

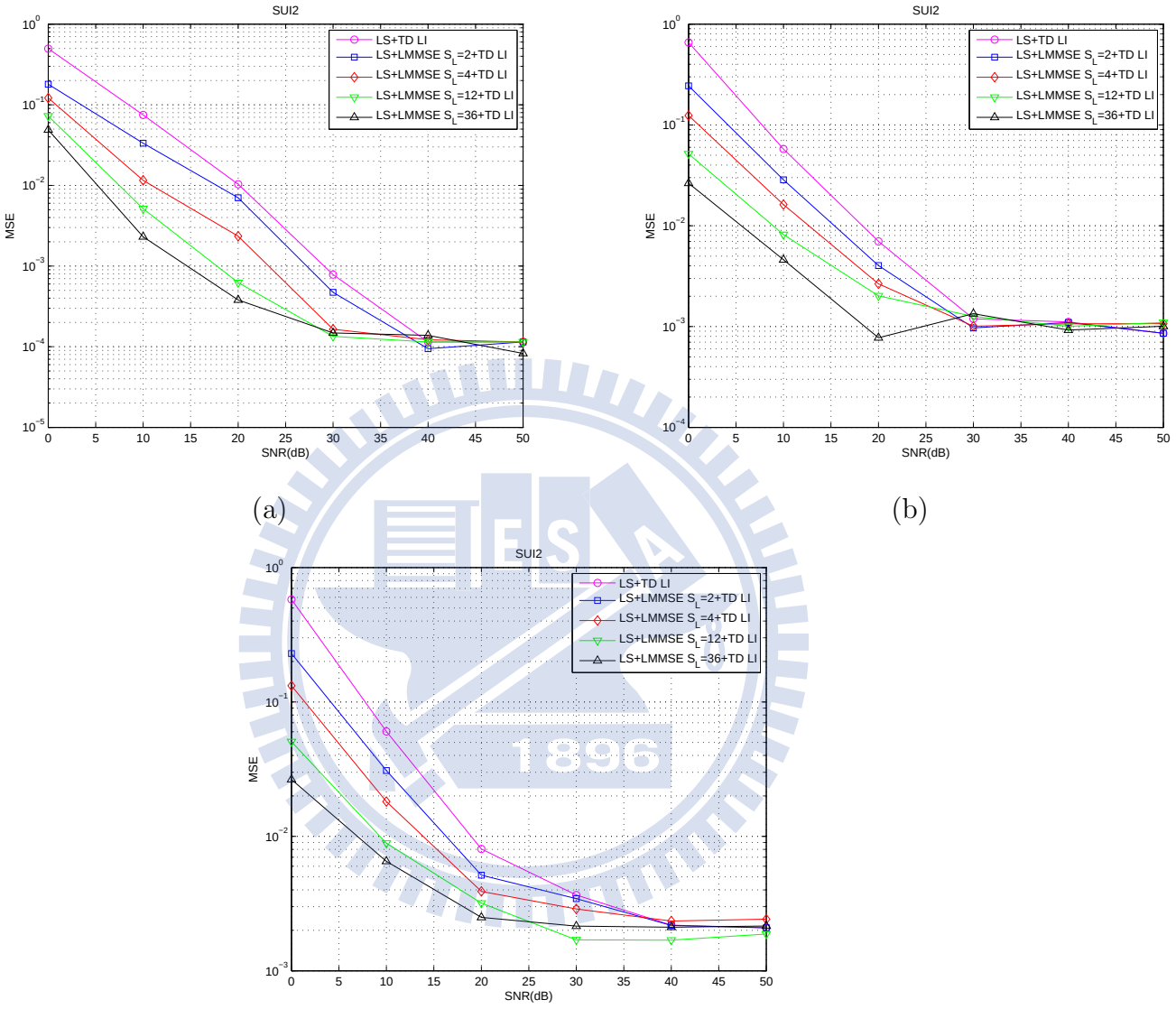

Figure 4.13: MSE performance at different FD LMMSE submatrix sizes S_L in SUI2 fading channel at speeds (a) 3 km/h, (b) 60 km/h, and (c) 120 km/h.

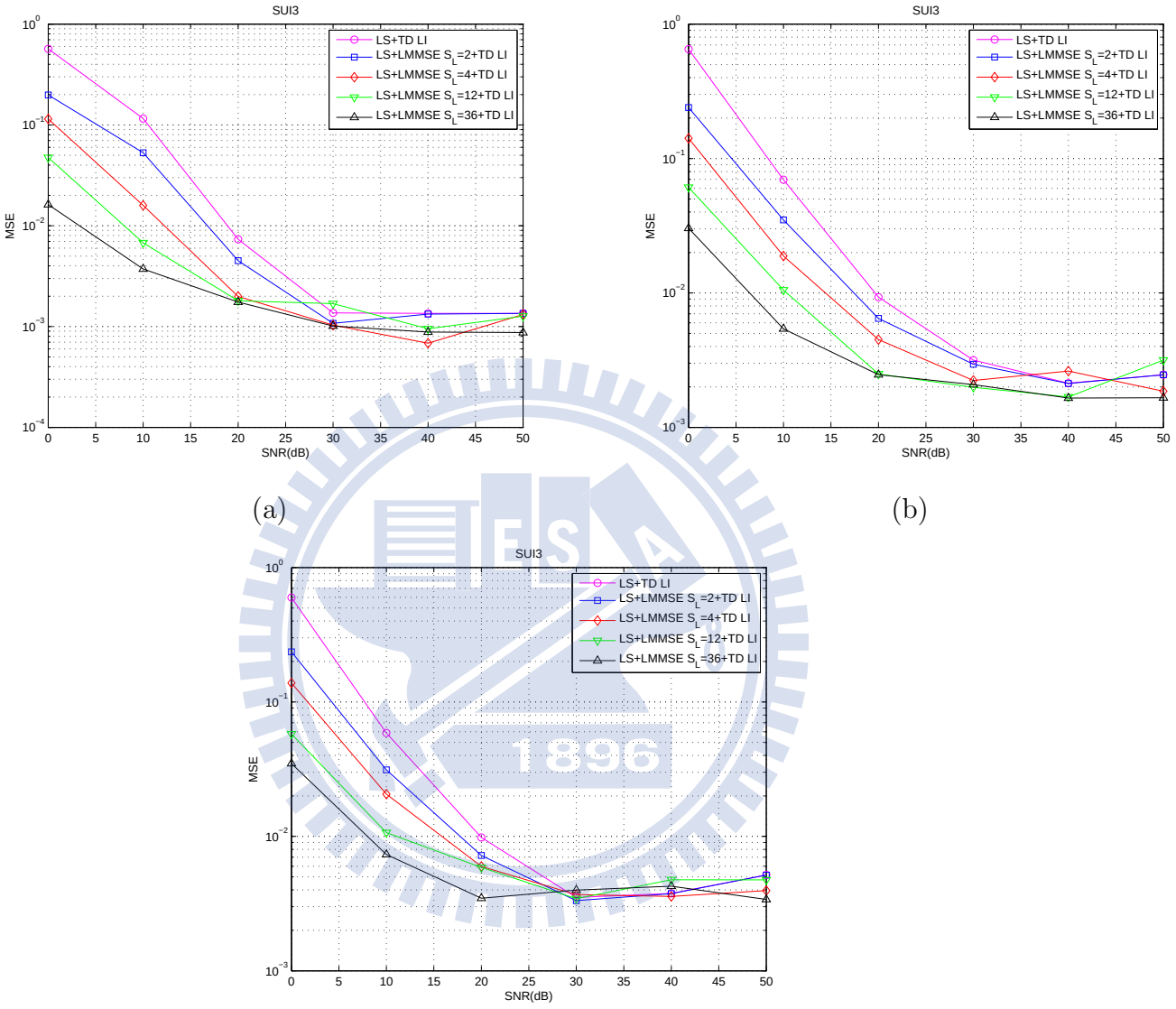

Figure 4.14: MSE performance at different FD LMMSE submatrix sizes S_L in SUI3 fading channel at speeds (a) 3 km/h, (b) 60 km/h, and (c) 120 km/h.

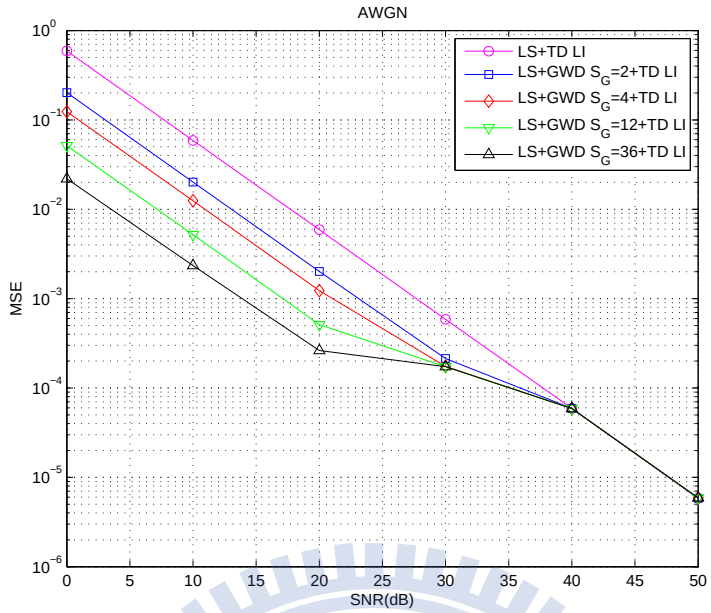

Figure 4.15: MSE performance at different FD GWD bandwidth S_G in AWGN channel.

relative to LS estimation in low SNR due to a wider Gaussian distribution bandwidth, as shown in Figure 4.15. Figures 4.16–4.19 show results for fading channel. Similar observations as the above bold.

Next we consider the different ways of approximating the autocorrelation matrix R'_C in FD LMMSE. The previous chapter referred to the use of the R'_C sub-matrix to reduce the amount of computation such as Figure 3.3, and then using overlapping method to compensate for the deficiencies in the sub-matrix connection. The data of the simulation is displayed in Figures4.20–4.23. We can see that there is actually not much difference in MSE performance for autocorrelation matrix that is overlapped and autocorrelation matrix that is not overlapped. In fact we think the performance of overlap is better, but the simulation is not what we want.We will discuss this phenomenon in the future work

There was another method in the previous chapter and that is SVD. It not only can solve

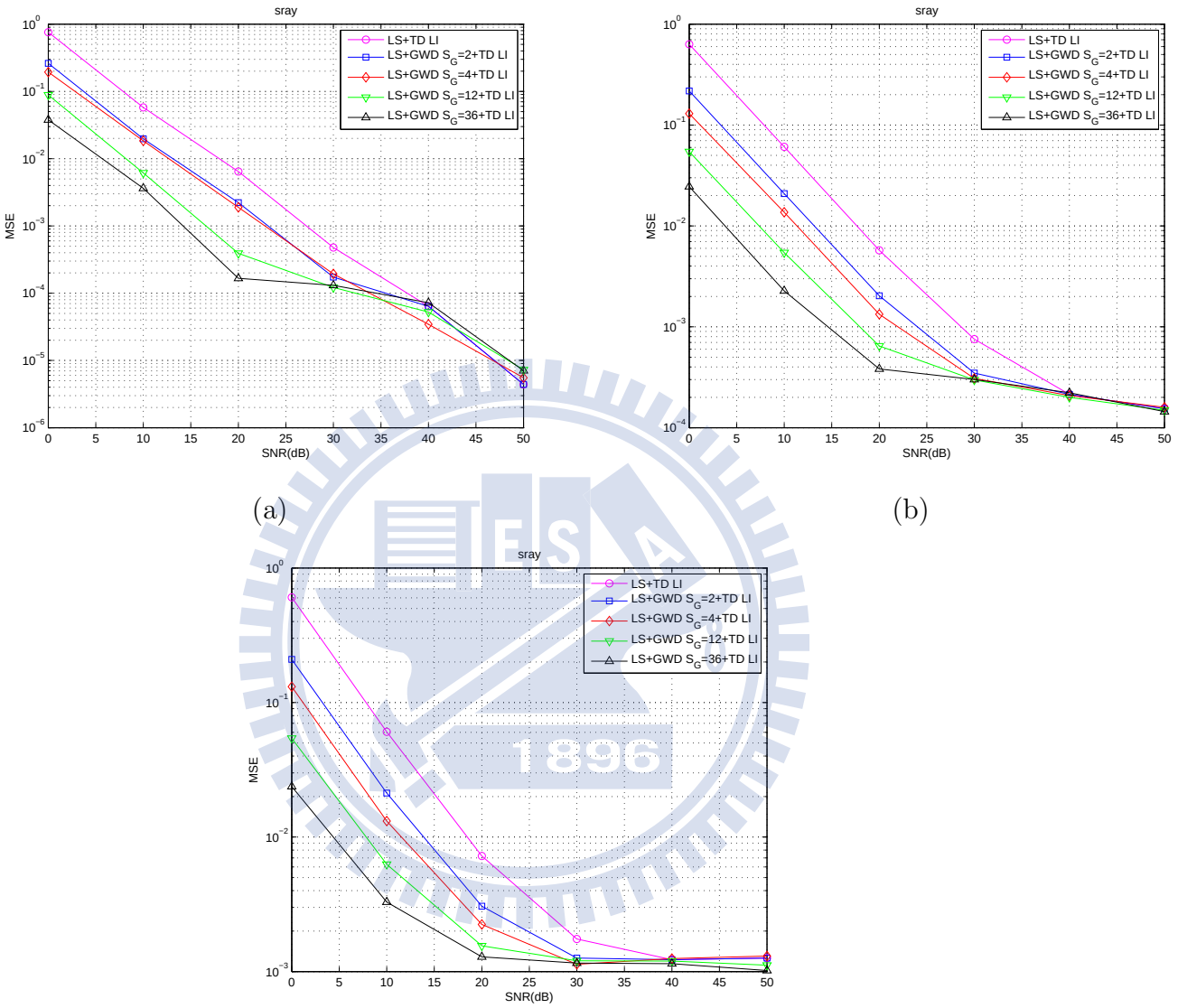

Figure 4.16: MSE performance at different FD GWD bandwidth S_G in single-path Rayleigh fading channel at speeds (a) 3 km/h, (b) 60 km/h, and (c) 120 km/h.

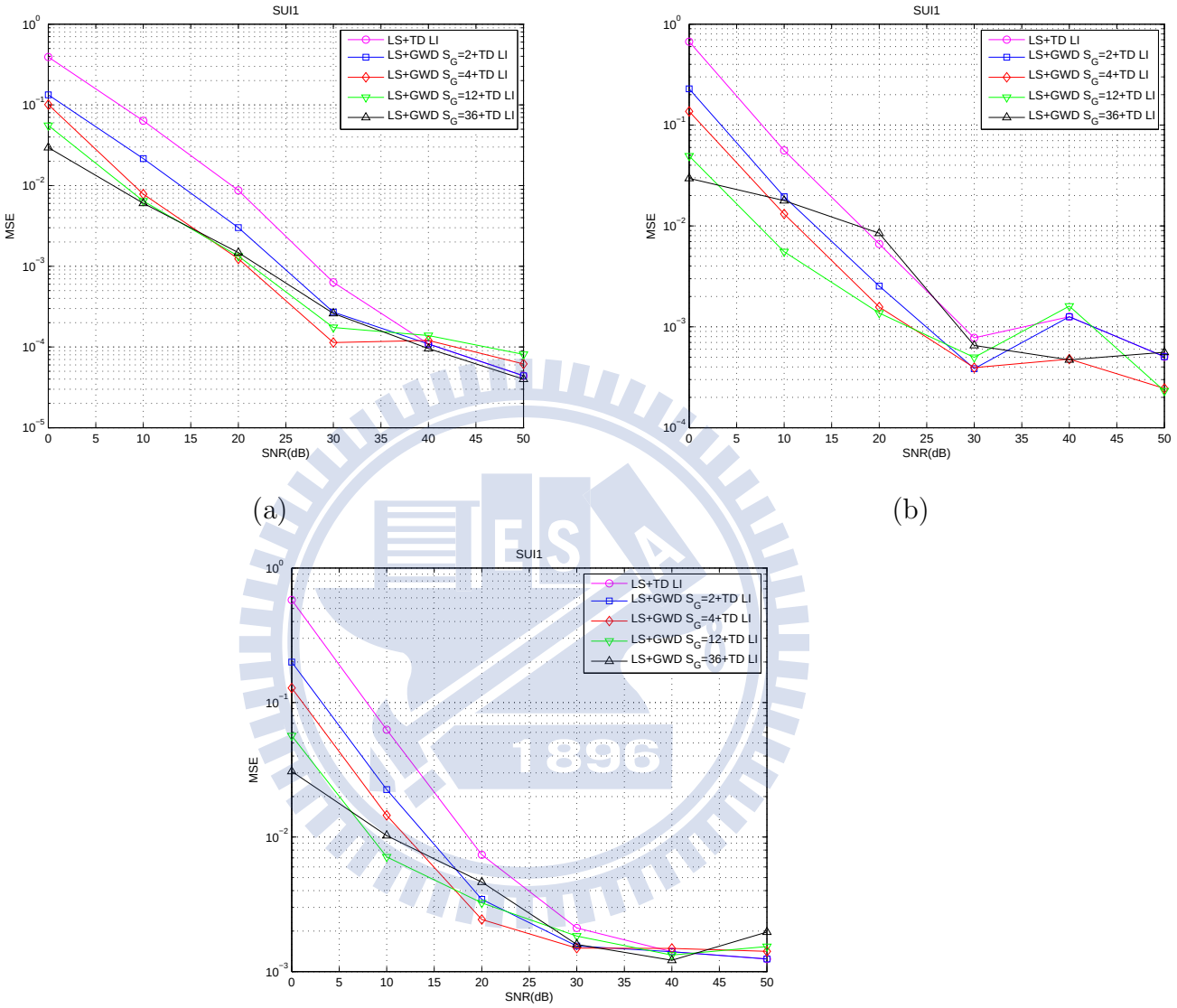

Figure 4.17: MSE performance at different FD GWD bandwidth S_G in SUI1 fading channel at speeds (a) 3 km/h, (b) 60 km/h, and (c) 120 km/h.

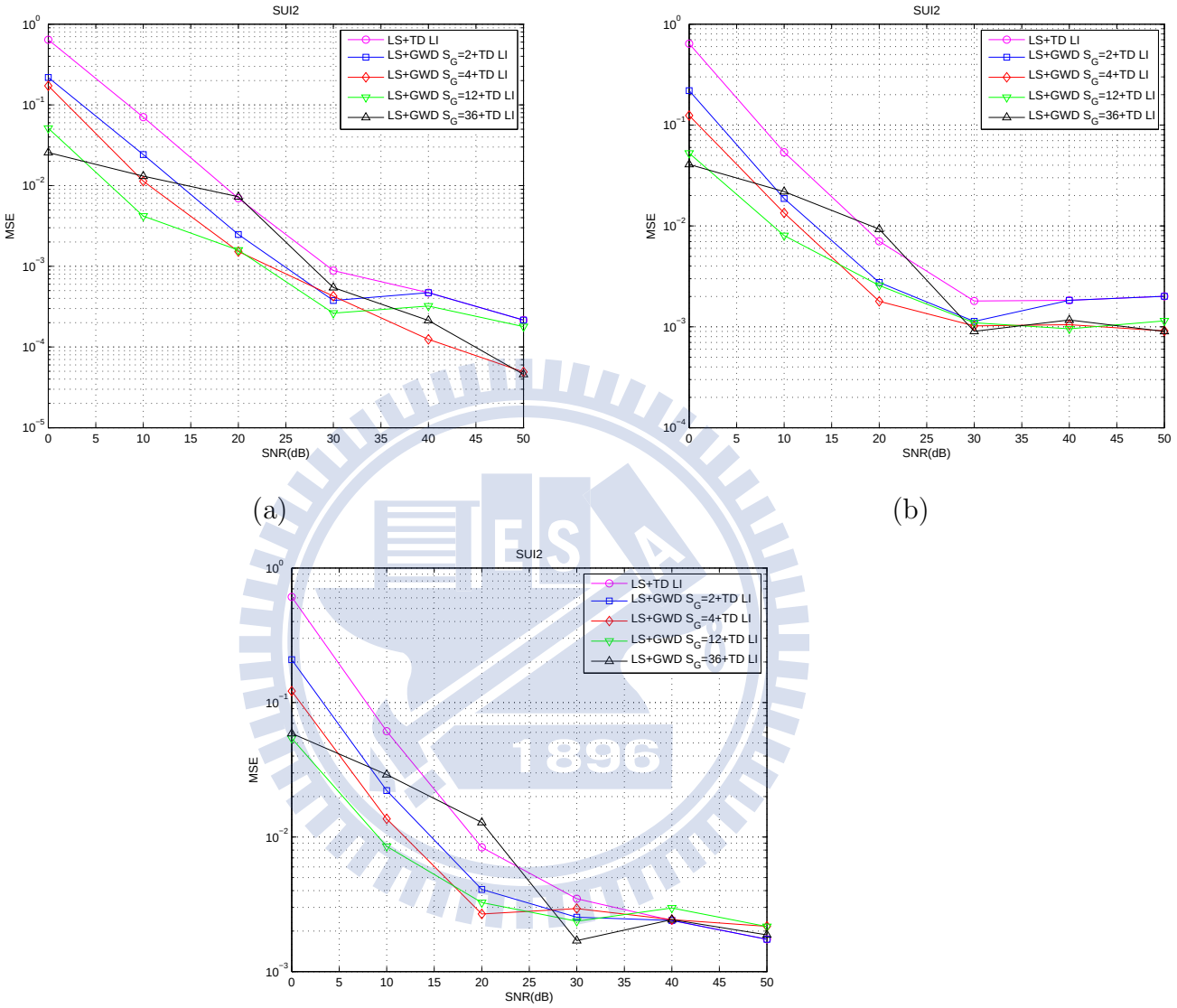

Figure 4.18: MSE performance at different FD GWD bandwidth S_G in SUI2 fading channel at speeds (a) 3 km/h, (b) 60 km/h, and (c) 120 km/h.

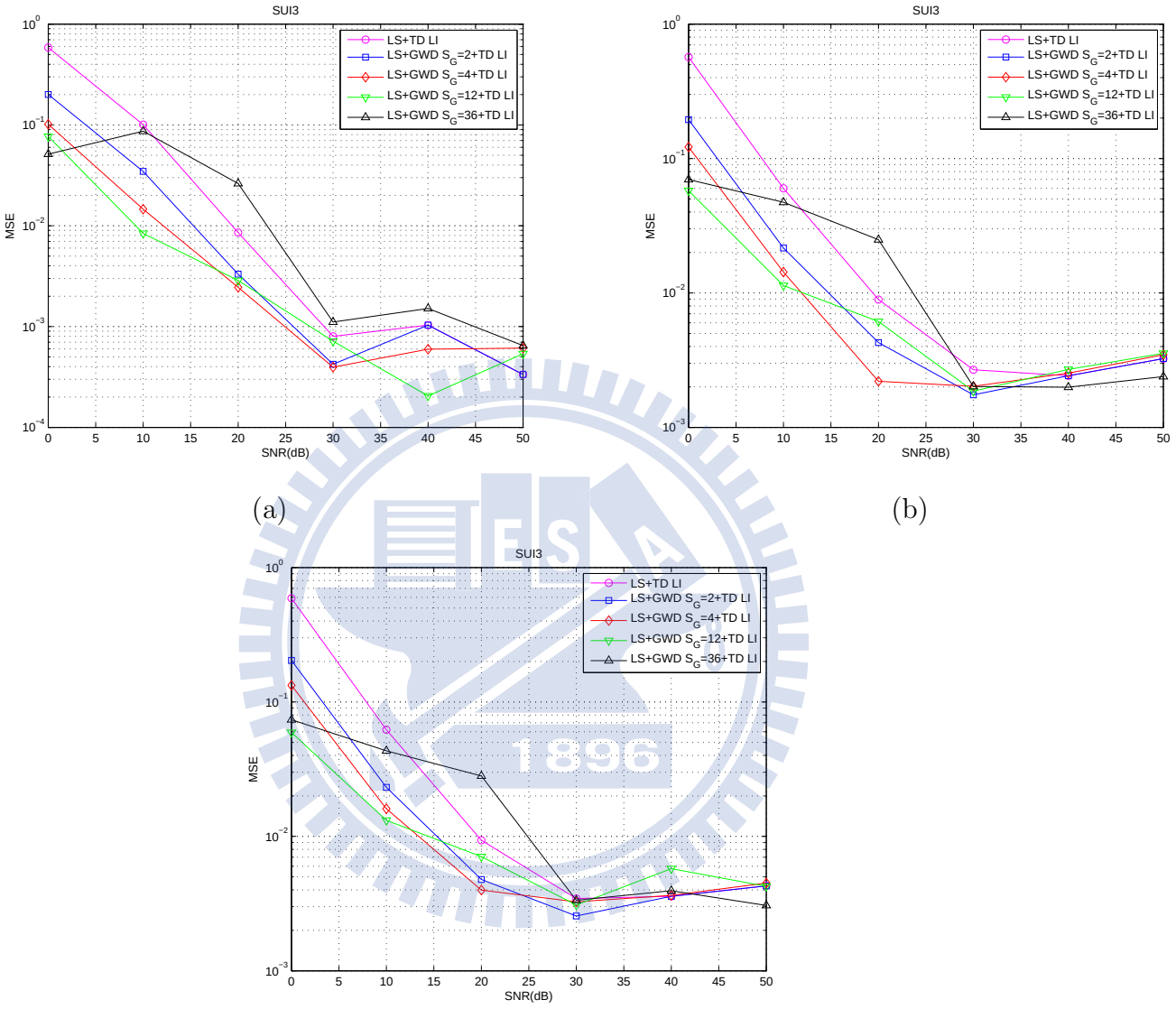

Figure 4.19: MSE performance at different FD GWD bandwidth S_G in SUI3 fading channel at speeds (a) 3 km/h, (b) 60 km/h, and (c) 120 km/h.

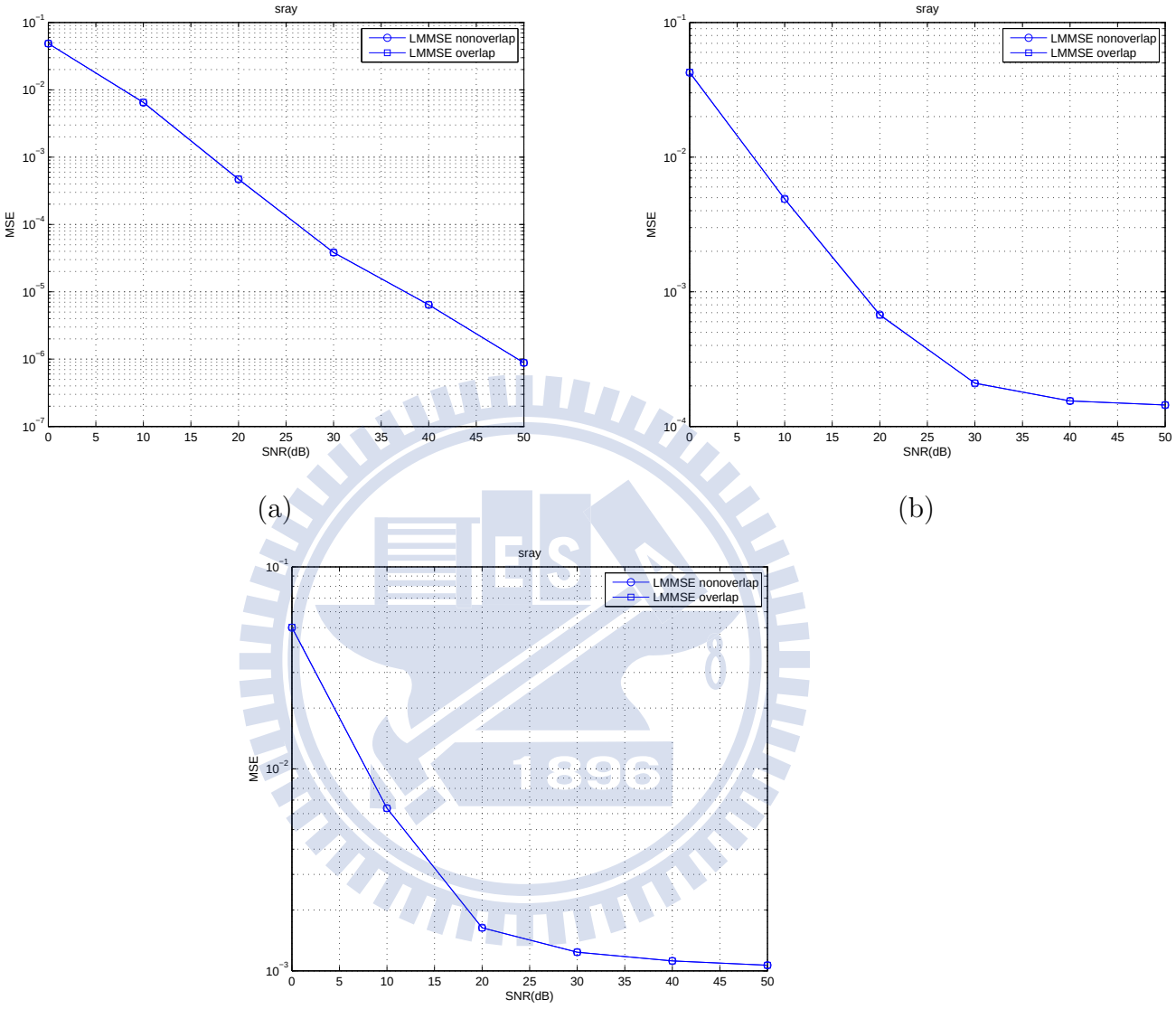

Figure 4.20: MSE performance for FD LMMSE with overlapped and non-overlapped R'_C window and submatrix size is $S_L = 12$ in single-path Rayleigh fading channel at speeds: (a) 3 km/h, (b) 60 km/h, and (c) 120 km/h.

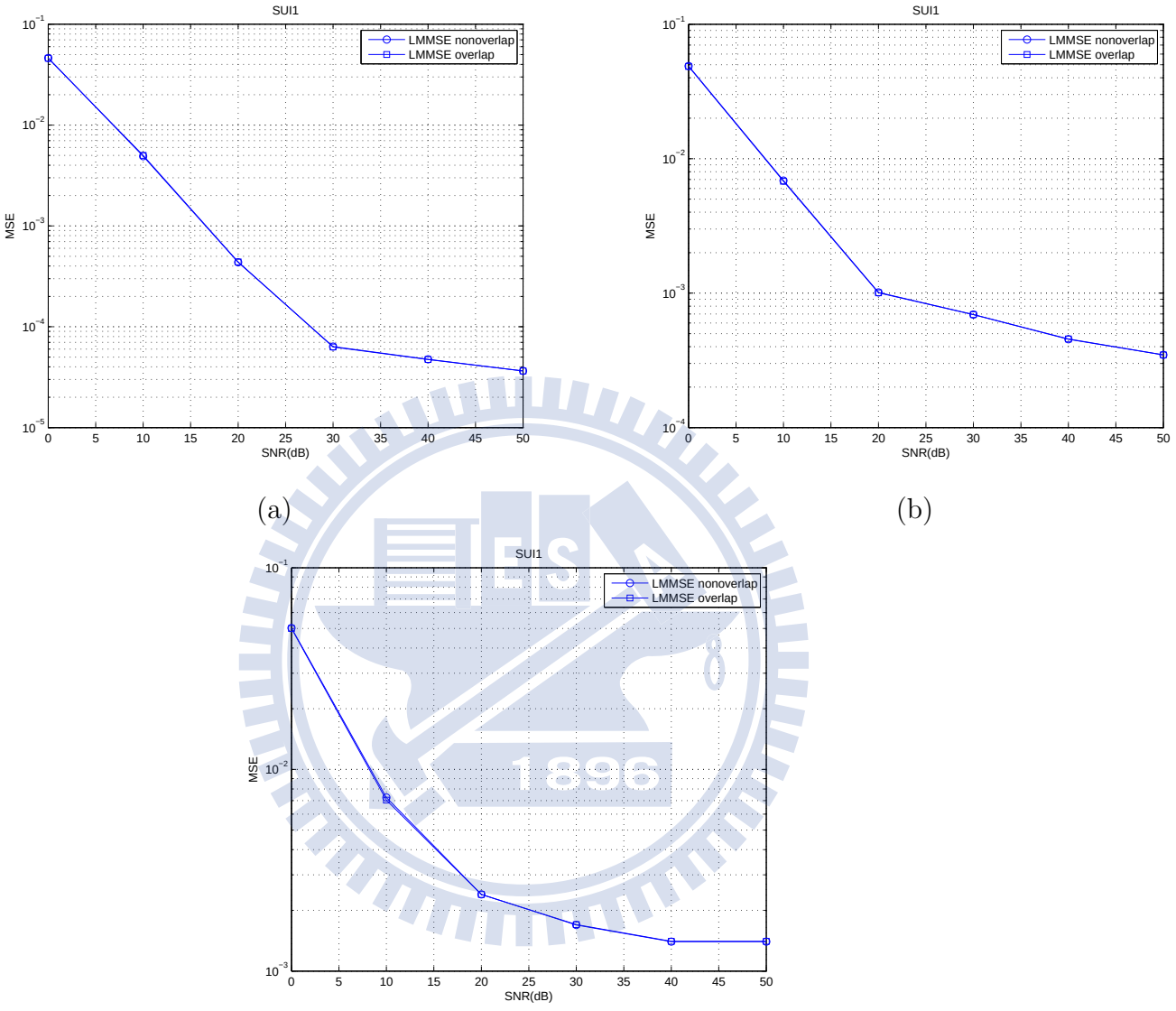

Figure 4.21: MSE performance for FD LMMSE with overlapped and non-overlapped R'_C window and submatrix size is $S_L = 12$ in SUI1 fading channel at speeds: (a) 3 km/h, (b) 60 km/h, and (c) 120 km/h.

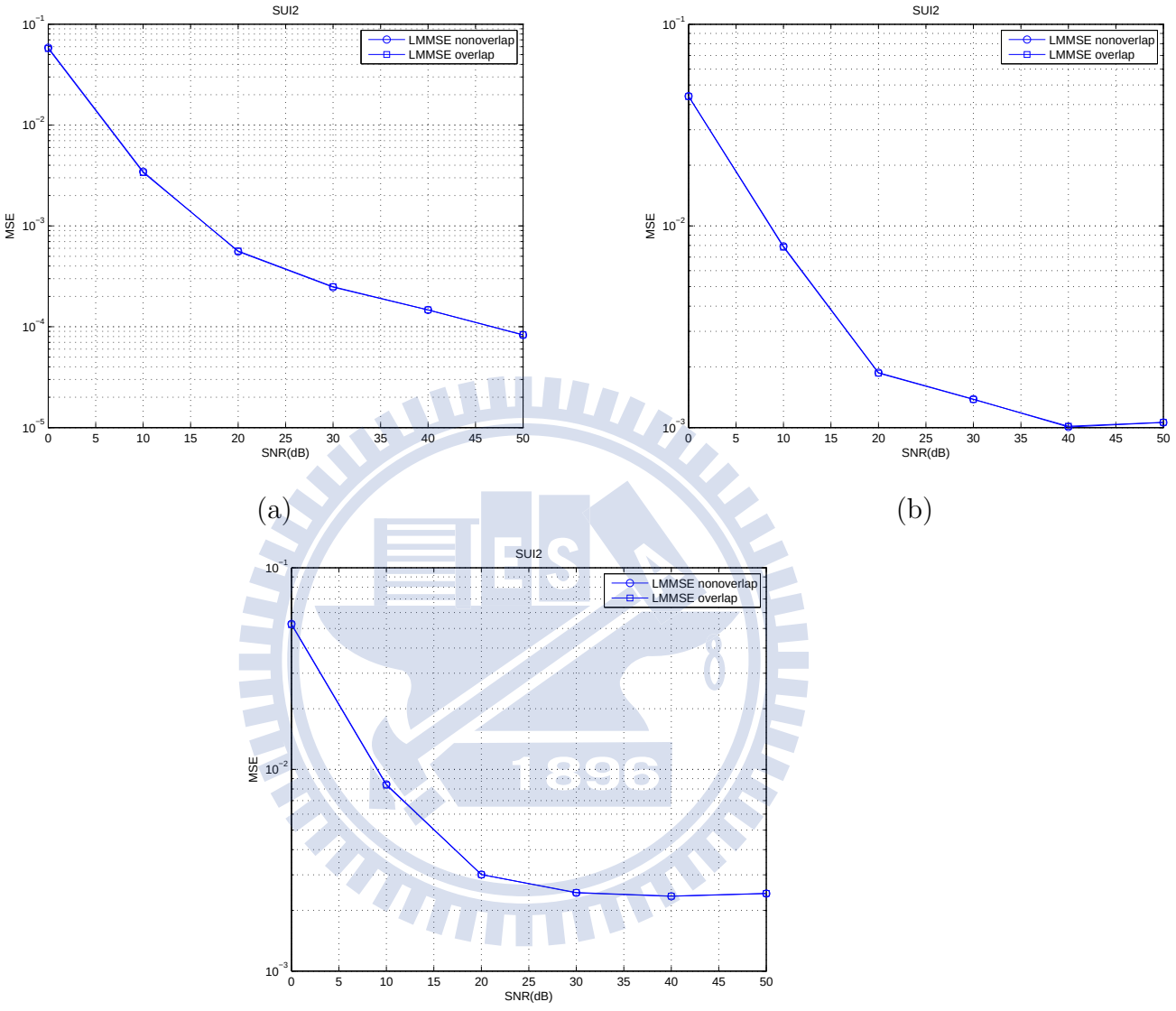

Figure 4.22: MSE performance for FD LMMSE with overlapped and non-overlapped R'_C window and submatrix size is $S_L = 12$ in SUI2 fading channel at speeds: (a) 3 km/h, (b) 60 km/h, and (c) 120 km/h.

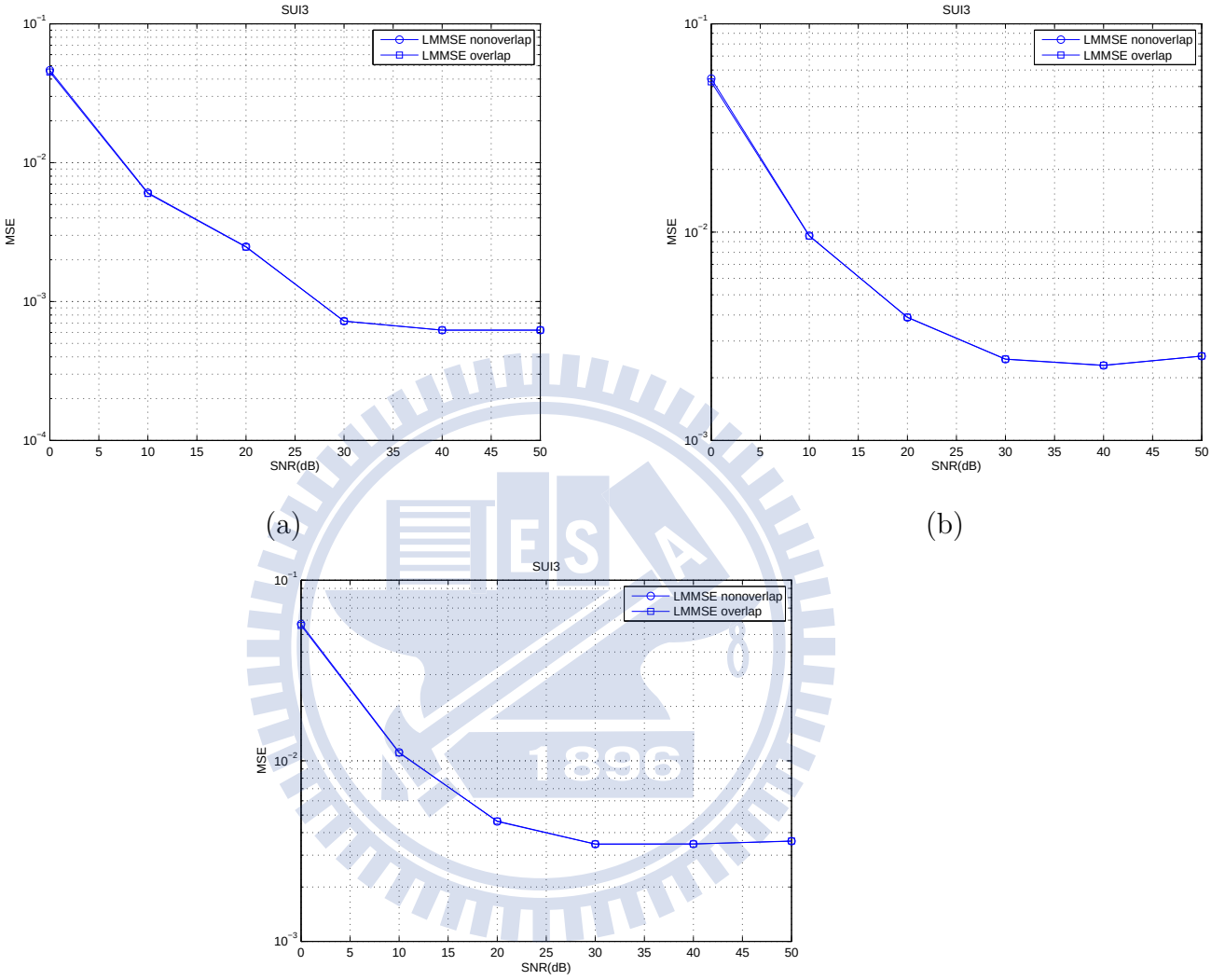

Figure 4.23: MSE performance for FD LMMSE with overlapped and non-overlapped R'_C window and submatrix size is $S_L = 12$ in SUI3 fading channel at speeds: (a) 3 km/h, (b) 60 km/h, and (c) 120 km/h.

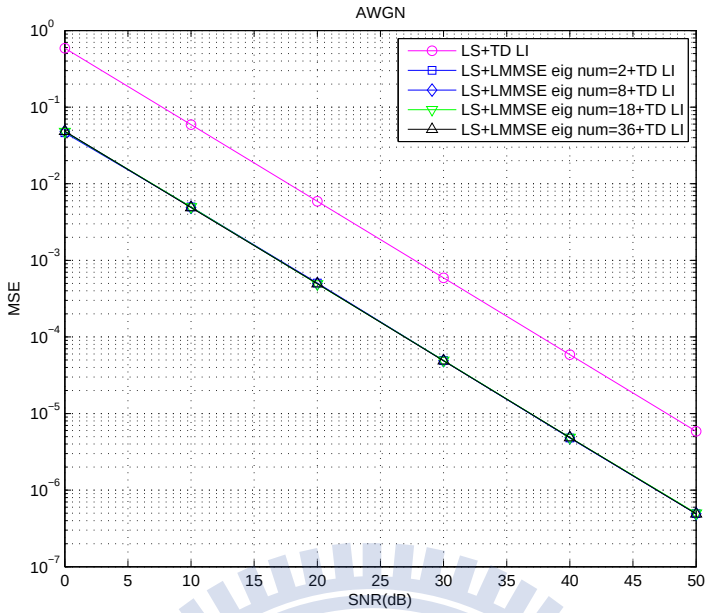

Figure 4.24: MSE performance for FD LMMSE in AWGN channel with different numbers of retained eigenvalues for R'_C.

the noise enhancement of the LMMSE matrix, but it can also ignore the smaller eigenvalues and reduce the amount of computation. The simulation data for the AWGN channel are shown in Figure 4.24. In this case, there are usually only one or two large singular values. Therefore, only two or three eigenvalues will need to be calculated because all the estimated value will be the same as the entire operation's estimated value. The results for single-path Rayleigh, SUI1 and SUI2 channel are shown separately in Figures 4.25–4.27. We can see that the number of calculated eigenvalues do not affect MSE performance much.

4.3 Channel Estimation MSE of MIMO Channels

We also employ the simulation condition given in Section 4.1 in simulation of MIMO channel estimation. We consider the TD and FD channel separation methods, and we also simulation the additional use of FD LMMSE and GWD.

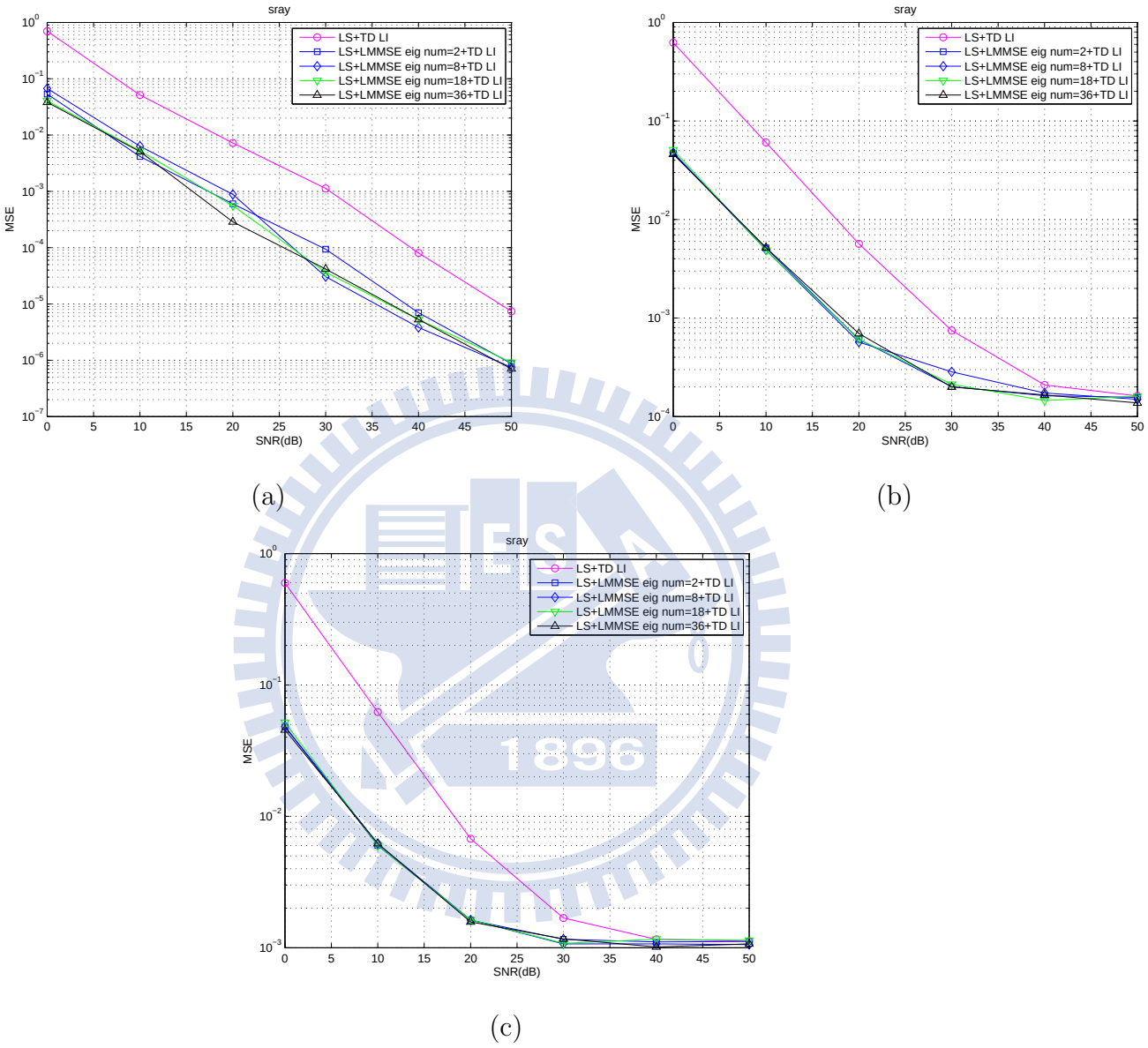

Figure 4.25: MSE performance for FD LMMSE in single-path Rayleigh fading channel at speeds (a) 3 km/h, (b) 60 km/h, and (c) 120 km/h with different numbers of retained eigenvalues for R'_C.

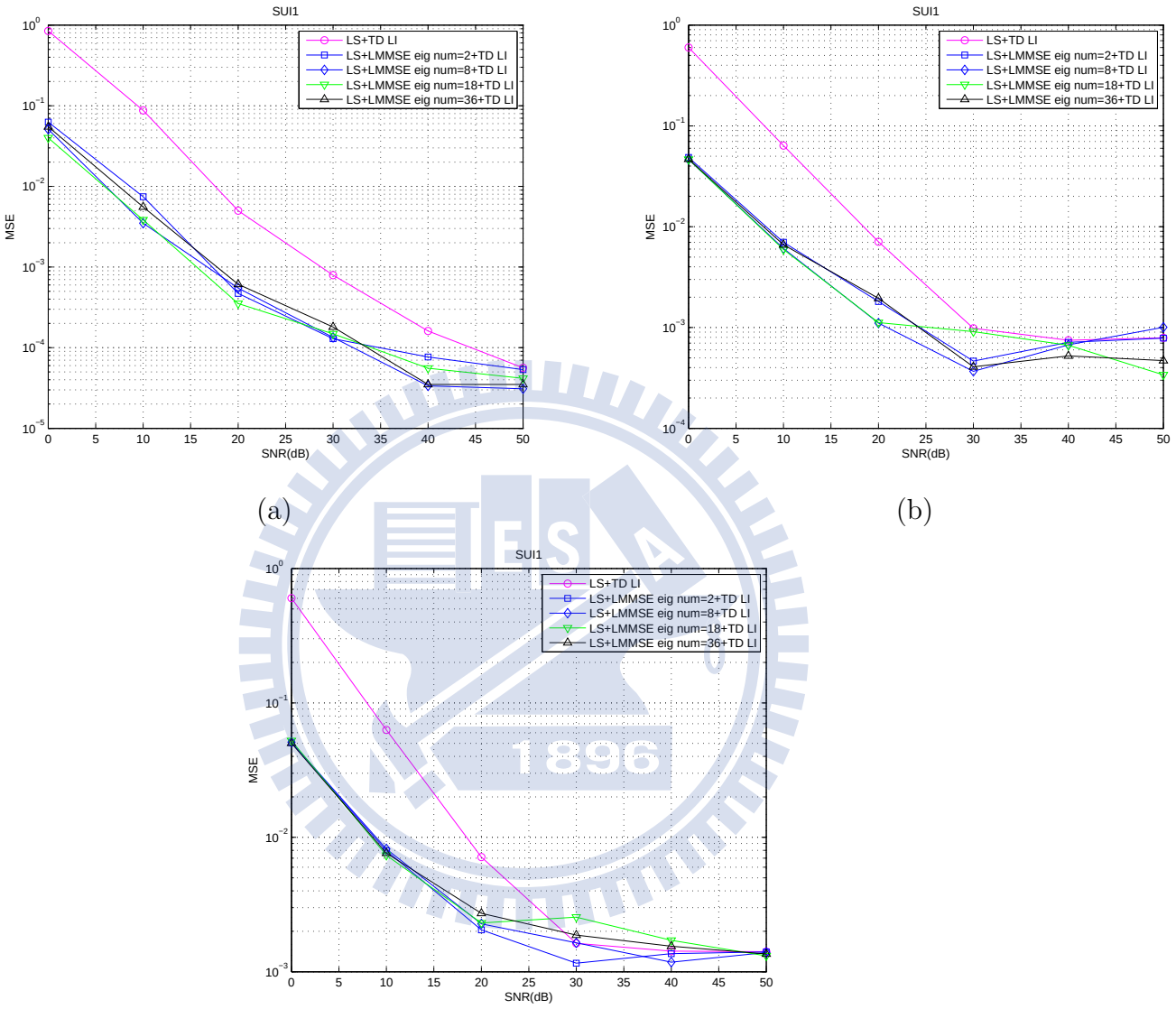

Figure 4.26: MSE performance for FD LMMSE in SUI1 fading channel at speeds (a) 3 km/h, (b) 60 km/h, and (c) 120 km/h with different numbers of retained eigenvalues for R'_C.

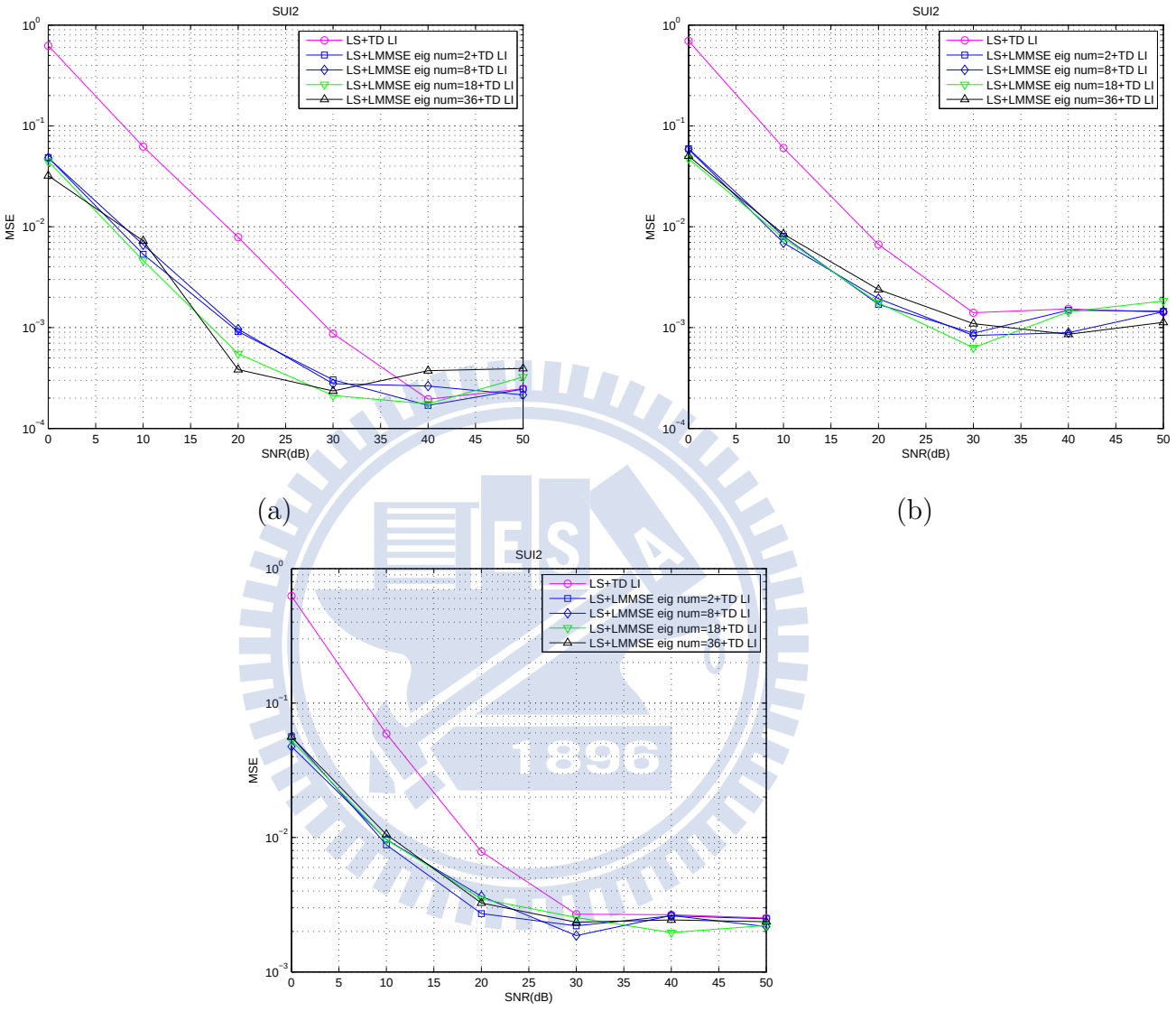

Figure 4.27: MSE performance for FD LMMSE in SUI2 fading channel at speeds (a) 3 km/h, (b) 60 km/h, and (c) 120 km/h with different numbers of retained eigenvalues for R'_C.

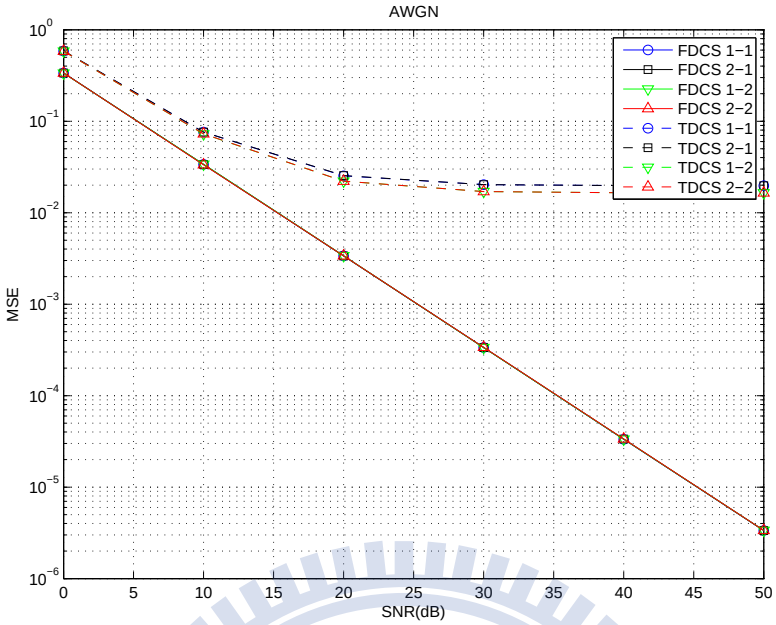

Figure 4.28: MSE performance of different channel separation methods in 2×2 MIMO over AWGN channel.

4.3.1 FD and TD Channel Separation

Figures 4.28 and 4.29 show the MSE performance of the FD channel separation (FDCS) and TD channel separation (TDCS) methods over the AWGN channel for 2×2 and 4×4 transmission, respectively. The MSE performance for the path from transmit antenna t to receive antenna l is marked $t - l$ in the legend. Clearly, the FD method performs better than the TD method. This is because the FD method does not suffer from the leakage power problem as the TD method, as explained in chapter 3. The leakage power problem aggravates with the increase in number of antenna which results in the higher MSE floor in Figure 4.29 compared to Figure 4.28. Note that the MSE performance of each path is about the same. So in subsequent performance figures we will show the average performance of all antenna paths.

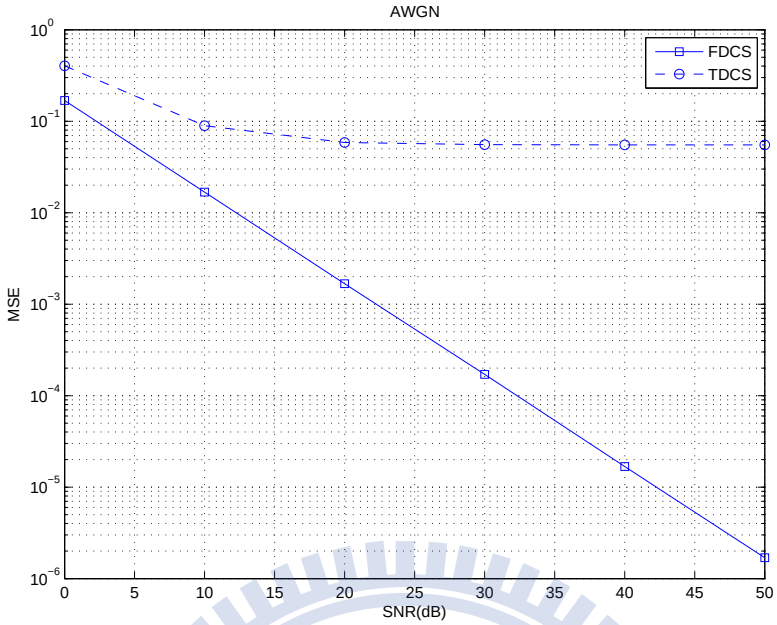

Figure 4.29: MSE performance of different channel separation methods in 4×4 MIMO over AWGN channel.

Next we consider the single-path Rayleigh, SUI1, SUI2 and SUI3 channels. Figure 4.30 shows the MSE performance of FDCS and TDCS for single-path Rayleigh 2×2 channels. We can find that in FDCS, the characteristic for 2×2 MIMO is similar to SISO shown in Figure 4.5. Due to antenna correlation matrix, in the multi-path channel, the performance of FDCS is worse nearly than SISO system. As in Figure 4.34 we slow the performance in estimating 4×4 MIMO channels, where we note that 4×4 MIMO is similar to 2×2 MIMO. This is because FDCS evenly average over the noise and transmitted power by number of antennas. Figures 4.31–4.33 and Figures 4.35–4.37 show the result for the three SUI channels with 2×2 and 4×4 MIMO respectively. We see that FDCS can accurately separate different antenna channels.

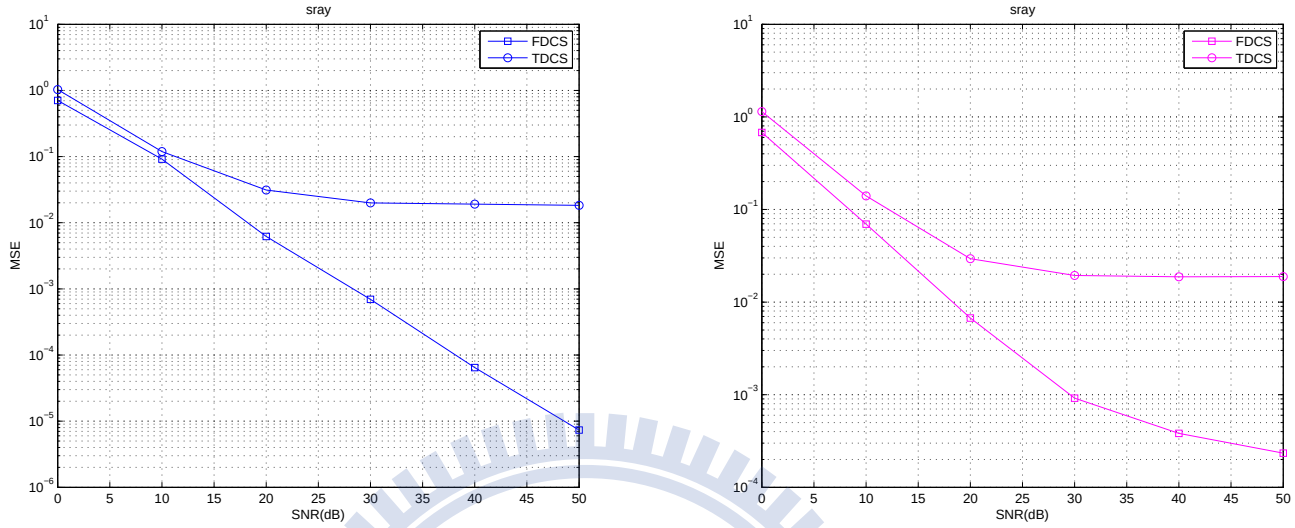

(a)(b)

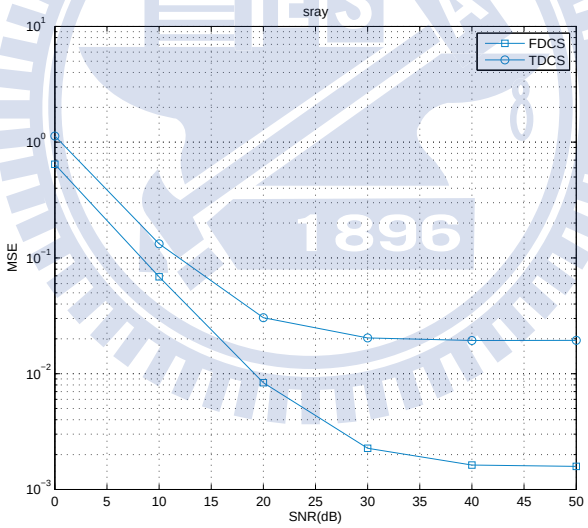

(c)

Figure 4.30: MSE performance of different channel separation methods in 2×2 MIMO over single-path Rayleigh fading channel at speeds (a) 3 km/h, (b) 60 km/h, and (c) 120 km/h.

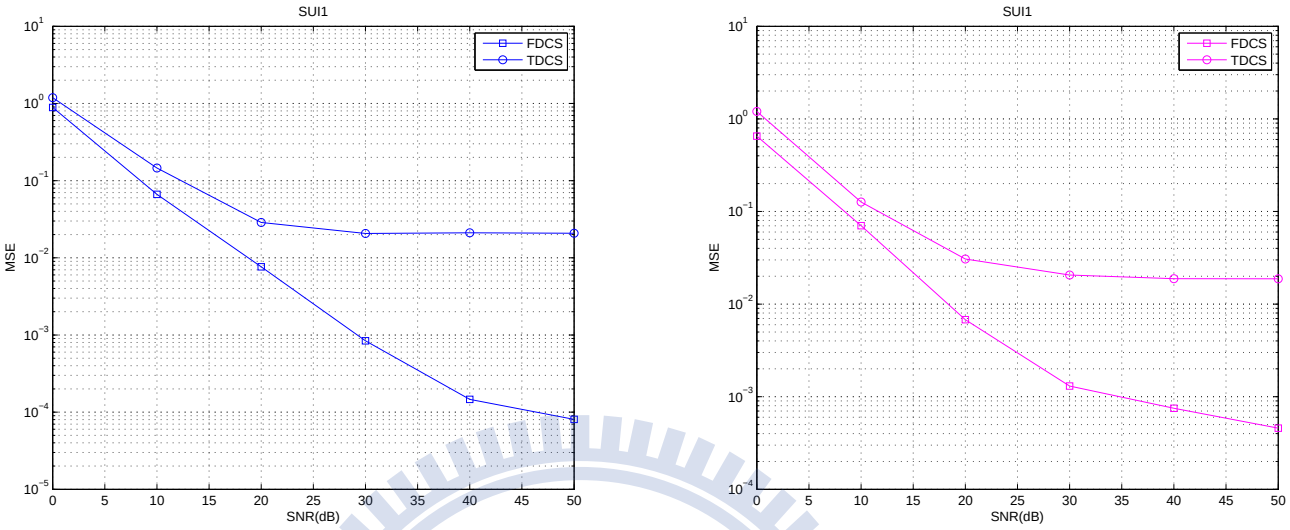

(a)(b)

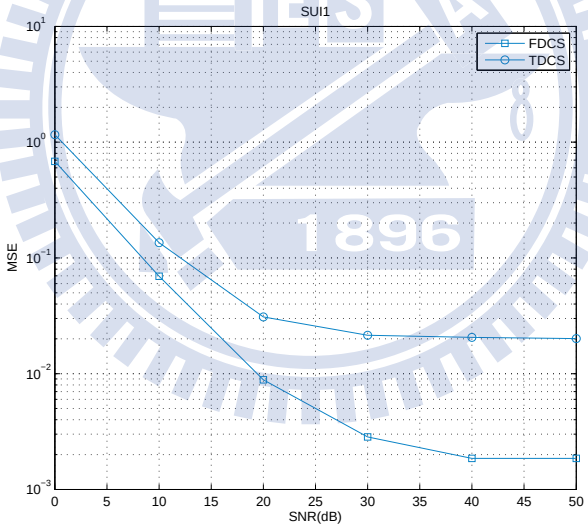

(c)

Figure 4.31: MSE performance of different channel separation methods in 2×2 MIMO over SUI1 fading channel at speeds (a) 3 km/h, (b) 60 km/h, and (c) 120 km/h.

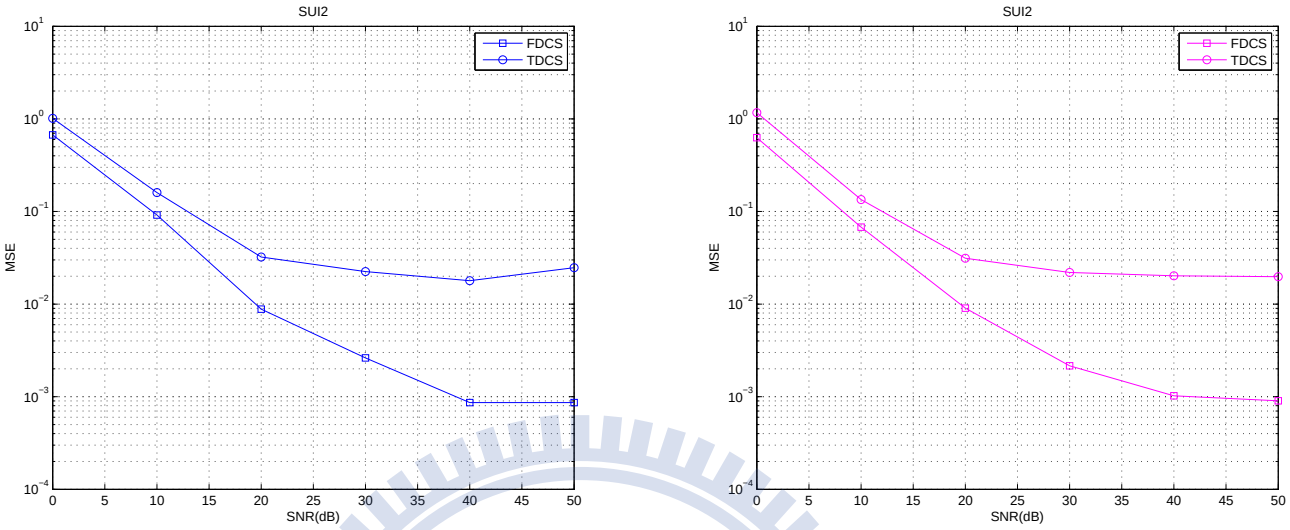

(a)(b)

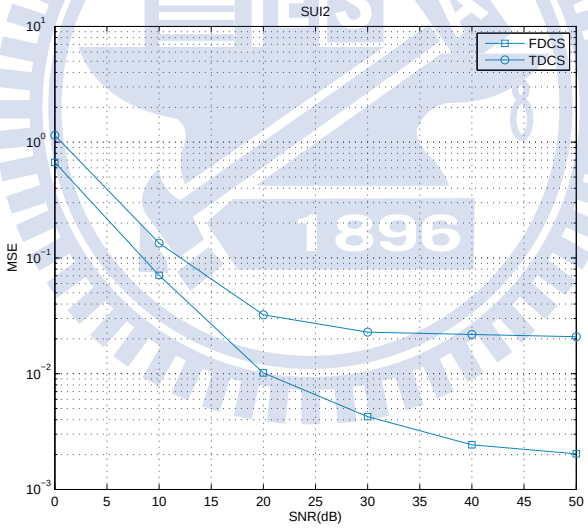

(c)

Figure 4.32: MSE performance of different channel separation methods in 2×2 MIMO over SUI2 fading channel at speeds (a) 3 km/h, (b) 60 km/h, and (c) 120 km/h.

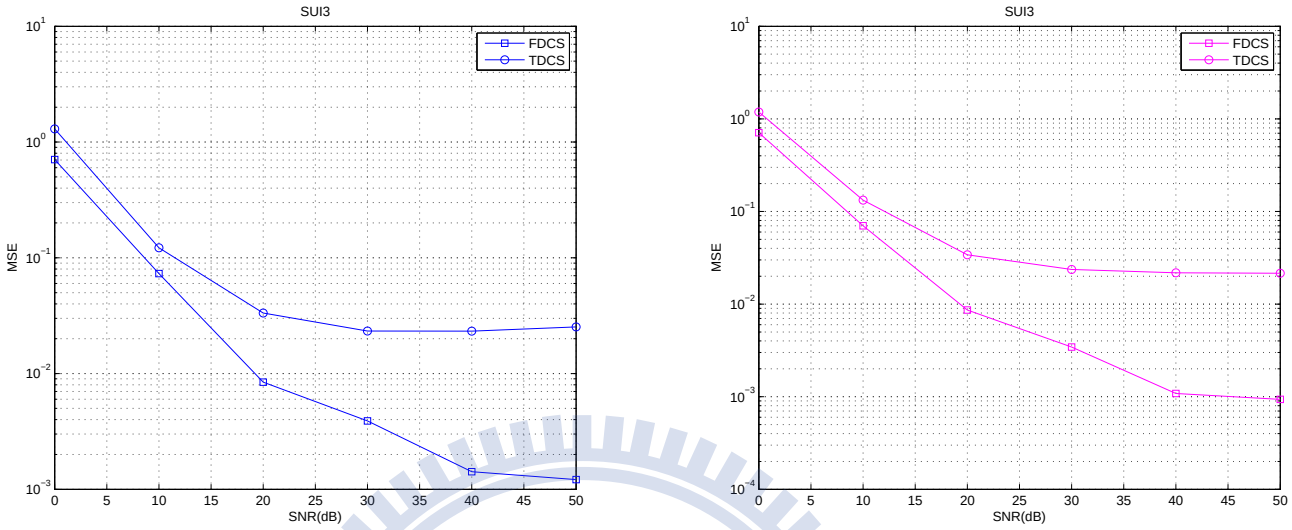

(a)(b)

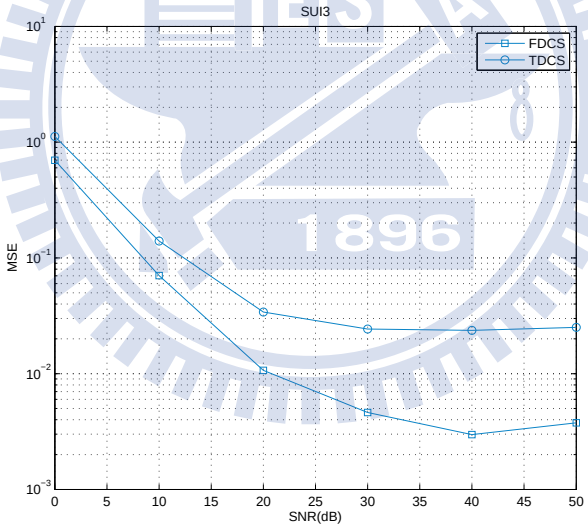

(c)

Figure 4.33: MSE performance of different channel separation methods in 2×2 MIMO over SUI3 fading channel at speeds (a) 3 km/h, (b) 60 km/h, and (c) 120 km/h.

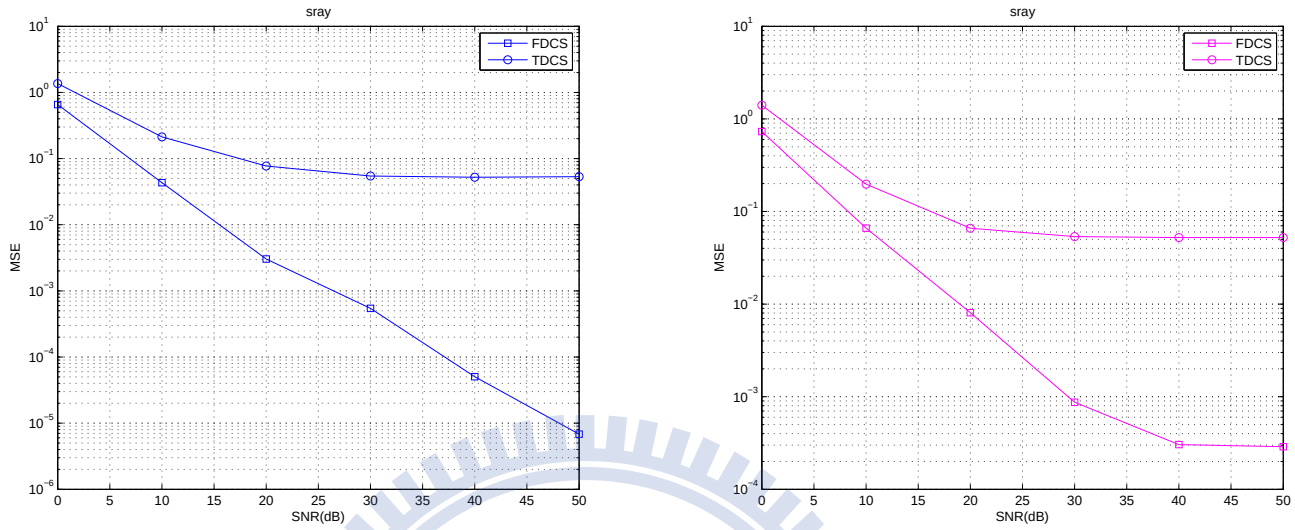

(a)(b)

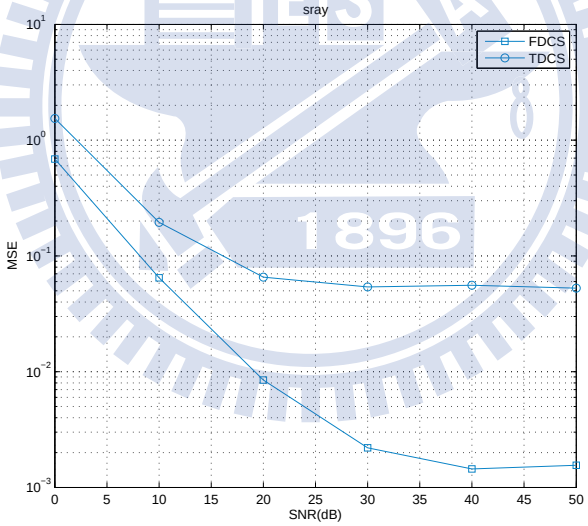

(c)

Figure 4.34: MSE performance of different channel separation methods in 4×4 MIMO over single-path Rayleigh fading channel at speeds (a) 3 km/h, (b) 60 km/h, and (c) 120 km/h.

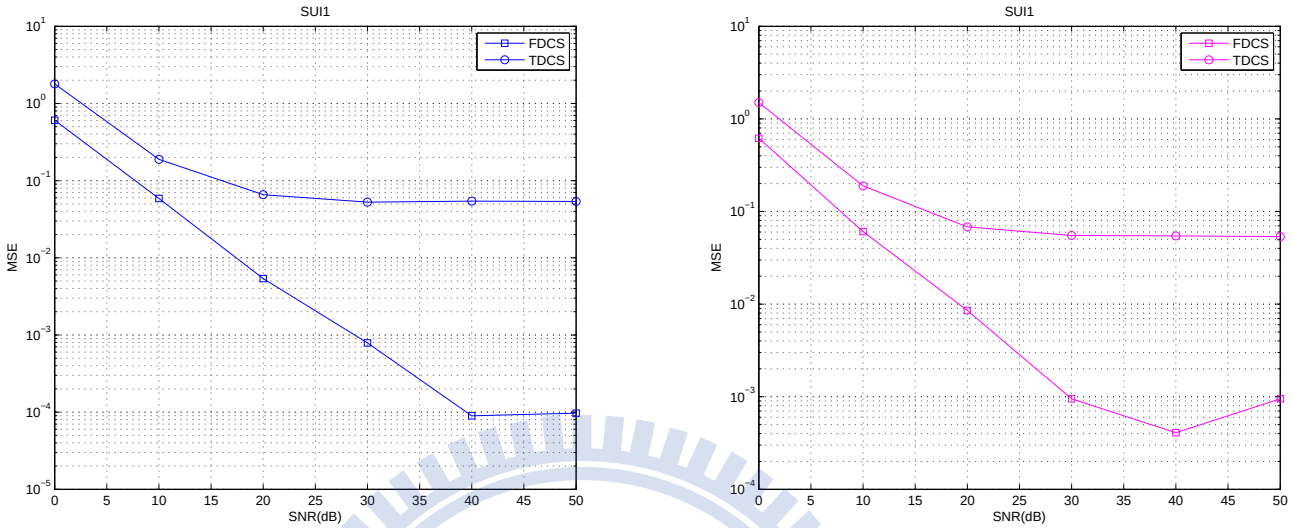

(a)(b)

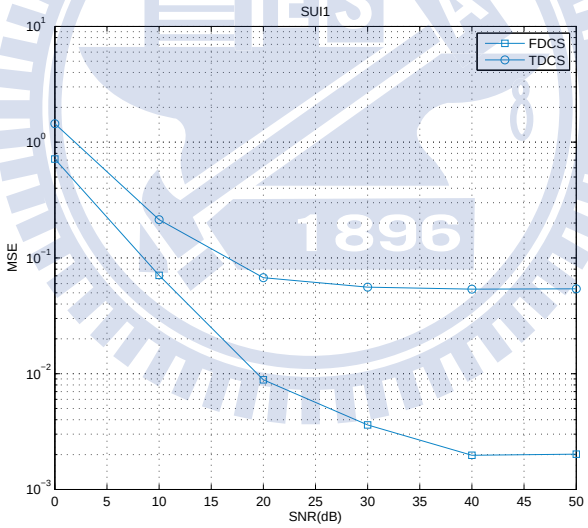

(c)

Figure 4.35: MSE performance of different channel separation methods in 4×4 MIMO over SUI1 fading channel at speeds (a) 3 km/h, (b) 60 km/h, and (c) 120 km/h.

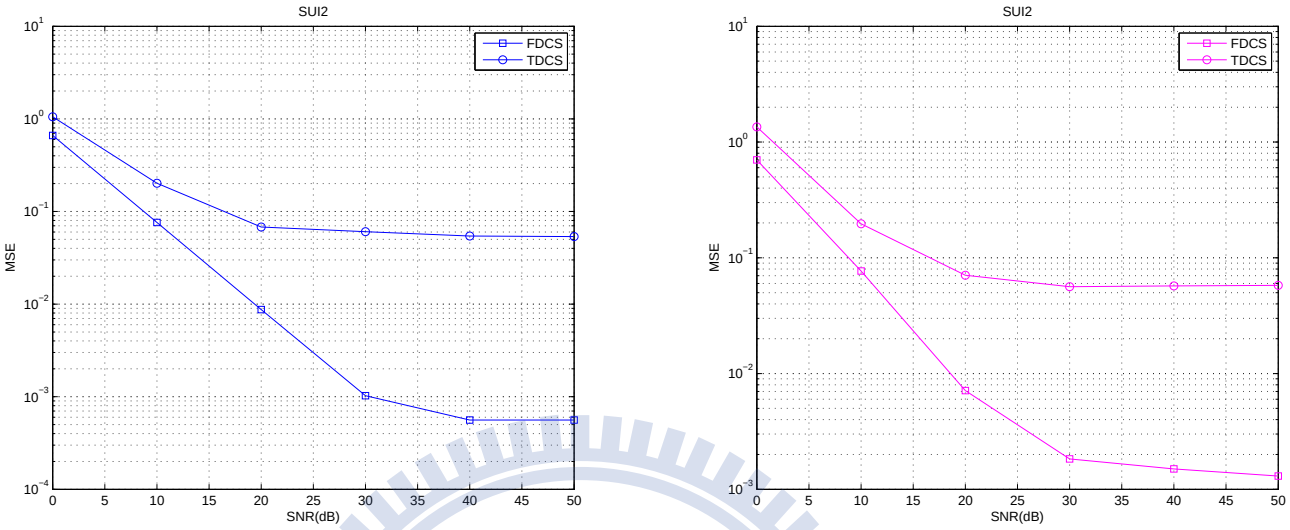

(a)(b)

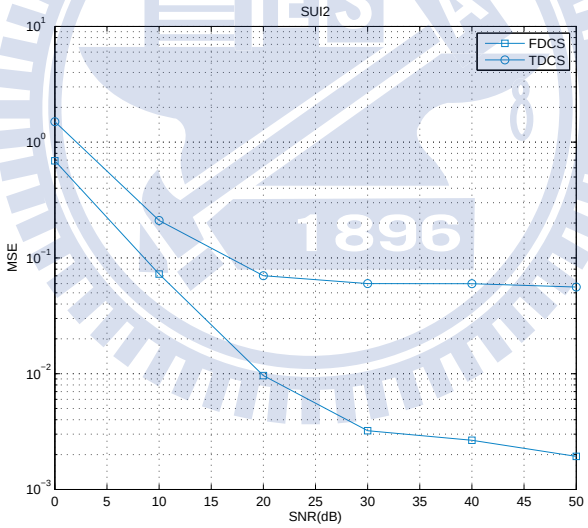

(c)

Figure 4.36: MSE performance of different channel separation methods in 4×4 MIMO over SUI2 fading channel at speeds (a) 3 km/h, (b) 60 km/h, and (c) 120 km/h.

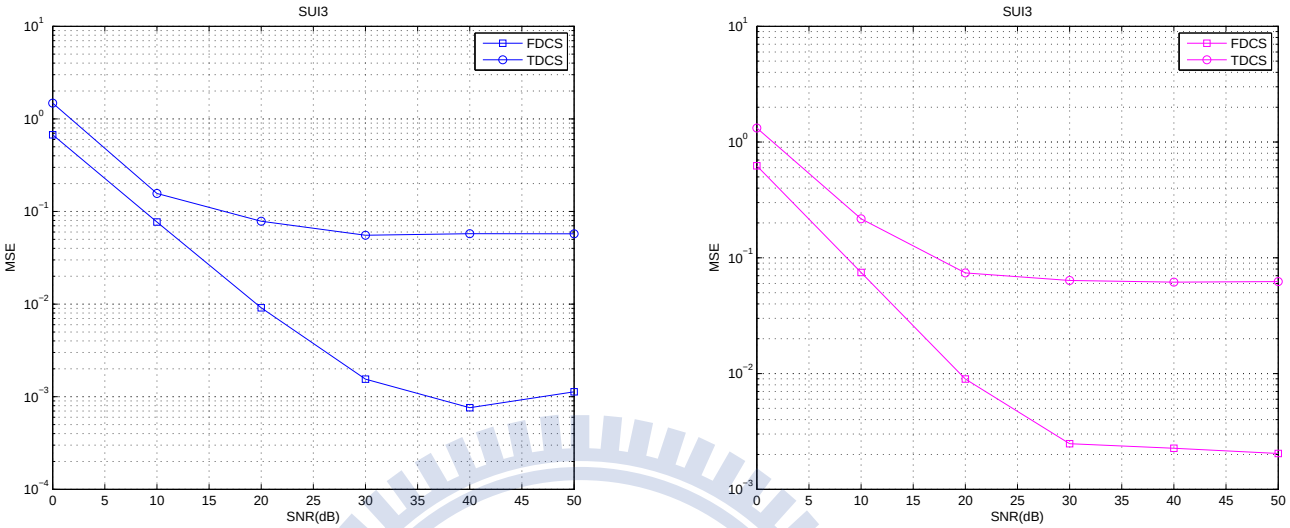

(a)(b)

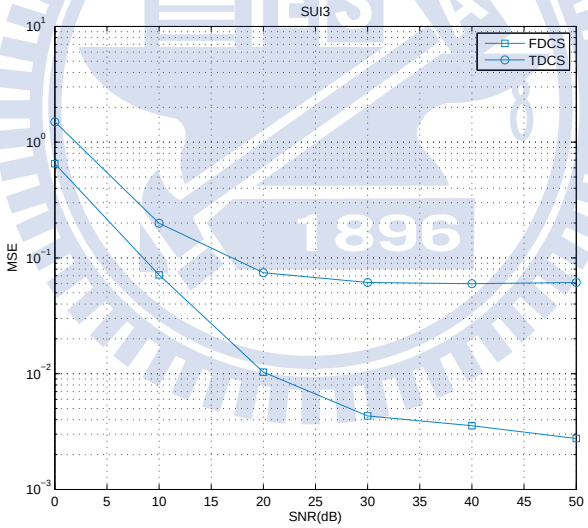

(c)

Figure 4.37: MSE performance of different channel separation methods in 4×4 MIMO over SUI3 fading channel at speeds (a) 3 km/h, (b) 60 km/h, and (c) 120 km/h.

4.3.2 Use of FD LMMSE in FD and TD Channel Separation

Now consider the frequency domain estimation methods introduced in the previous chapter: LMMSE and GWD. After estimating the channel response of each path by FDCS or TDCS, we conduct such a frequency domain estimation. First, we show the result with FD LMMSE in 2×2 and 4×4 MIMO over the AWGN in Figures 4.38 and 4.39, respectively. Comparing with Figures 4.28 and 4.29, we see that the effect of FD LMMSE is similar to the SISO case, that is, the MSE will drop by a multiple. This multiple is dependent on the submatrix size used in FD LMMSE. However, because FDCS already combines several neighboring subcarriers' channel responses in solving linear equations, this step averages the noise in the frequency domain. So in 2×2 MIMO the multiplicative reduction in MSE is half the FD LMMSE submatrix size. Similarly, in a 4×4 MIMO system, the MSE reduction multiple is one-fourth the FD LMMSE submatrix size. For TDCS, in addition to averaging noise-induced error, LMMSE will also average leakage power error, so the MSE will lower more drastically than in the case of FDCS.

Consider adding FD LMMSE to 2×2 MIMO channel estimation for single-path Rayleigh, SUI1, SUI2 and SUI3 channels as shown in Figures 4.40–4.43 and to the 4×4 MIMO channel estimation, as shown in Figures 4.44–4.47. We can see that in the fading channels, the MSE result shows analogous characteristics compared as with the AWGN channel, but the multiple is not also dependent on the submatrix size used in FD LMMSE due to the smaller coherent bandwidth in fading channel.

4.3.3 Use of FD GWD in FD and TD Channel Separation

We now replace the FD LMMSE as used in the last subsection by the FD GWD to enhance the performance of FD and TD channel separation. Figures 4.48 and 4.49 show the results for 2×2 and 4×4 MIMO, respective, in the AWGN channel. We note that the MSE performance

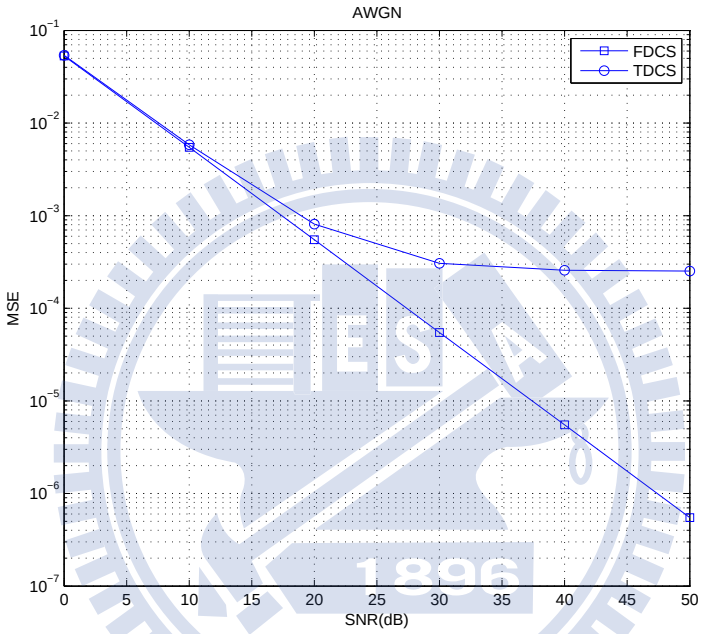

Figure 4.38: MSE performance of different channel separation methods equipped with FD LMMSE in 2×2 MIMO over AWGN channel.

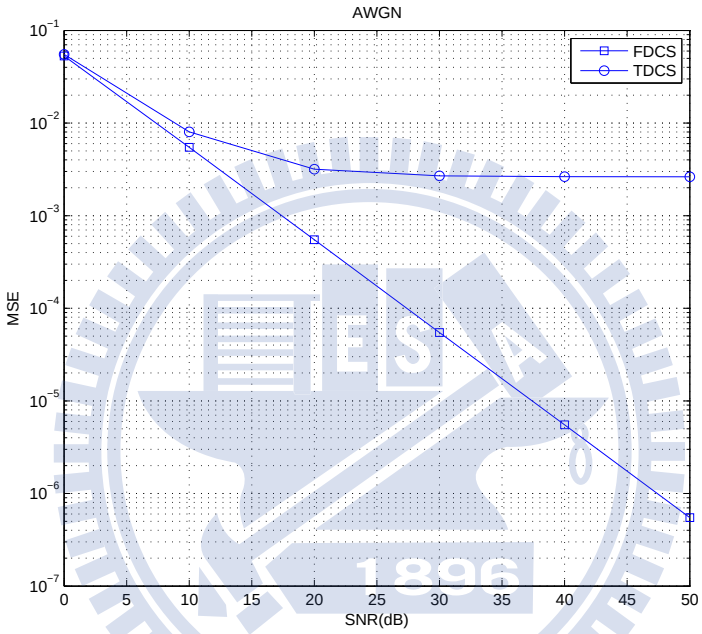

Figure 4.39: MSE performance of different channel separation methods equipped with FD LMMSE in 4×4 MIMO over AWGN channel.

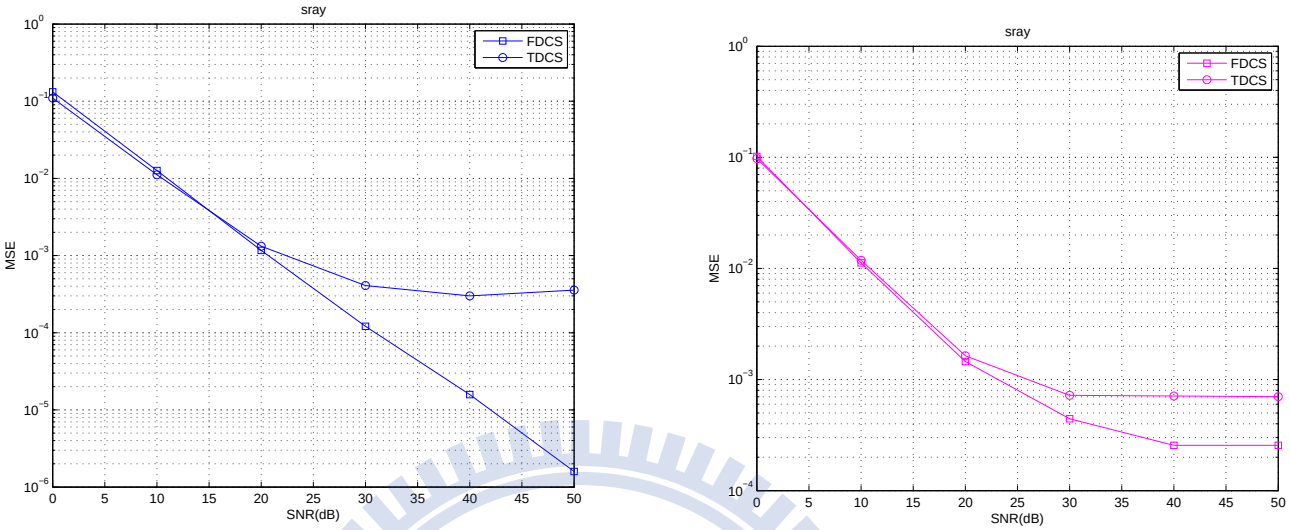

(a)(b)

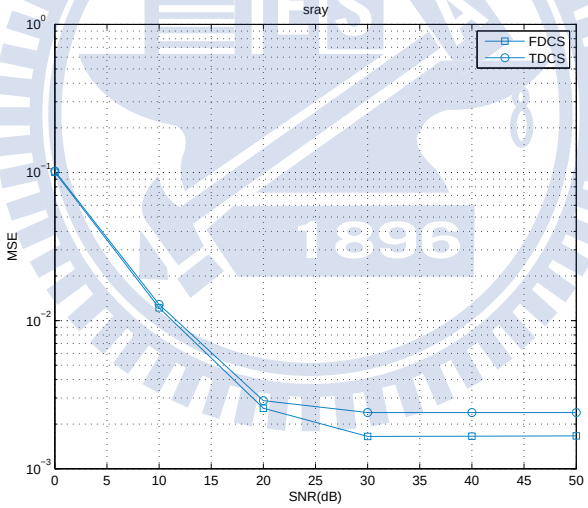

(c)

Figure 4.40: MSE performance of different channel separation methods equipped with FD LMMSE in 2×2 MIMO over single-path Rayleigh fading channel at speeds (a) 3 km/h, (b) 60 km/h, and (c) 120 km/h.

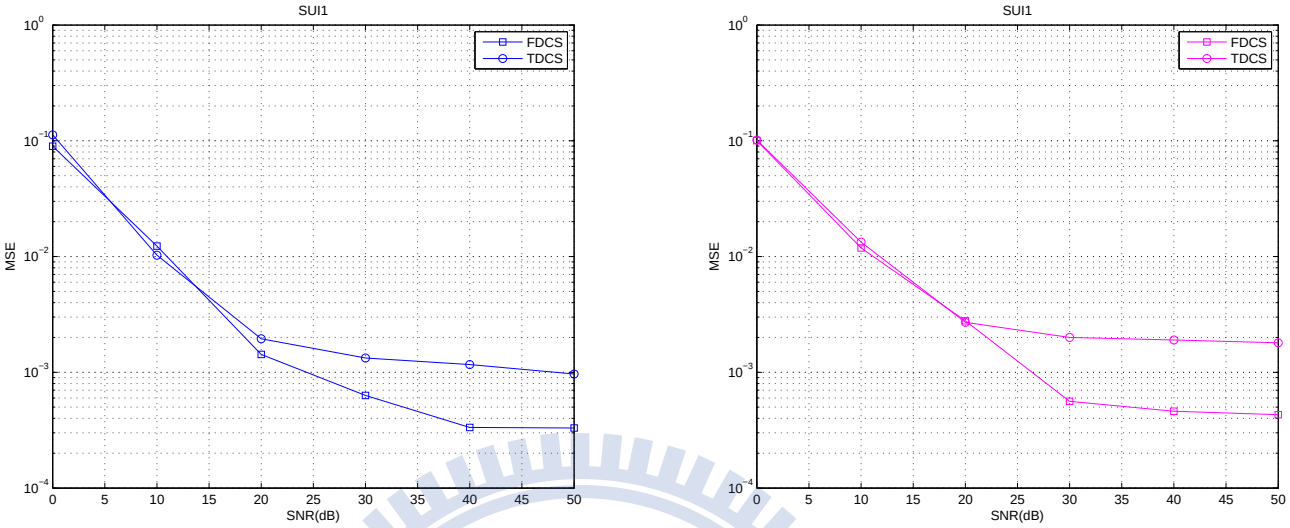

(a)(b)

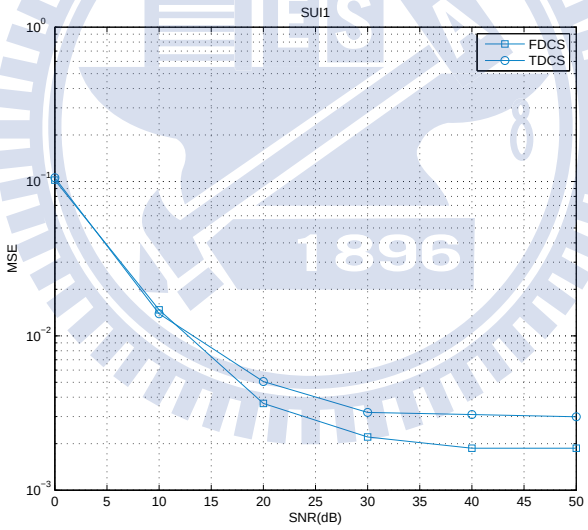

(c)

Figure 4.41: MSE performance of different channel separation methods equipped with FD LMMSE in 2×2 MIMO over SUI1 fading channel at speeds (a) 3 km/h, (b) 60 km/h, and (c) 120 km/h.

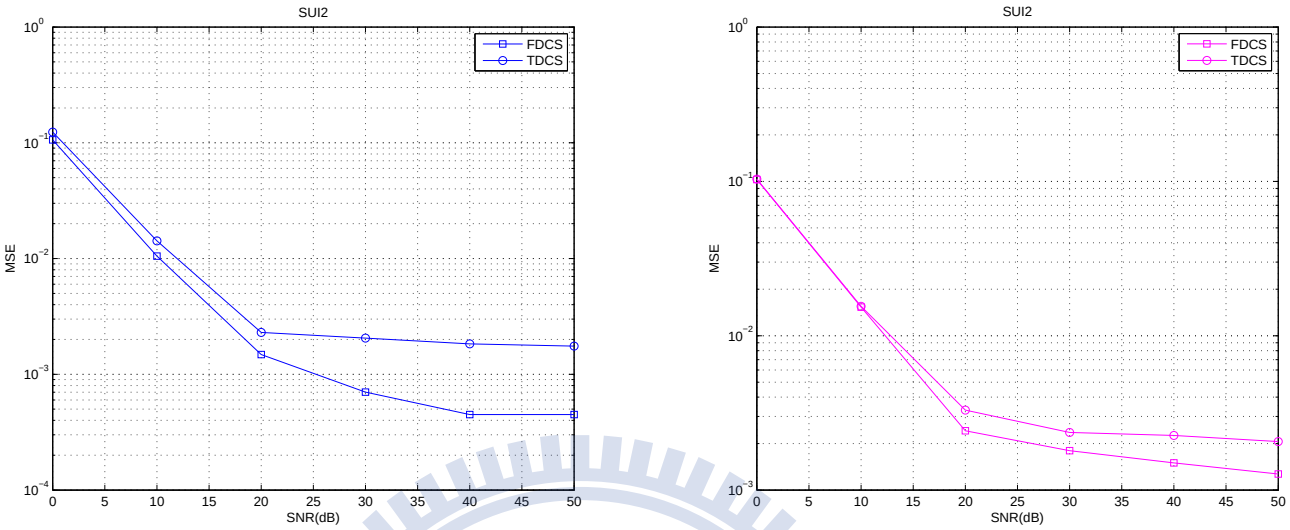

(a)(b)

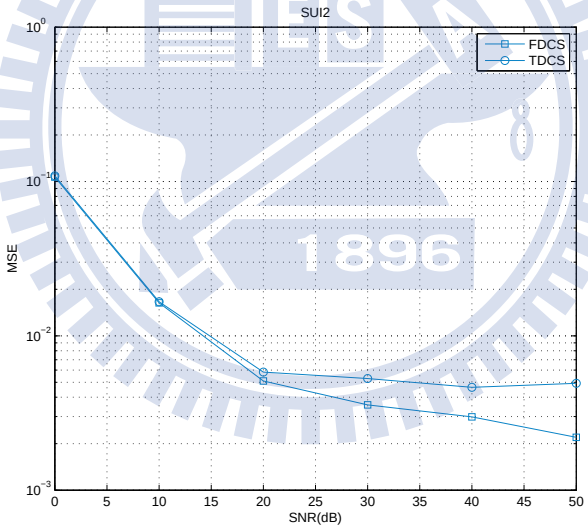

(c)

Figure 4.42: MSE performance of different channel separation methods equipped with FD LMMSE in 2×2 MIMO over SUI2 fading channel at speeds (a) 3 km/h, (b) 60 km/h, and (c) 120 km/h.

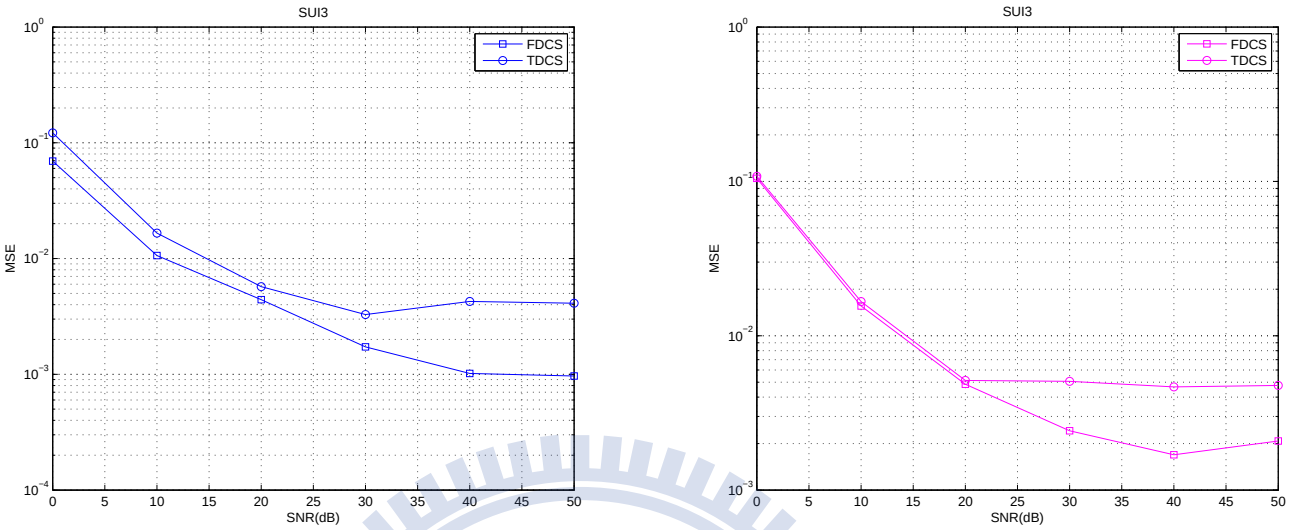

(a)(b)

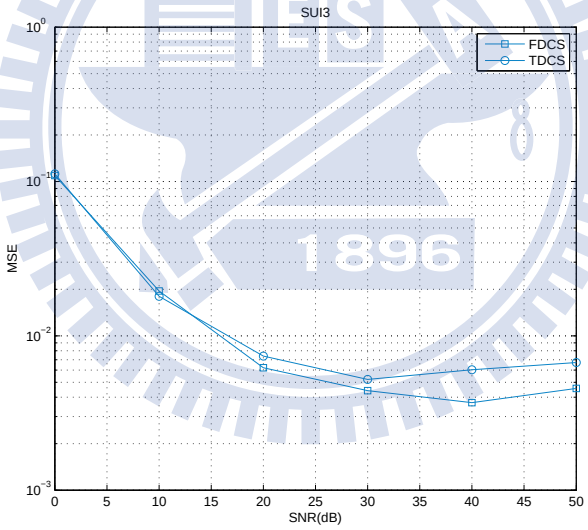

(c)

Figure 4.43: MSE performance of different channel separation methods equipped with FD LMMSE in 2×2 MIMO over SUI3 fading channel at speeds (a) 3 km/h, (b) 60 km/h, and (c) 120 km/h.

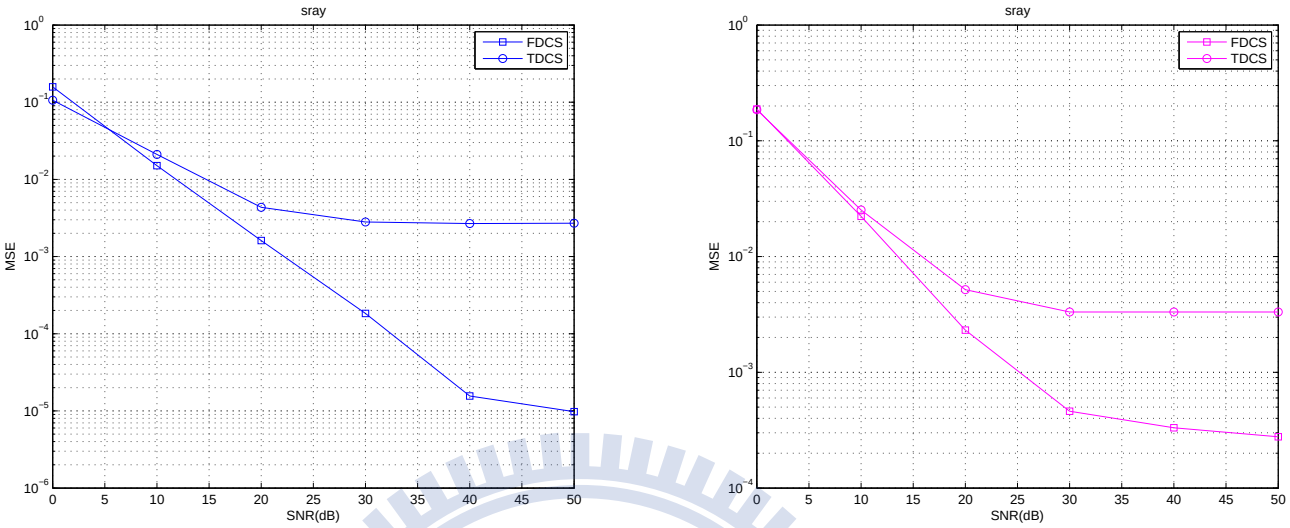

(a)(b)

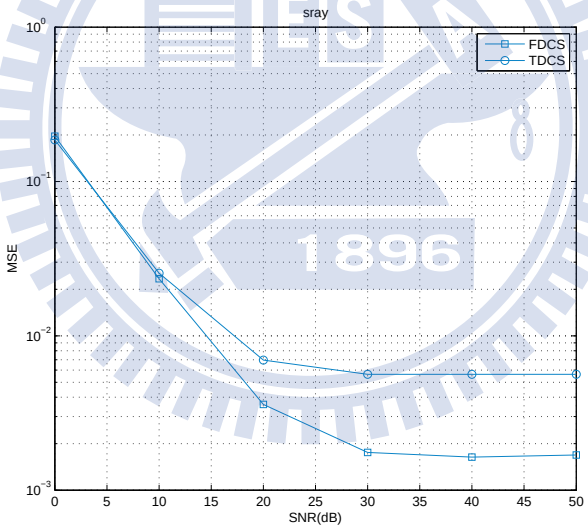

(c)

Figure 4.44: MSE performance of different channel separation methods equipped with FD LMMSE in 4×4 MIMO over single-path Rayleigh fading channel at speeds (a) 3 km/h, (b) 60 km/h, and (c) 120 km/h.

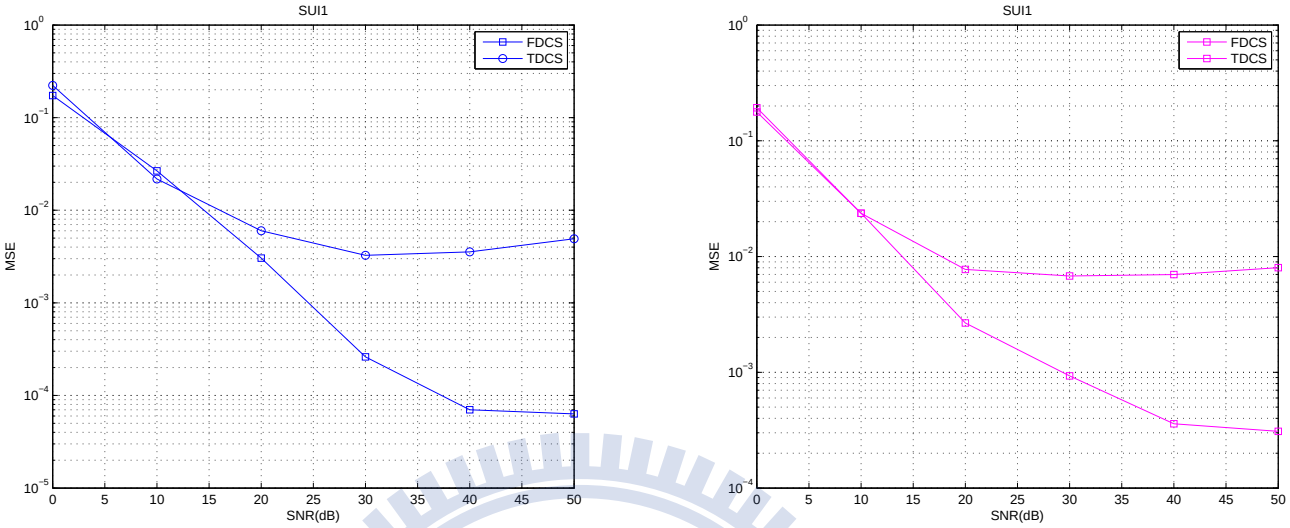

(a)(b)

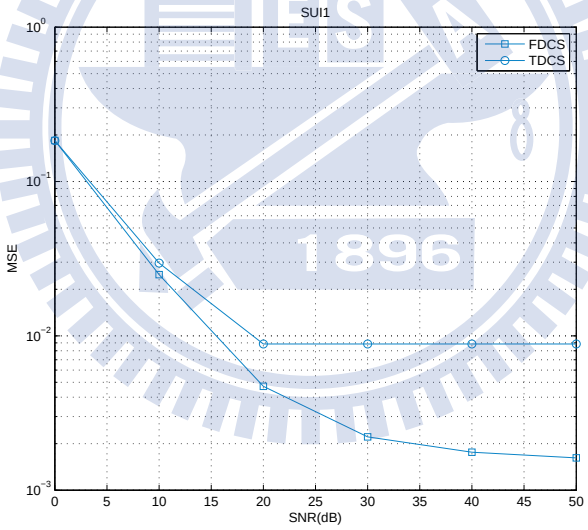

(c)

Figure 4.45: MSE performance of different channel separation methods equipped with FD LMMSE in 4×4 MIMO over SUI1 fading channel at speeds (a) 3 km/h, (b) 60 km/h, and (c) 120 km/h.

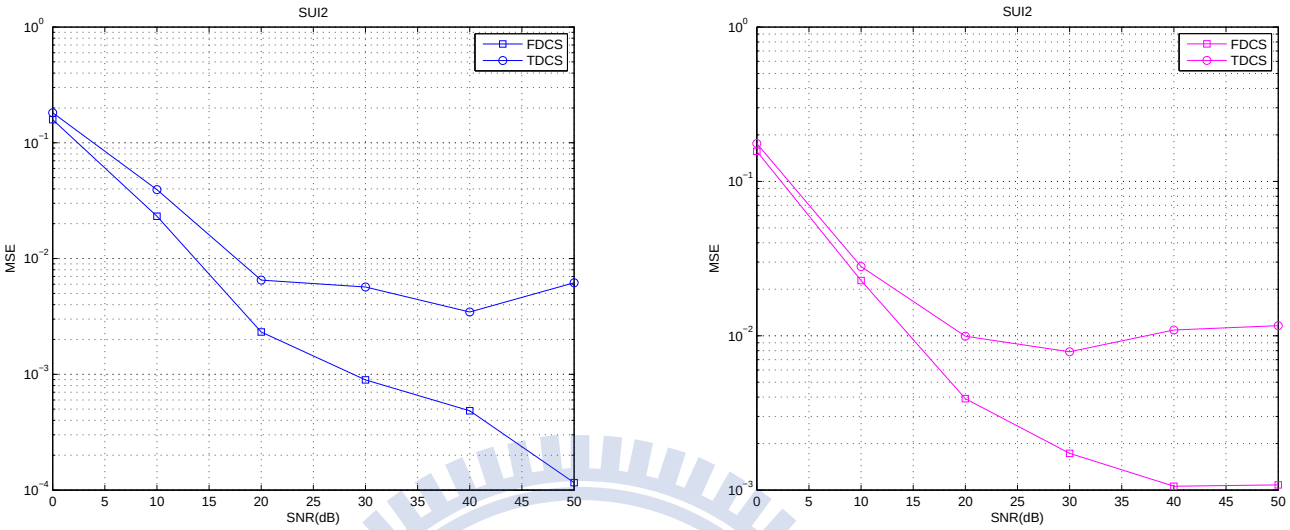

(a)(b)

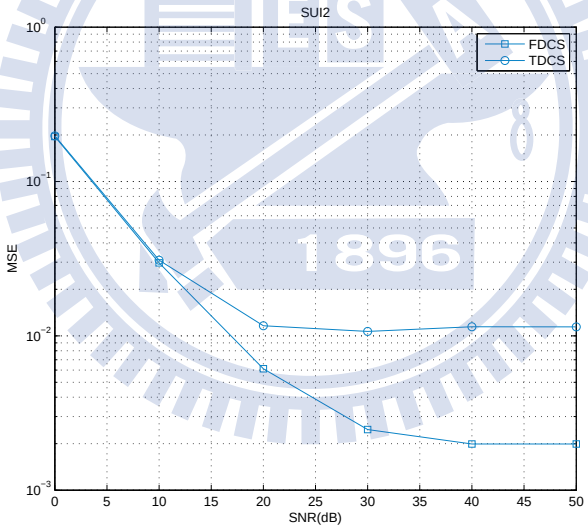

(c)

Figure 4.46: MSE performance of different channel separation methods equipped with FD LMMSE in 4×4 MIMO over SUI2 fading channel at speeds (a) 3 km/h, (b) 60 km/h, and (c) 120 km/h.

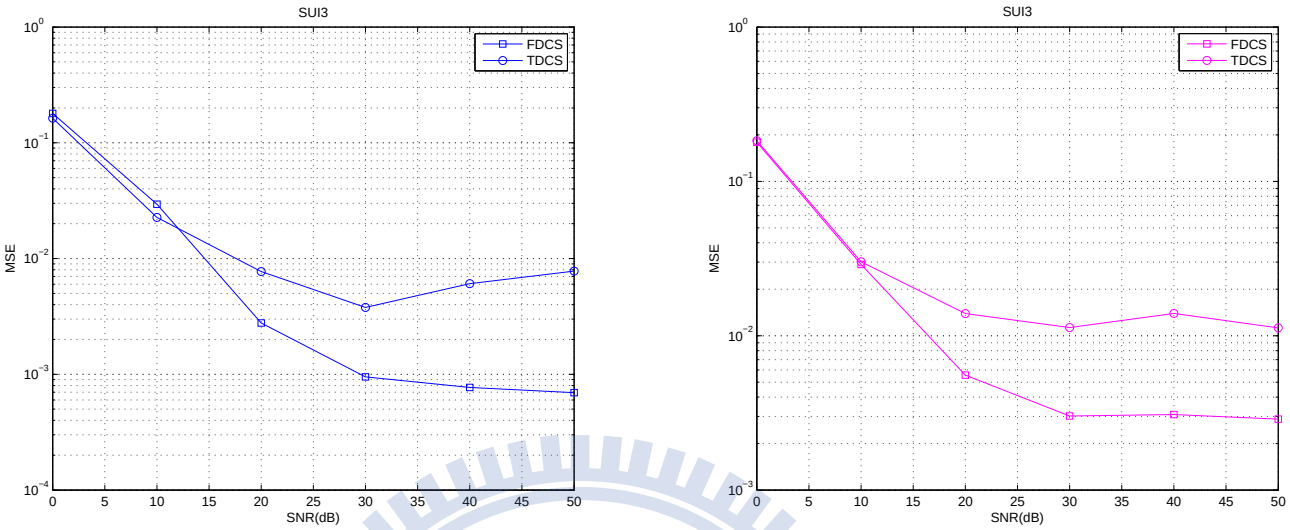

(a)(b)

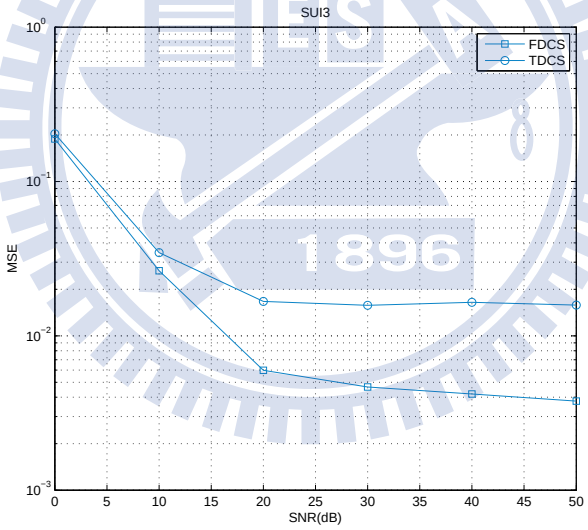

(c)

Figure 4.47: MSE performance of different channel separation methods equipped with FD LMMSE in 4×4 MIMO over SUI3 fading channel at speeds (a) 3 km/h, (b) 60 km/h, and (c) 120 km/h.

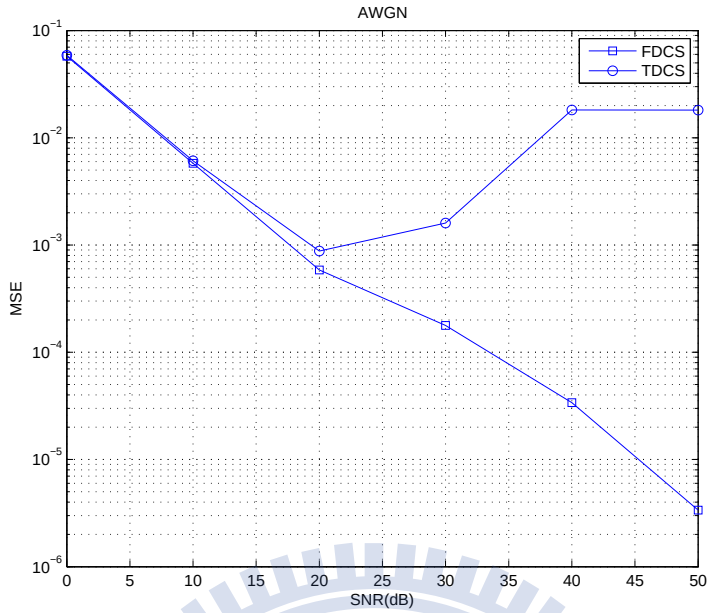

Figure 4.48: MSE performance of different channel separation methods equipped with FD GWD in 2×2 MIMO over AWGN channel.

with FDCS is similar to the use of FD LMMSE, but TDCS will produce greater errors in high SNR. This is mainly due to the narrowing of the bandwidth of the Gaussian distribution in high SNR. When the width reduces to one, the result will be the same as only doing LS channel estimation.

Consider single-path Rayleigh, SUI1, SUI2 and SUI3 adding FD GWD in the 2×2 MIMO channel estimation, as shown in Figures 4.50–4.53 and adding FD GWD simulation in the 4×4 MIMO channel estimation, as shown in Figures 4.54–4.57. We see that in the fading channels, the MSE result shows analogous characteristics as with the AWGN channel.

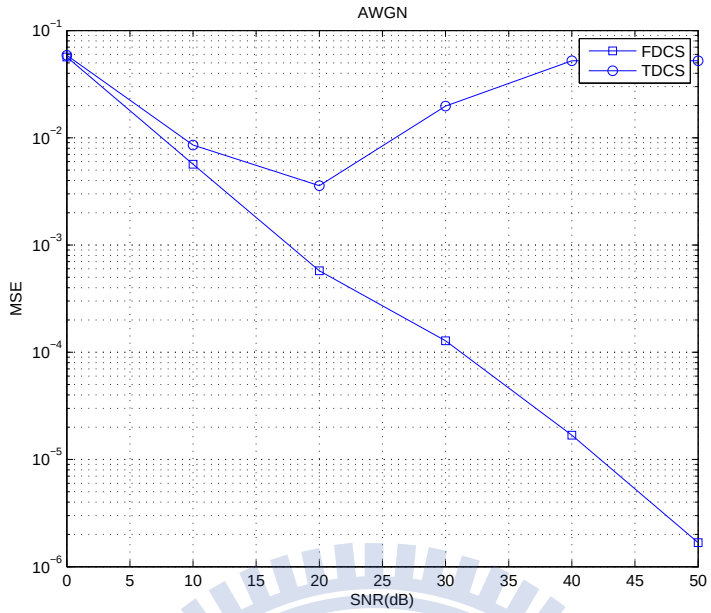

Figure 4.49: MSE performance of different channel separation methods equipped with FD GWD in 4×4 MIMO over AWGN channel.

4.4 Symbol Error Rate Results

As said before considering multipath channels, we do simulation for AWGN channel to validate the simulation model. We compare the theoretical SER curves with the SER curves resulting from simulation. For an even number of bits per symbol, the SER of rectangular QAM is given by

$$P_s = 4(1 - \frac{1}{\sqrt{M}})Q(\sqrt{\frac{3}{M-1}\frac{E_s}{N_0}}), \tag{4.5}$$

where

- M = number of symbols in modulation constellation; for example, $M = 4$ for QPSK, 16 for 16QAM, and 64 for 64QAM,
- E_s = average symbol energy,

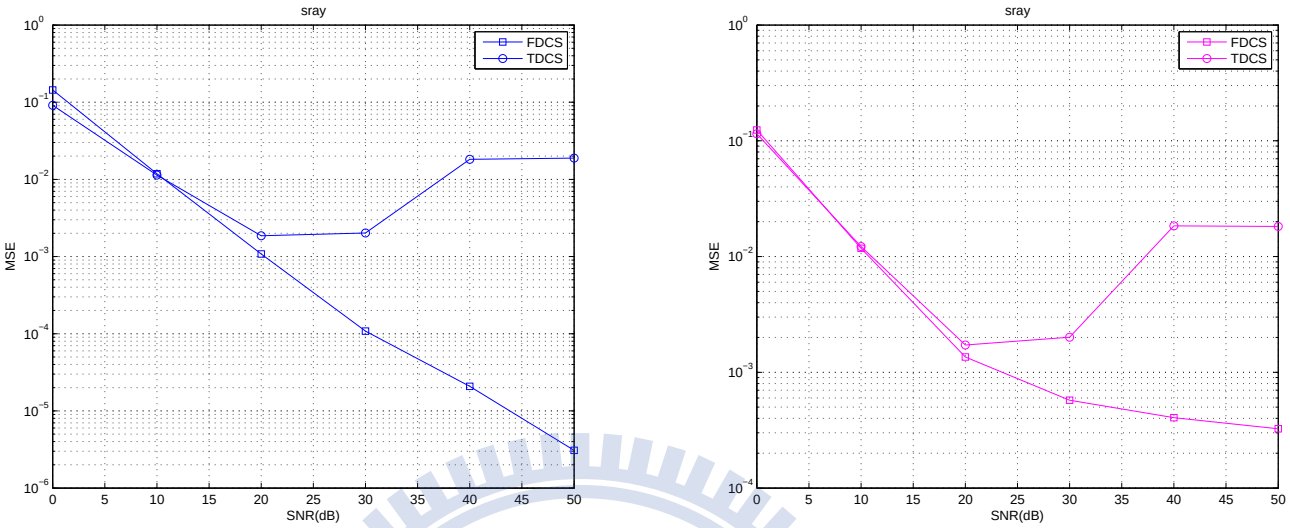

(a)(b)

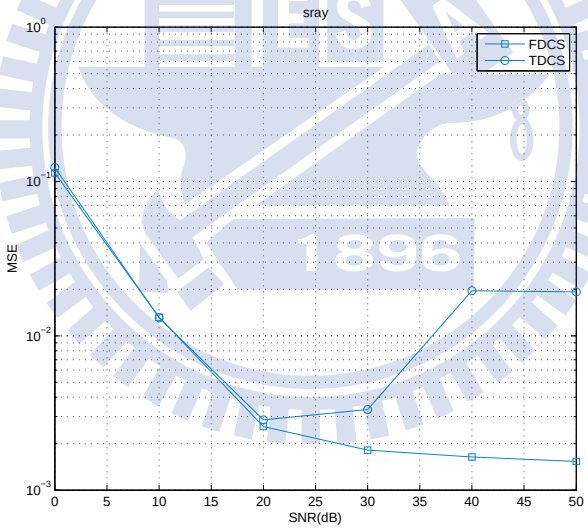

(c)

Figure 4.50: MSE performance of different channel separation methods equipped with FD GWD in 2×2 MIMO over single-path Rayleigh fading channel at speeds (a) 3 km/h, (b) 60 km/h, and (c) 120 km/h.

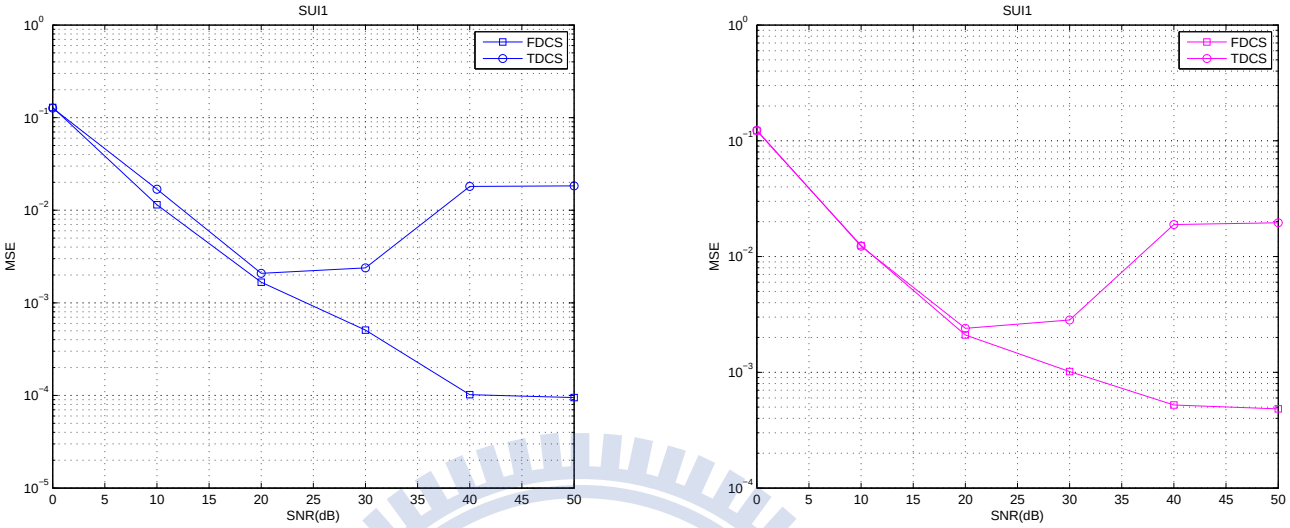

(a)(b)

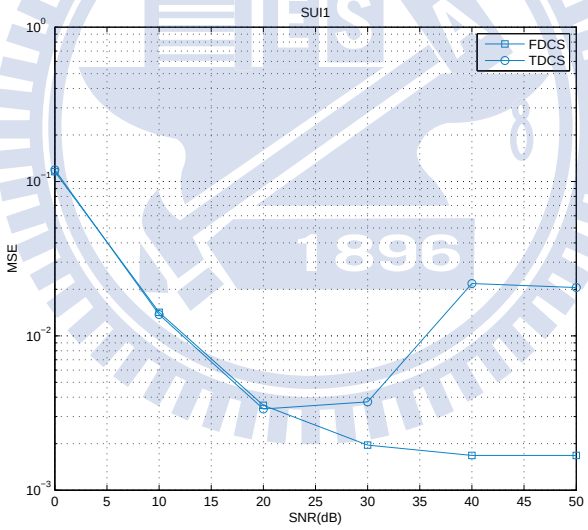

(c)

Figure 4.51: MSE performance of different channel separation methods equipped with FD GWD in 2×2 MIMO over SUI1 fading channel at speeds (a) 3 km/h, (b) 60 km/h, and (c) 120 km/h.

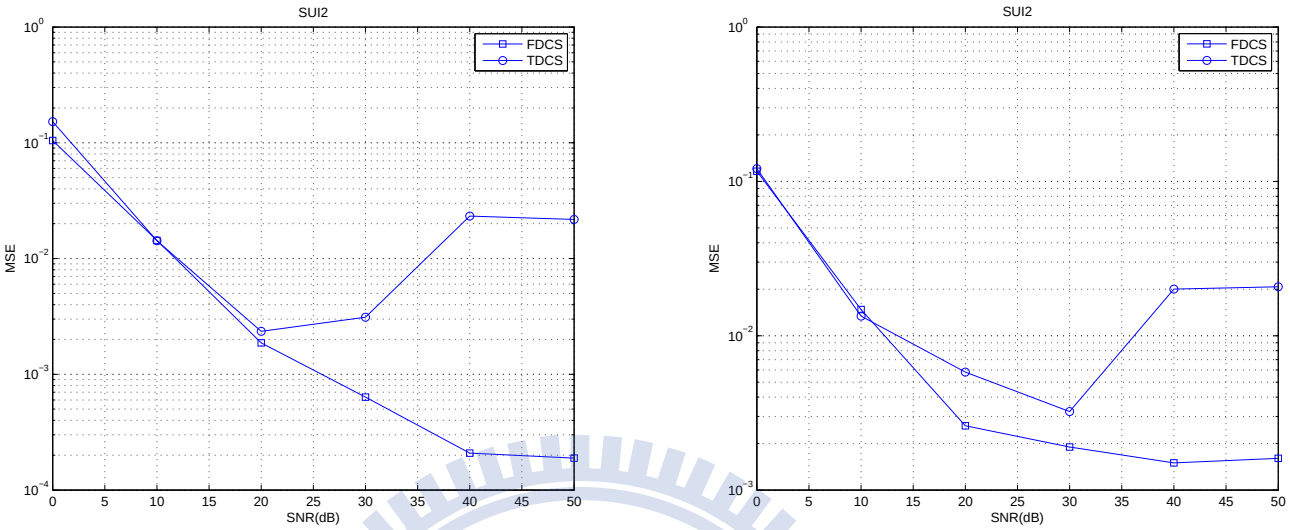

(a)(b)

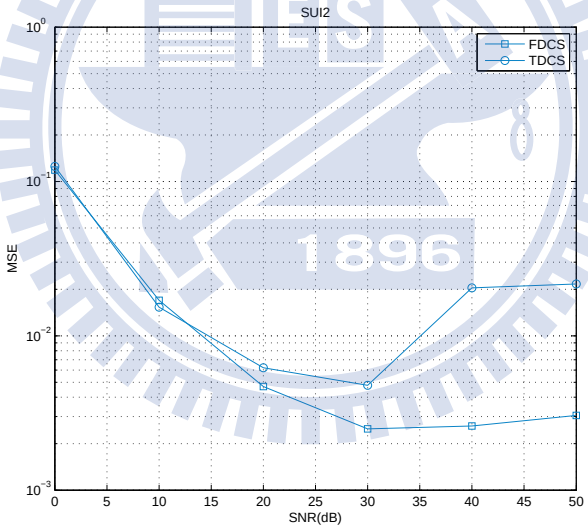

(c)

Figure 4.52: MSE performance of different channel separation methods equipped with FD GWD in 2×2 MIMO over SUI2 fading channel at speeds (a) 3 km/h, (b) 60 km/h, and (c) 120 km/h.

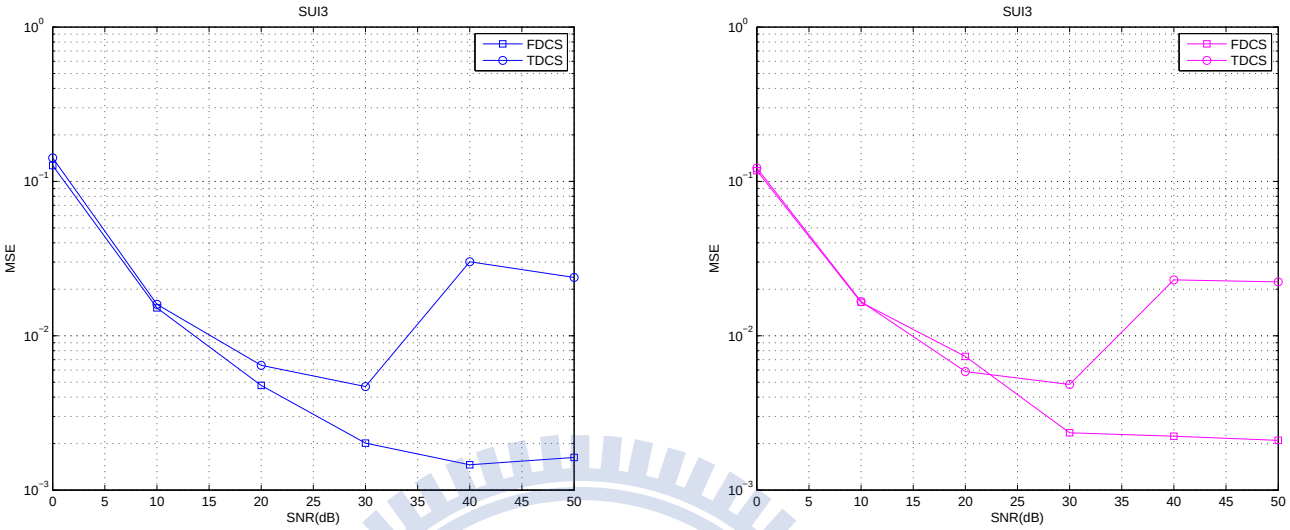

(a)(b)

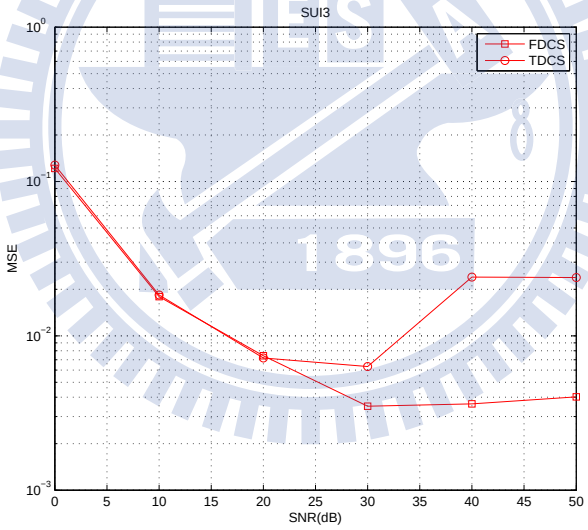

(c)

Figure 4.53: MSE performance of different channel separation methods equipped with FD GWD in 2×2 MIMO over SUI3 fading channel at speeds (a) 3 km/h, (b) 60 km/h, and (c) 120 km/h.

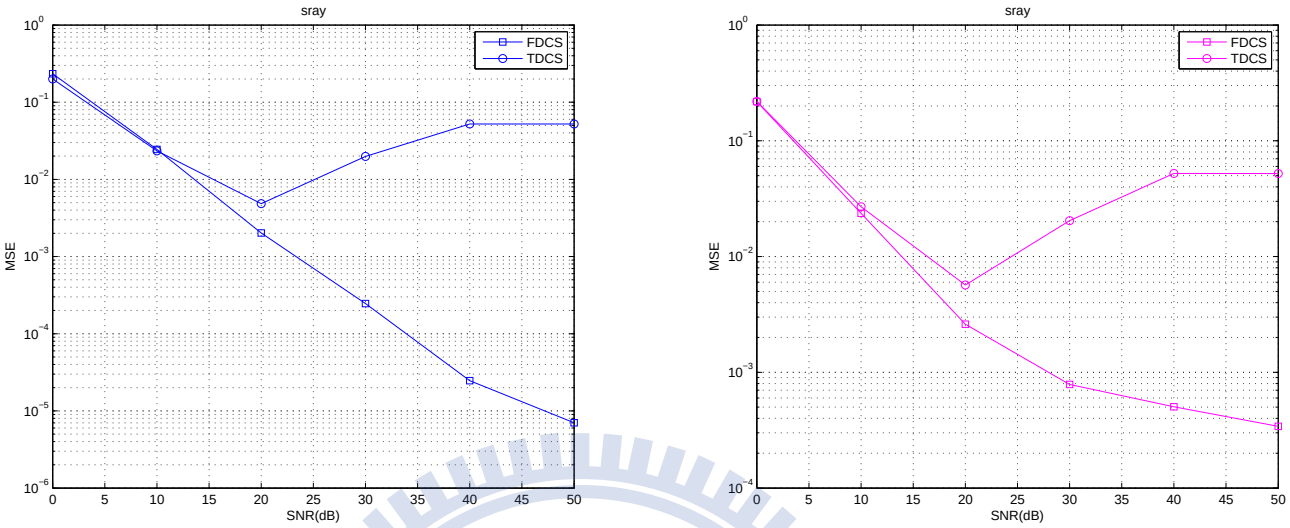

(a)(b)

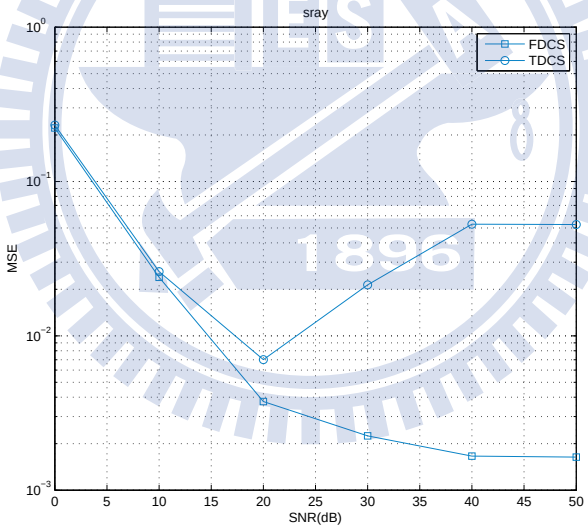

(c)

Figure 4.54: MSE performance of different channel separation methods equipped with FD GWD in 4×4 MIMO over single-path Rayleigh fading channel at speeds (a) 3 km/h, (b) 60 km/h, and (c) 120 km/h.

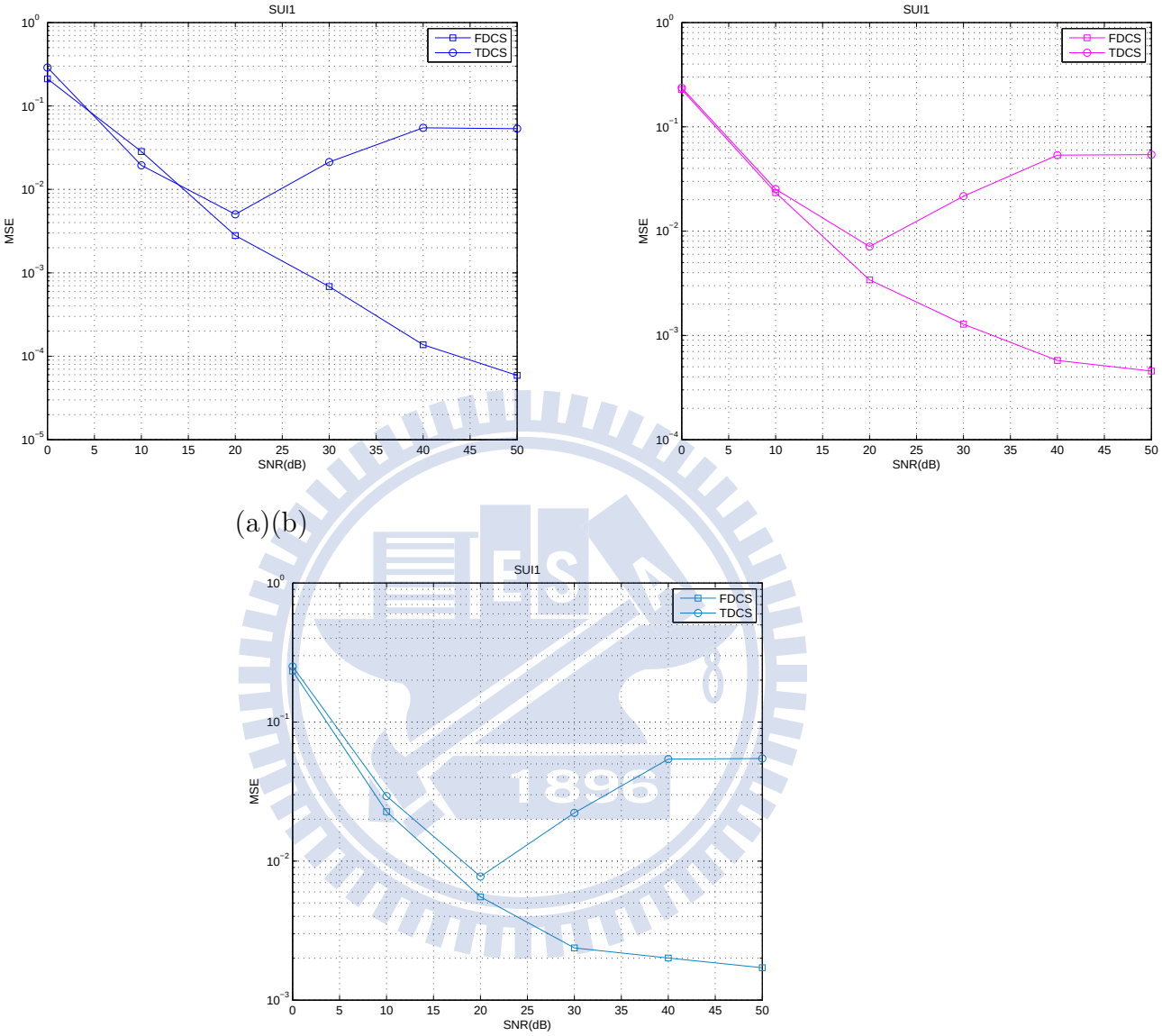

(a)(b)

(c)

Figure 4.55: MSE performance of different channel separation methods equipped with FD GWD in 4×4 MIMO over SUI1 fading channel at speeds (a) 3 km/h, (b) 60 km/h, and (c) 120 km/h.

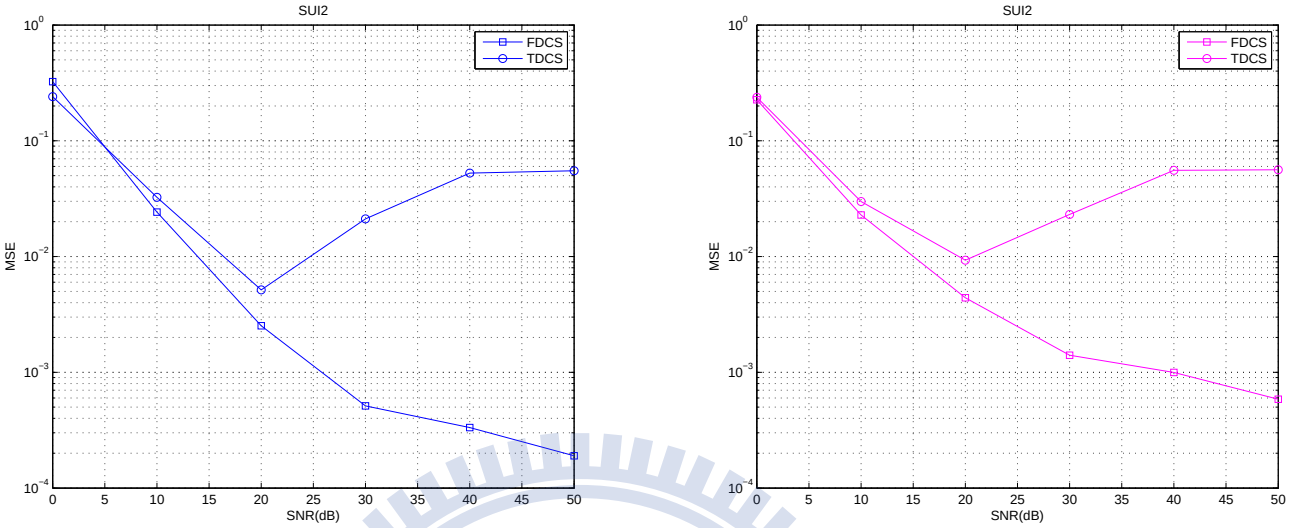

(a)(b)

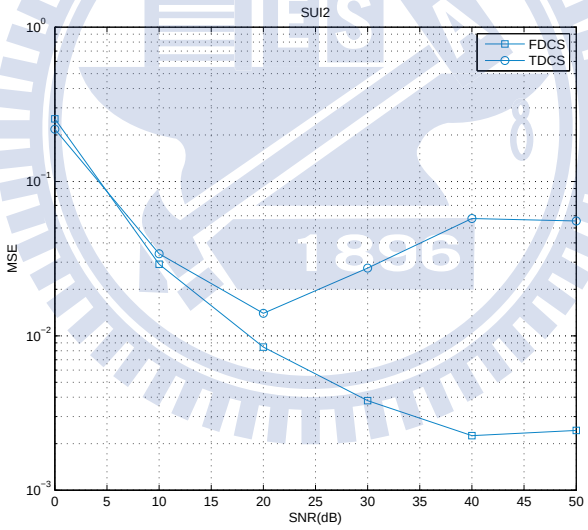

(c)

Figure 4.56: MSE performance of different channel separation methods equipped with FD GWD in 4×4 MIMO over SUI2 fading channel at speeds (a) 3 km/h, (b) 60 km/h, and (c) 120 km/h.

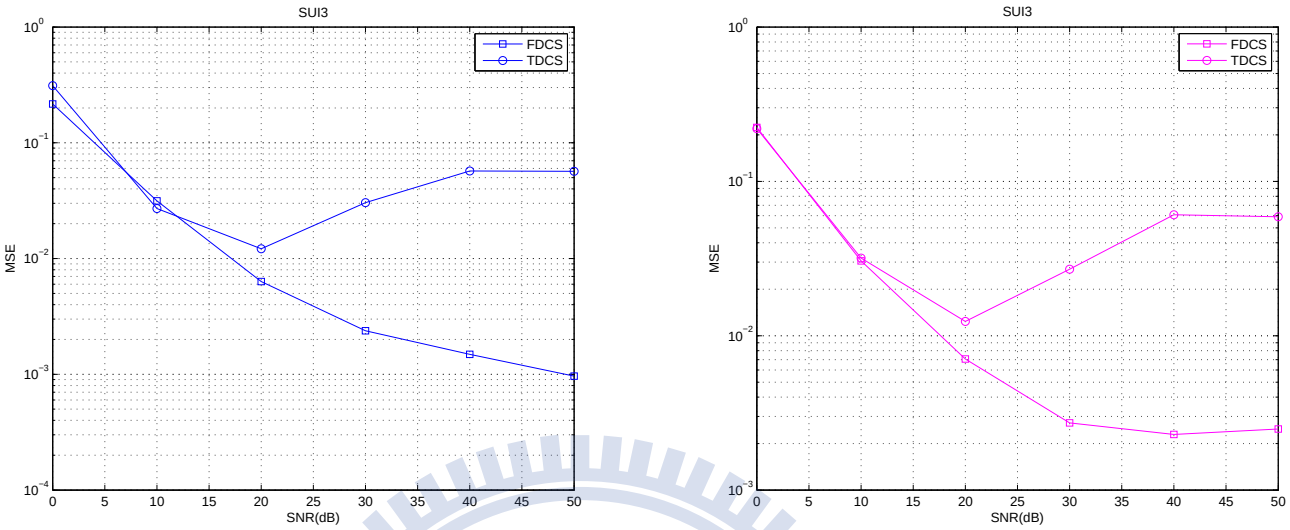

(a)(b)

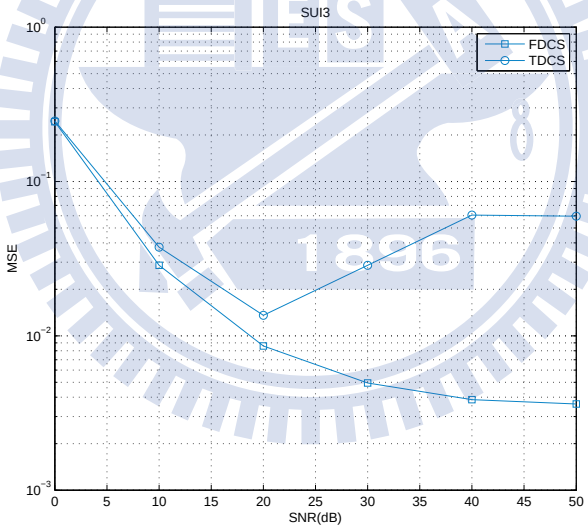

(c)

Figure 4.57: MSE performance of different channel separation methods equipped with FD GWD in 4×4 MIMO over SUI3 fading channel at speeds (a) 3 km/h, (b) 60 km/h, and (c) 120 km/h.

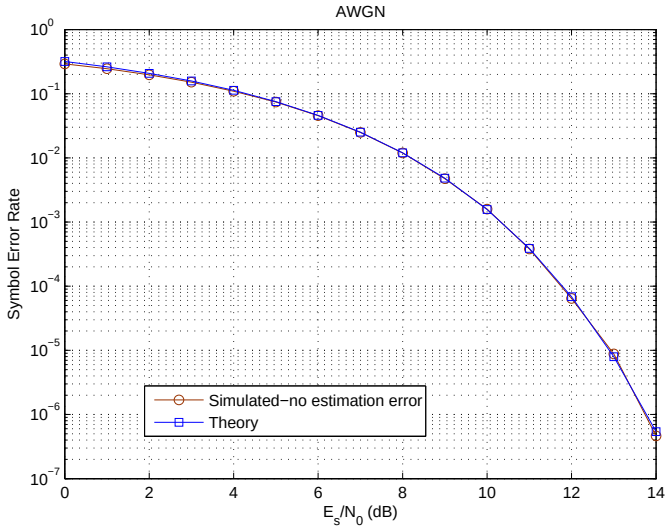

Figure 4.58: SER performance under perfect channel state information (CSI) compared with theory in AWGN for QPSK.

- N_0 = noise power spectral density (W/Hz), and
- $Q(x) = \frac{1}{2\pi}\int_x^\infty e^{-t^2/2}dt$.

Figure 4.58 plot the simulated SER values with uncoded QPSK in AWGN according to the block diagram in Figure 4.1 together with the theoretical values. We see that the simulation result agrees with the theoretical curve.

4.4.1 SISO

Figures 4.59–4.63 show the SER performance of different channel estimation methods in AWGN, single-path Rayleigh, SUI1, SUI2 and SUI3 channels, respectively. We can see that the SER performance of the different methods largely follows a similar ordering as their MSE performance, but the disparity is not as pronounced. Such a phenomenon has been observed in other simulations conducted previously [22]. We suspect that the reason may have to do with insufficient whiteness of the channel estimation error. But this is yet to be investigated.

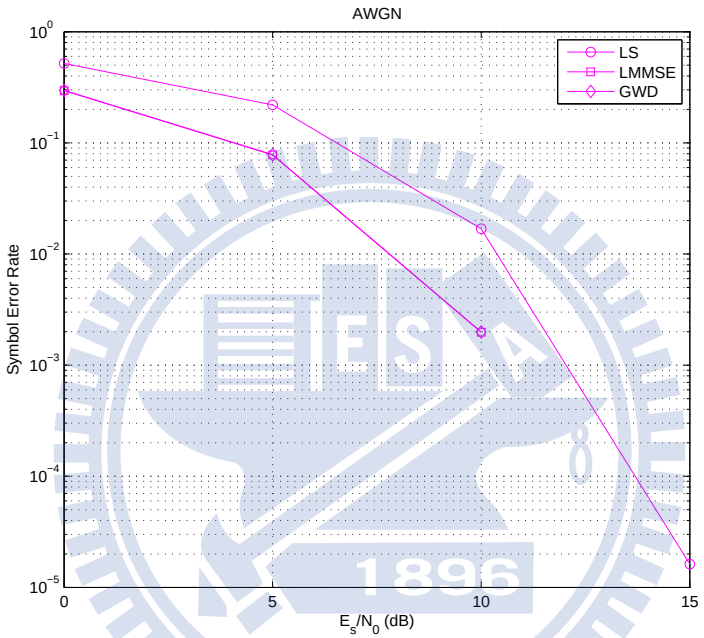

Figure 4.59: SER performance of different channel estimation methods with SL = 12, SG = 12 in AWGN channel.

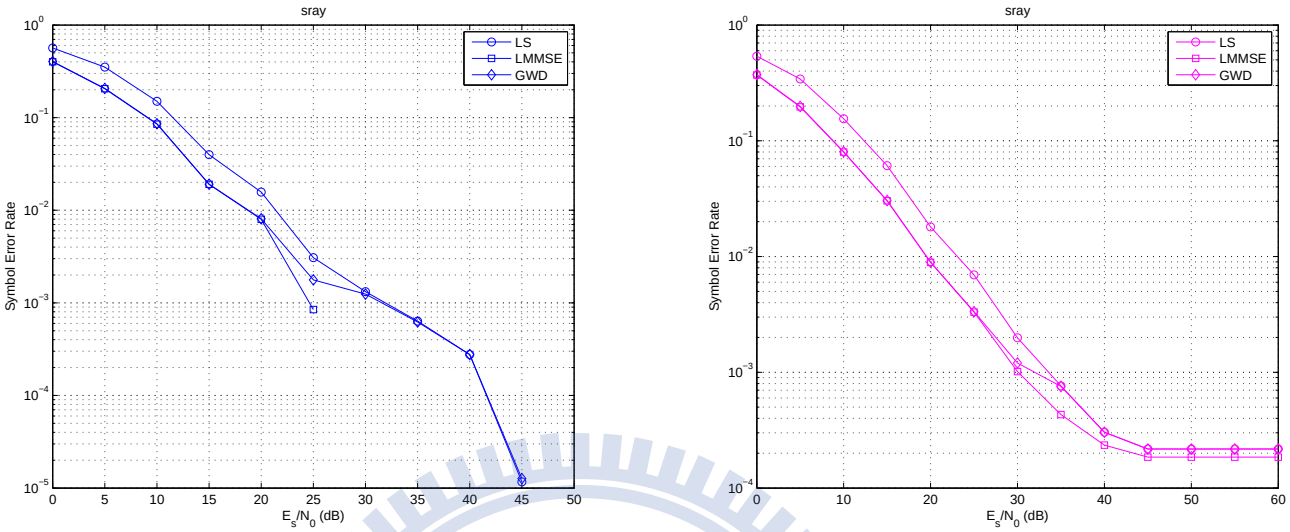

(a)(b)

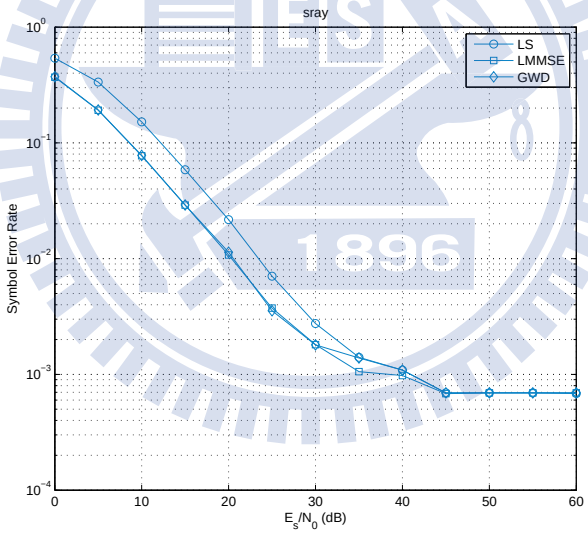

(c)

Figure 4.60: SER performance of different channel estimation methods with SL = 12, SG = 12 in signal path Rayleigh fading channel at speeds (a) 3 km/h, (b) 60 km/h, and (c) 120 km/h.

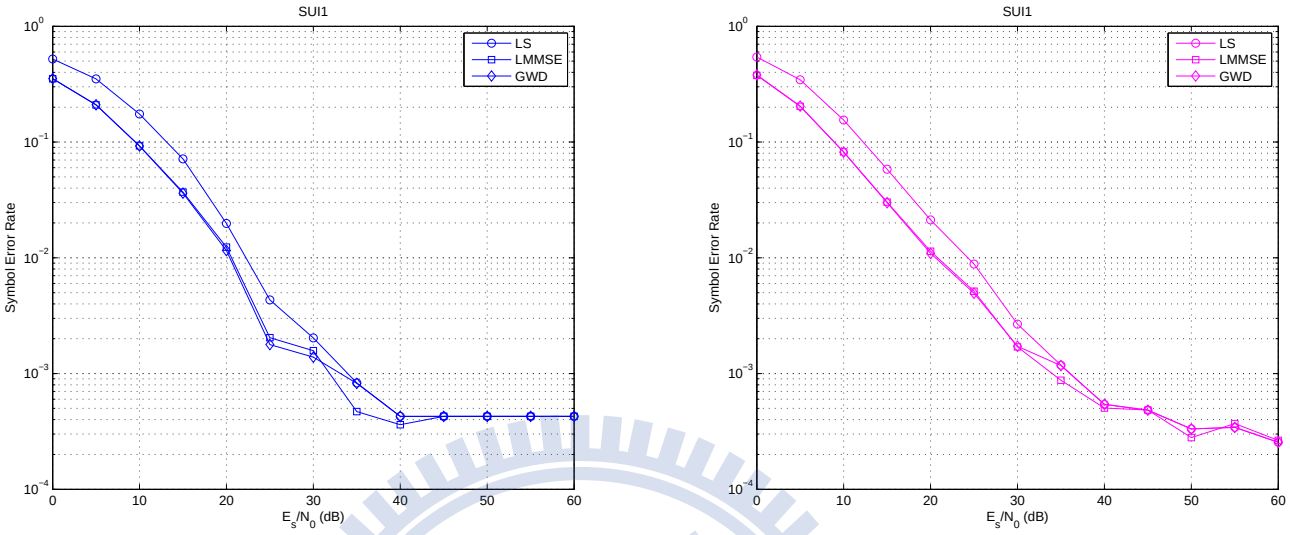

(a)(b)

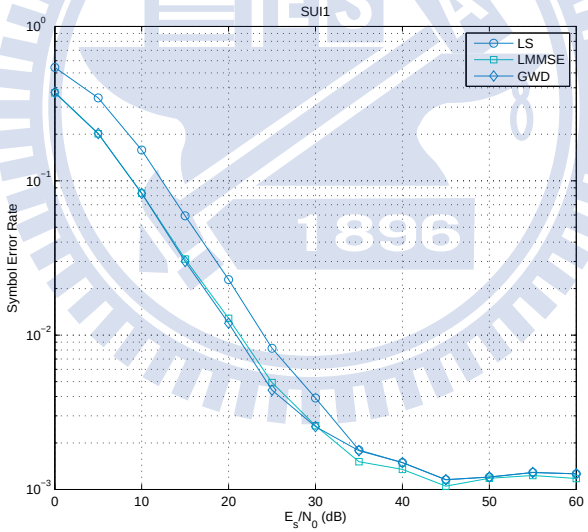

(c)

Figure 4.61: SER performance of different channel estimation methods with SL = 12, SG = 12 in SUI1 fading channel at speeds (a) 3 km/h, (b) 60 km/h, and (c) 120 km/h.

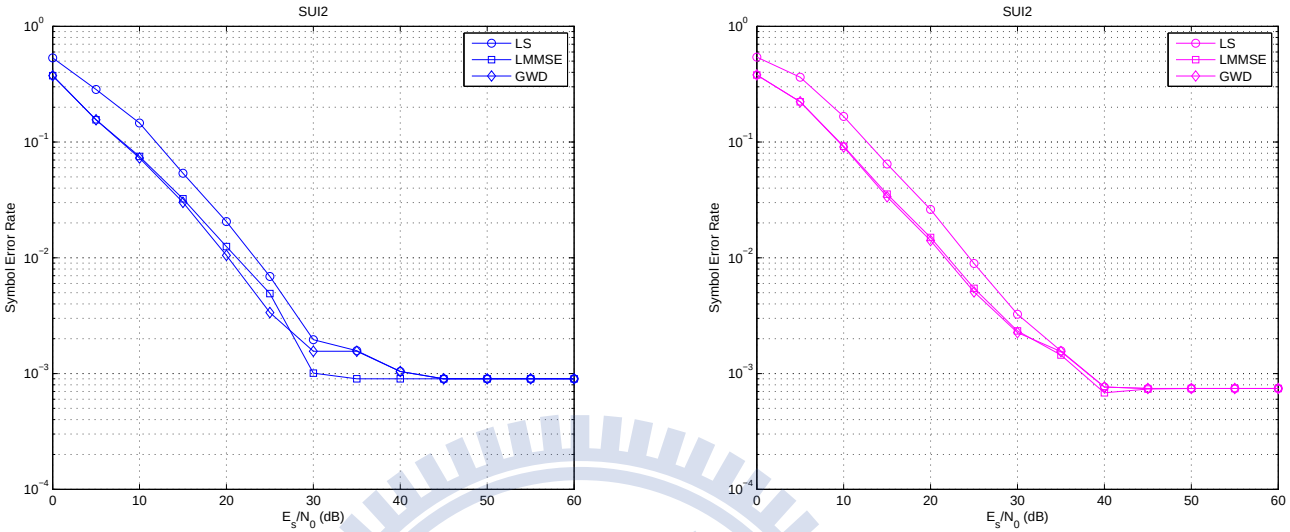

(a)(b)

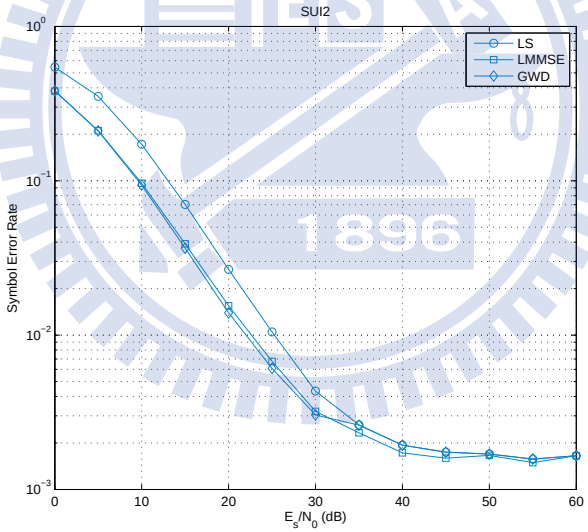

(c)

Figure 4.62: SER performance of different channel estimation methods with SL = 12, SG = 12 in SUI2 fading channel at speeds (a) 3 km/h, (b) 60 km/h, and (c) 120 km/h.

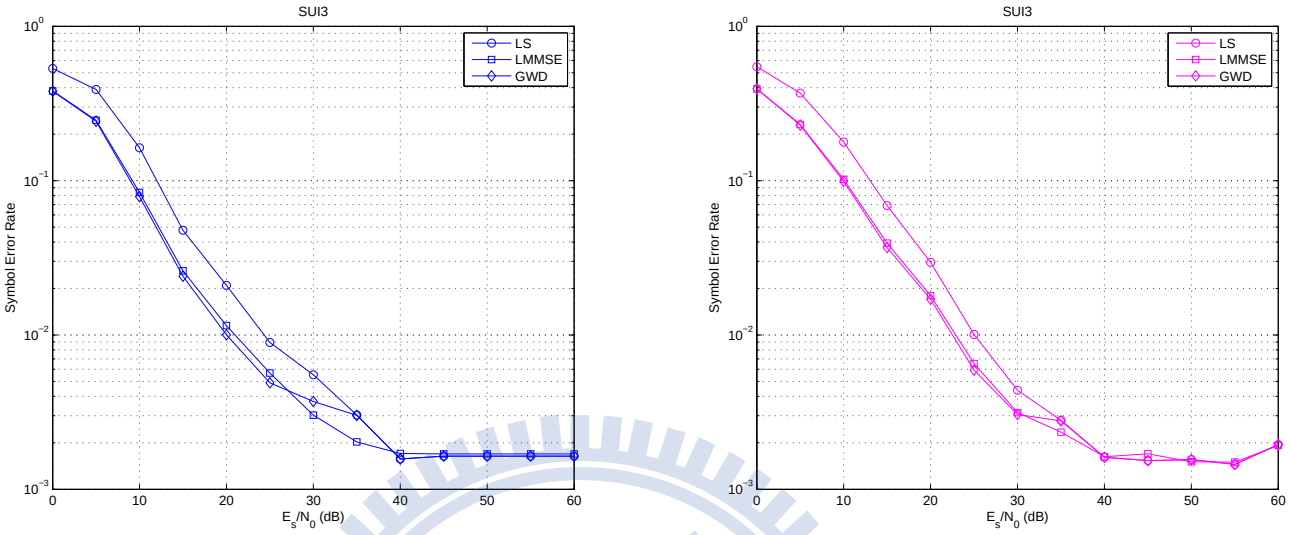

(a)(b)

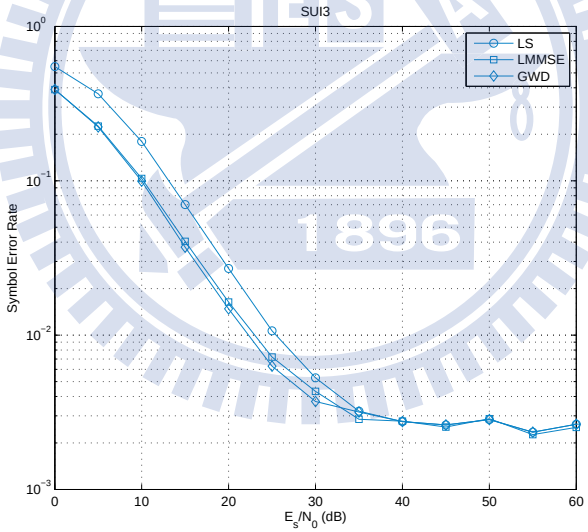

(c)

Figure 4.63: SER performance of different channel estimation methods with SL = 12, SG = 12 in SUI3 fading channel at speeds (a) 3 km/h, (b) 60 km/h, and (c) 120 km/h.

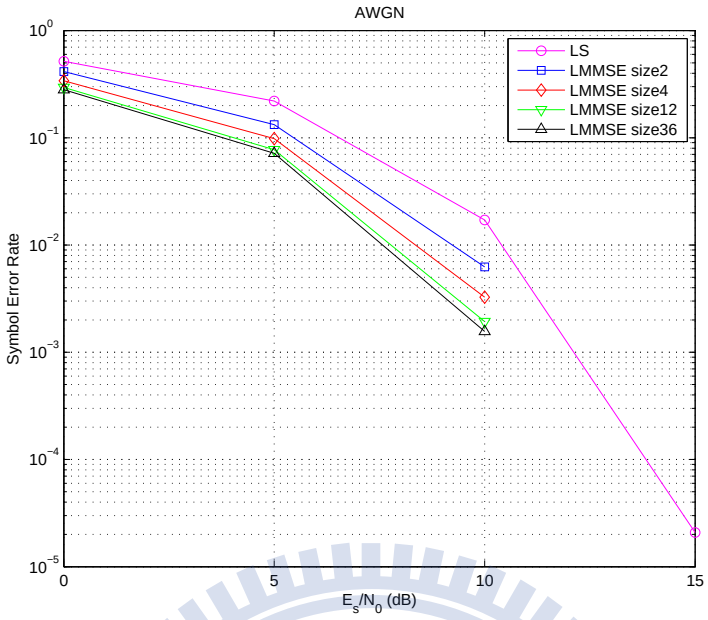

Figure 4.64: SER performance at different FD LMMSE submatrix sizes S_L in AWGN channel.

Since the SER and MSE performance have similar ordering, we now only concentrate on the 60 km/h case. Figures 4.64–4.66 show the SER performance of different FD LMMSE submatrix size S_L in AWGN, single-path Rayleigh, SUI1, SUI2 and SUI3 channels, respectively, for a speed 60 km/h. The ordering of simulated SER performance is similar to the MSE performance as shown in Figures 4.10–4.14. We note that difference in SER performance with different S_L is often quite.

Figure 4.67–4.69 show SER performance of different FD GWD bandwidth S_G in AWGN, single-path Rayleigh, SUI1, SUI2 and SUI3 channels, respectively, for speed 60 km/h. The results in these figures are rather similar to LMMSE qualitatively. The ordering of simulated SER performance is similar to the MSE performance shown in Figures 4.15–4.19. We note again that the difference in SER performance with different S_G is often small.

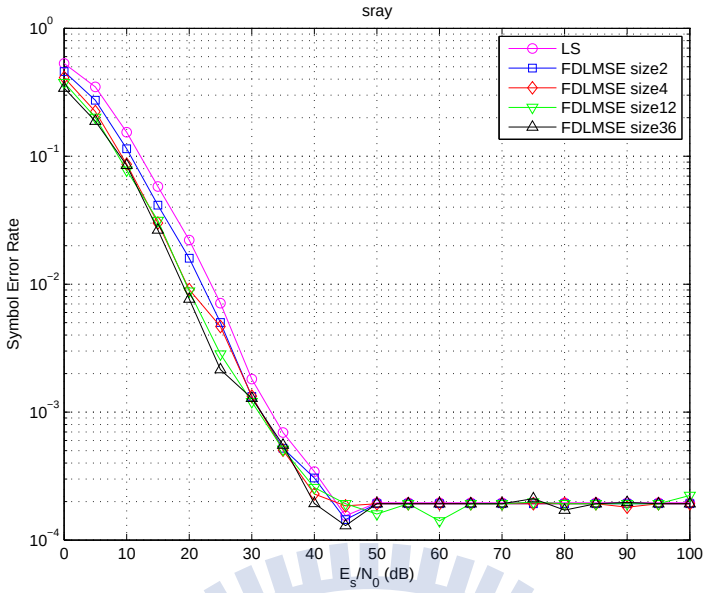

Figure 4.65: SER performance at different FD LMMSE submatrix sizes S_L in single-path Rayleigh channel at speed 60 km/h.

4.4.2 MIMO

In MIMO transmission, the SER performance depends highly on the multi-antenna receiving method, for which many techniques have been proposed by many people. As our interest is mainly in channel estimation and not in signal detection, we relegate the associated study on SER performance to potential future research.

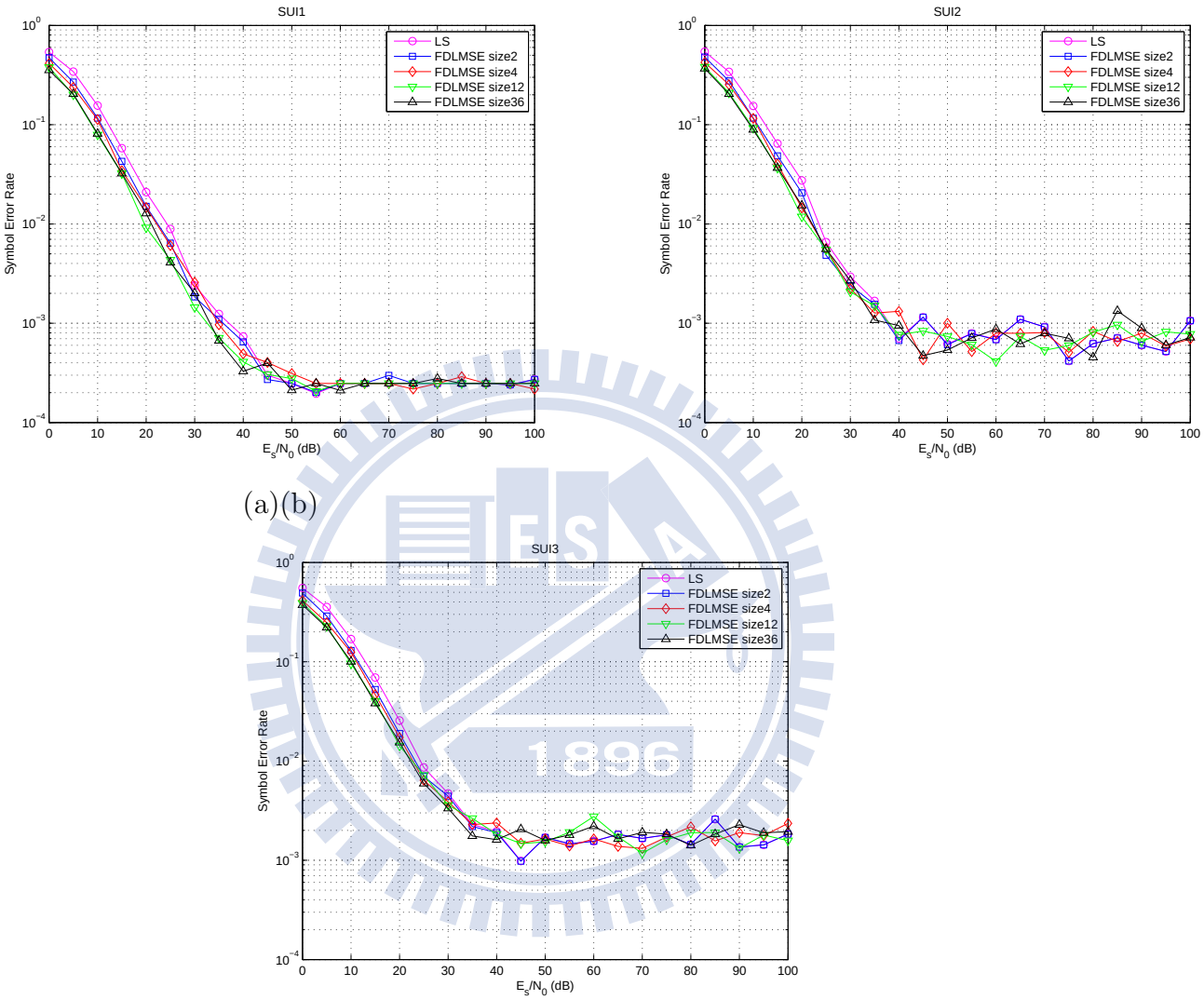

(a)(b)

(c)

Figure 4.66: SER performance at different FD LMMSE submatrix sizes S_L in (a) SUI1, (b) SUI2, and (c) SUI3 fading channels at speed 60 km/h.

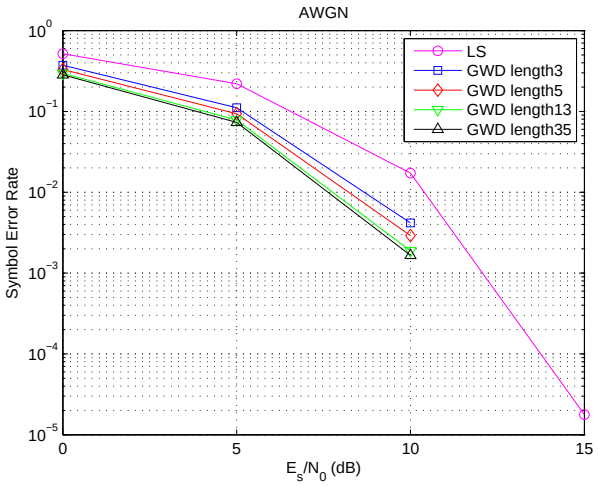

Figure 4.67: SER performance at different FD GWD bandwidth S_G in AWGN channel.

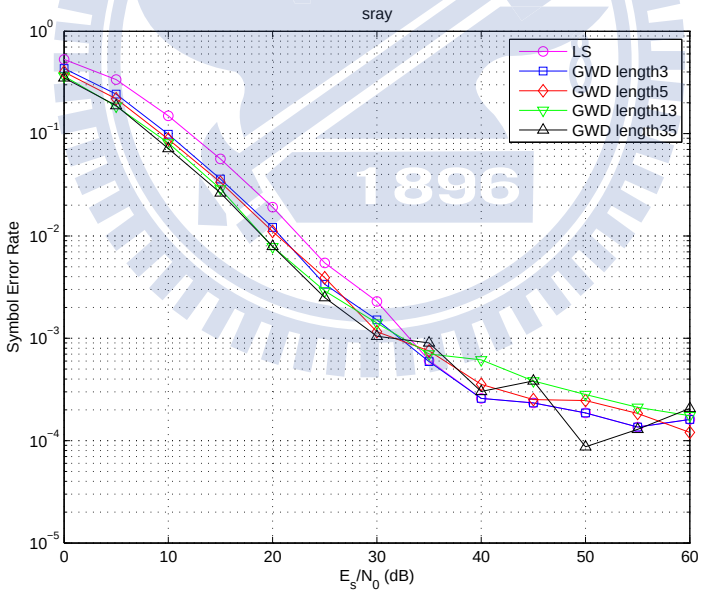

Figure 4.68: SER performance at different FD GWD bandwidth S_G in single-path Rayleigh channel at speed 60 km/h.

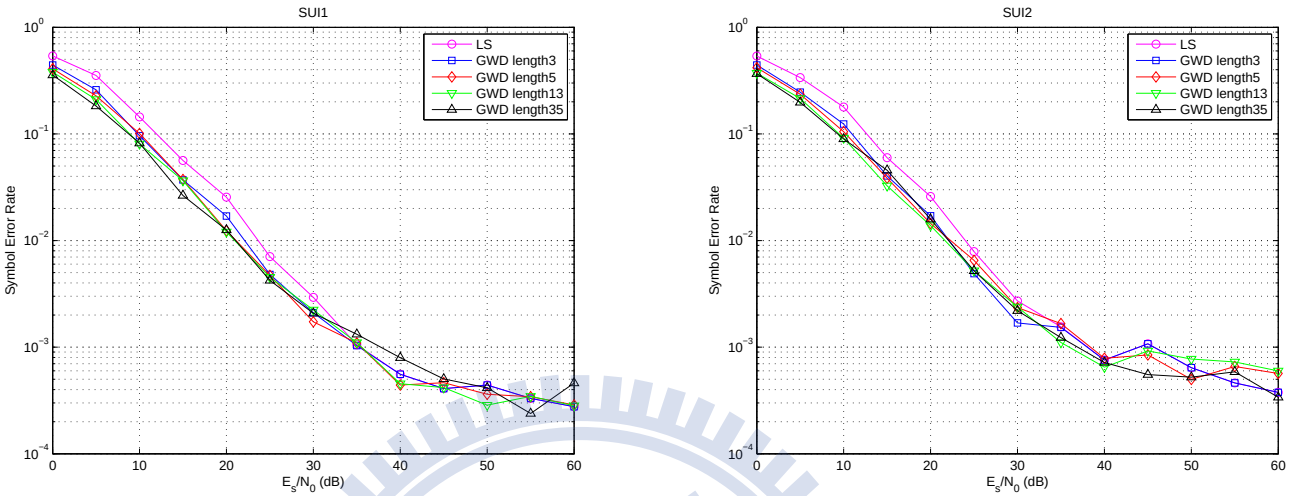

(a)(b)

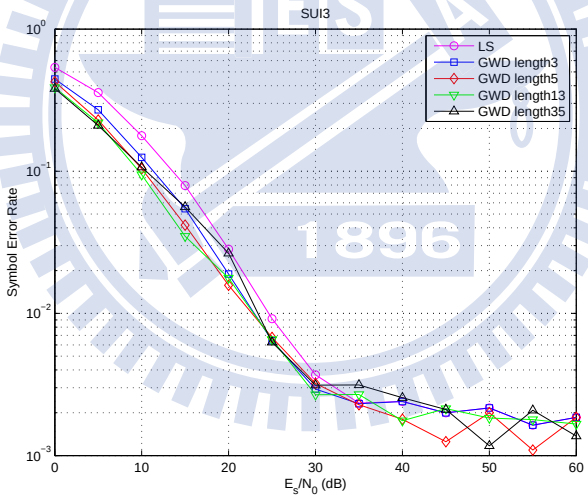

(c)

Figure 4.69: SER performance at different FD GWD bandwidth S_G in (a) SUI1, (b) SUI2, and (c) SUI3 fading channel at speed 60 km/h.

Chapter 5

Conclusion and Potential Future Work

5.1 Conclusion

In our study we analyzed the LTE SISO system and LTE-A MIMO system's channel estimate. In the SISO system we studied the estimator in the frequency domain, FD LMMSE and FD GWD respectively. Although FD LMMSE estimation is more accurate, there is the higher complexity and matrix irreversibility problem. In order to solve these problems, we used SVD decomposition and reduced rank to reduce the amount of computation. We also developed the FD GWD method using a similar constant matrix as the frequency domain estimator. This constant will change in size according to the SNR. Because the matrix is a constant matrix with a given amount, the amount of computation will drop a lot, and the performance will not differ too much. In the MIMO system, we examined how to separate the information on the receiving end of all the information transmitted by the transmission antenna. There are two methods. The first is according to [13]'s time-domain antenna separation (TDAS) and the second is our own developed frequency-domain antenna separation (FDAS). Based on the above analysis, it is evident frequency domain antenna separation has a better performance because it will not be affected leakage power. However, the frequency-domain's antenna

separator accuracy is based on size of the coherent bandwidth. That is, the channel delay cannot be too large, or it will still produce serious errors. In all our simulated channels there was no such problem. Next, we considered placing SISO system's frequency domain estimator into the MIMO system that has been through antenna separation. FD GWD accompanied with TDAS will have significant estimation error in high SNR. In this thesis paper the best match is using FDAS matched with FD GWD's frequency domain estimates.

5.2 Potential Future Work

There are several possible extension for our research:

- Try to do channel estimation in MIMO PUCCH.
- Try to do channel estimation in MU MIMO.
- Try to discuss the MSE of overlap is not better.
- Try to discuss why dose MSE not proportional to SER.
- Find suitable methods of signal detection and use these methods to solve SER problems in MIMO
- Try other kinds of techniques to estimate channel response that more suitable for SC-FDMA.
- In this thesis, we do not consider the influence of intercarrier interference (ICI). The ICI simulation can be involved in the future.
- Change matlab code to C code and try to implement on DSP.

Bibliography

[1] 3GPP TS 36.211, *Physical Channels and Modulation*. V8.9.0, Dec. 2009.

[2] 3GPP TS 36.211, *Physical Channels and Modulation*. V10.4.0, Jan. 2012.

[3] Farooq Khan, *LTE for 4G Mobile Broadband: Air Interface Technologies and Performance*. Cambridge University Press, 2009.

[4] 3GPP TS 36.212, *Multiplexing and Channel Coding*. V8.8.0, Dec. 2009.

[5] 3GPP TS 36.213, *Physical Layer Procedures*. V8.8.0, Sep. 2009.

[6] A. F. Molisch, *Wireless Communications*. Wiley, 2005.

[7] J. G. Proakis and M. Salehi, *Digital Communications, 5th ed.* McGraw-Hill, 2008.

[8] Steven M. Kay, *Fundamentals of Statistical Signal Processing, Volume I: Estimation Theory*. Prentice Hall, 1993.

[9] Steven M. Kay, *Fundamentals of Statistical Signal Processing, Volume II: Detection Theory*. Prentice Hall, 1993.

[10] Jia-Chin Lin, Kao-Peng Chou, and Shih-Chan Huang, "Novel channel estimation techniques on SC-FDMA uplink transmission," in *IEEE Veh. Technol. Conf*, May 2010, pp. 1–5.

[11] M.-H. Hsieh, "Synchronization and channel estimation techniques for OFDM systems," Ph.D. dissertation, Department of Electronics Engineering and Institute of Electronics, National Chiao Tung Uni-versity, Hsinchu, Taiwan, R.O.C., May 1998.

[12] B. Karakaya, H. Arslan, and H. A. Curpan, "Channel estimation for LTE uplink in high Doppler spread," in *Proc. IEEE Wirel. Commum. Network. Conf*, Apr. 2008, pp. 1126–1130.

[13] Xiaolin Hou, Zhan Zhang, and Hidetoshi Kayama, "DMRS design and channel estimation for LTE-Advanced MIMO uplink," in IEEE *Vehicular Technology Conference Fall*, Sep. 2009, pp.1–5.

[14] A. Nix, G. Huang, and S. Armour, "DFT-based channel estimation and noise variance estimation techniques for single-carrier FDMA," in *IEEE Veh. Technol. Conf*, Oct. 2010, pp. 1–5.

[15] C. Mehlfuhrer, M. Rupp, M. Simko, and M. Wrulich, "Doubly dispersive channel estimation with scalable complexity," in *IEEE International ITG Workshop on Smart Antennas*, Feb. 2010, pp. 251–256.

[16] K. Higuchi, M. Sawahashi, T. Kawamura, and T. Sakurai, "Effect of noise suppression in channel estimation for single carrier FDMA radio access with variable transmission bandwidth," in *IEEE Int. Sym. Wireless Commun. Systems*, Oct. 2008, pp. 204–208.

[17] M. K. Mehmet and H. Arslan, "Channel estimation for wireless OFDM systems," *Commun. Surveys Tuts.*, vol. 9, no. 2, pp. 18–48, 2nd quarter 2007.

[18] Amir D. Dabbagh, Amitava Ghosh, and Rapeepat Ratasuk, "On UMTS-LTE physical uplink shared and control channels," in *IEEE Veh. Technol. Conf*, Sep. 2008, pp. 1–5.

[19] C.S. Park, Y.-P.E. Wang, G. Jöngren, and D. Hammarwall, "Evolution of uplink MIMO for LTE-advanced," *IEEE Communications Magazine*, vol. 49, no. 2, pp. 112–121, Feb. 2011

[20] V. Erceg *et al.*, "Channel models for fixed wireless applications," IEEE 802.16.3c-01/29r4, July 2001.

[21] K.-C. Yu, "Study in IEEE 802.16e OFDMA MIMO channel estimation techniques and associated digital signal processor implementation," M.S. thesis, Department of Electronics Engineering and Institute of Electronics, National Chiao Tung University, Hsinchu, Taiwan, R.O.C., Dec. 2008.

[22] Juo-Han Yu, "Research in LTE Uplink channel estimation techniques," M.S. thesis, Department of Electronics Engineering and Institute of Electronics, National Chiao Tung University, Hsinchu, Taiwan, R.O.C., Oct. 2011.

[23] http://en.wikipedia.org/wiki/3GPP_Long_Term_Evolution

作者簡介

作者畢業於淡江大學電機工程學系，研究所就讀國立交通大學電子研究所，指導教授為林大衛老師。主要研究為無線通訊系統，修過的課程有數位通訊、通道編碼、行動通訊。而論文主要研究LTE無線通訊系統中的通道估計。而IC課程上也修過如：數位積體電路、計算機結構，同時也在碩一暑假時期前往國家晶片系統設計中心進修Verilog相關課程，因此對於IC設計上也有一些基本的了解。

李政憲